

Atomic and Electronic Structure of  
Quantum Dots Measured with Scanning  
Probe Techniques

Cover: A cartoon about Double-Barrier Tunneling Junction

Ph.D. Thesis Utrecht University, January 2012  
ISBN: 978-90-393-5684-5

# Atomic and Electronic Structure of Quantum Dots Measured with Scanning Probe Techniques

---

De atomaire en elektronische structuur van quantum  
kristallen bestudeerd met raster microscopie en  
spectroscopie

(met een samenvatting in het Nederlands)

Proefschrift

ter verkrijging van de graad van doctor aan de Universiteit Utrecht op gezag van de rector  
magnificus, prof. dr. G.J. van der Zwaan, ingevolge het besluit van het college voor  
promoties in het openbaar te verdedigen op maandag 9 januari 2012 des middages te 4.15  
uur

door

Zhixiang Sun

geboren op 20 februari 1980, te Hebei, China

Promotoren: Prof. dr. D. A. M. Vanmaekelbergh  
Prof. dr. P. Liljeroth

... to my parents

---

---

# Contents

<b>1</b>	<b>Introduction</b>	<b>3</b>
1.1	Chapter outline . . . . .	3
1.2	Basic principles of STM . . . . .	4
1.2.1	History of STM and theory of quantum tunneling . . . . .	4
1.2.2	Scanning tunneling spectroscopy . . . . .	9
1.2.3	Double-barrier tunneling junction . . . . .	10
1.2.4	Calculation of electron-phonon coupling strength in QDs . . . . .	13
1.3	Introduction to AFM . . . . .	15
1.3.1	Development of AFM . . . . .	15
1.3.2	Theory of nc-AFM . . . . .	16
1.3.3	Force spectroscopy with FM-AFM . . . . .	20
1.3.4	Oscillation amplitude effects . . . . .	21
1.4	Scope and outline of this thesis . . . . .	23
<b>2</b>	<b>Electron-phonon coupling in CdSe nanorods</b>	<b>27</b>
2.1	Introduction . . . . .	27
2.2	Experimental . . . . .	30
2.3	Results and discussion . . . . .	30
2.4	Summary and outlook . . . . .	38
2.5	Acknowledgement . . . . .	38
<b>3</b>	<b>Hole-Induced Electron Transport through PbSe/CdSe Core-Shell QDs</b>	<b>39</b>
3.1	Introduction . . . . .	39
3.2	Experimental . . . . .	41
3.3	Results and discussions . . . . .	42
3.4	Summary . . . . .	47
3.5	Acknowledgement . . . . .	47
<b>4</b>	<b>Epitaxial graphene moiré pattern on Ir(111) measured by nc-AFM</b>	<b>49</b>
4.1	Introduction . . . . .	49
4.2	Experimental . . . . .	51

4.3	Results and discussion . . . . .	52
4.4	Conclusions . . . . .	58
4.5	Acknowledgement . . . . .	58
<b>5</b>	<b>Confined electronic states in graphene nanoflakes on Ir(111) probed with nc-AFM</b>	<b>61</b>
5.1	Electronic structure of graphene . . . . .	61
5.2	Experimental . . . . .	66
5.3	Results and discussions . . . . .	67
5.4	Summary . . . . .	71
<b>6</b>	<b>CO-CO intermolecular interaction probed with nc-AFM</b>	<b>73</b>
6.1	Introduction to the problem . . . . .	73
6.2	Experimental . . . . .	75
6.3	Results and discussion . . . . .	75
6.4	Summary and outlook . . . . .	81
6.5	Acknowledgement . . . . .	81
	<b>References</b>	<b>82</b>
	<b>Appendix</b>	<b>95</b>
	<b>Summary</b>	<b>97</b>
	<b>Samenvatting</b>	<b>99</b>

---

# Acronyms

<i>AFM</i>	atomic force microscopy
<i>CVD</i>	chemical vapor deposition
<i>DBTJ</i>	double-barrier tunneling junction
<i>DOS</i>	density of states
<i>FCC</i>	face-centered cubic
<i>FM – AFM</i>	frequency modulation AFM
<i>HCP</i>	hexagonal close-packed
<i>HOMO</i>	highest occupied molecular orbital
<i>HOPG</i>	highly oriented pyrolytic graphite
<i>IETS</i>	inelastic electron tunneling spectroscopy
<i>LDOS</i>	local density of states
<i>LT – STM</i>	low temperature STM
<i>LUMO</i>	lowest unoccupied molecular orbital
<i>nc – AFM</i>	non-contact AFM
<i>QD</i>	quantum dot
<i>SPM</i>	scanning probe microscopy
<i>STM</i>	scanning tunneling microscopy
<i>STS</i>	scanning tunneling spectroscopy
<i>TEM</i>	transmission electron microscopy
<i>vdW</i>	van der Waals



---

# Chapter 1

## Introduction

### 1.1 Chapter outline

Scanning tunneling microscopy (STM) was developed by Gerd Binnig, Christoph Gerber and Heinrich Rohrer at IBM in the early 1980s (Binnig and Rohrer, 1982). Several years later, they and Calvin Quate invented the atomic force microscope (AFM) (Binnig *et al.*, 1986). In the following years, many other techniques derived from STM and AFM, such as scanning magnetic force microscopy (Rugar *et al.*, 1990; Hartman, 1999; Schwarz and Wiesendanger, 2008) and near-field scanning optical microscopy (Betzig *et al.*, 1986; Dunn, 1999), were developed. In general, the family is called scanning probe microscopy (SPM) (Wiesendanger, 1998). SPM can achieve atomic imaging resolution and can be used under different conditions: liquid, ambient and ultrahigh vacuum. SPM has been applied to many fields in science such as surface science, condensed matter physics, chemistry, biophysics etc. New SPM techniques are still under development today; for example, recent experiments by Loth *et al.* (2010) show that by using an electrical pump-probe technique, low-temperature (LT) STM can be used to probe electronic processes at the time scale of a few tens of nanoseconds.

In this chapter, I will give a general introduction to STM, AFM and related concepts necessary for the understanding of the experiments presented in this thesis. In section 1.2 I will introduce the working principles of scanning tunneling microscopy and spectroscopy (STS). After that, electron-phonon coupling in polar semiconductor materials will be discussed. Section 1.3 will focus on the principles of AFM. In that section, we will briefly introduce different operating modes. Also the principle of force spectroscopy using frequency modulation (FM) AFM will be discussed.

## 1.2 Basic principles of STM

### 1.2.1 History of STM and theory of quantum tunneling

The Nobel lecture of Binnig and Rohrer (1987) recounts the story of how STM was invented. The main goal at that time was to develop a tool for local conductance spectroscopy on a small sample area of less than  $10 \text{ nm}^2$ .

Jaklevic and Lambe (1966) measured the molecular vibration spectra of propionic acid and acetic acid with Al-Al oxide-Pb junctions, as illustrated in Fig. 1.1. The technique was developed into a power method named as inelastic electron tunneling spectroscopy (IETS) (see ex. Klein *et al.* (1973); Hansma (1977)). IETS and single-electron tunneling devices (Gorter, 1951) were developed before the invention of STM. IETS is measuring the tunneling current through a biased metal-thin insulator-metal junction. The insulator layer should be sufficiently thin such that electron tunneling proceeds at an appreciable rate. The thin layer is probed through inelastic tunneling processes inside the material. If molecules are present inside the thin film, inelastic tunneling processes will influence the tunneling current. By variation of the bias, one can perform spectroscopic measurements of those inelastic tunneling processes and obtain electronic information on the impurities.

The new idea led to the invention of STM was to apply vacuum tunneling between sample and a sharp tip, in order to localize the tunneling current during  $I$  vs.  $V_b$  spectroscopy. Only later Binnig and Rohrer realized that this can also be used for topography imaging (Binnig and Rohrer, 1987). A piezoelectric tube can be used for controllable motion of the tip in the vertical and lateral directions (Binnig and Smith, 1986). A sketch of the STM instrument is shown in Fig. 1.2 and the tunneling junction is formed between the tip apex and sample surface.

For topography imaging of the sample surface, two scanning modes can be used as shown in Fig. 1.3. One is scanning under a constant tunneling current  $I_t$ , where a feedback adjusts the tip-sample distance. Since the tunneling current depends on local electronic structure, the topography is not equal to the “geometric” topography<sup>1</sup> of the sample surface. Typically, the difference is small, and this mode can be used to get information about the surface structure. The other operating mode is scanning at constant height. In this case, the tip-sample distance feedback is turned off and  $I_t$  as a function of the tip position is measured. In order to avoid contact between the tip and sample and get large enough current signal, this mode is only applied to samples with atomic scale corrugations.

The working mechanism behind STM is quantum tunneling between two electrodes separated by a vacuum barrier due to the wavelike behavior of electrons. The transmission coefficient  $T$ , which is the ratio between the transmitted wave amplitude and the incident wave amplitude, is commonly used to describe the tunneling process. The exact solution for the transmission coefficient for a time-independent potential can be calculated with the time-independent Schrödinger equation.

---

<sup>1</sup>Here the “geometric” topography means the topography which is equivalent to the atomic skeleton of the material.

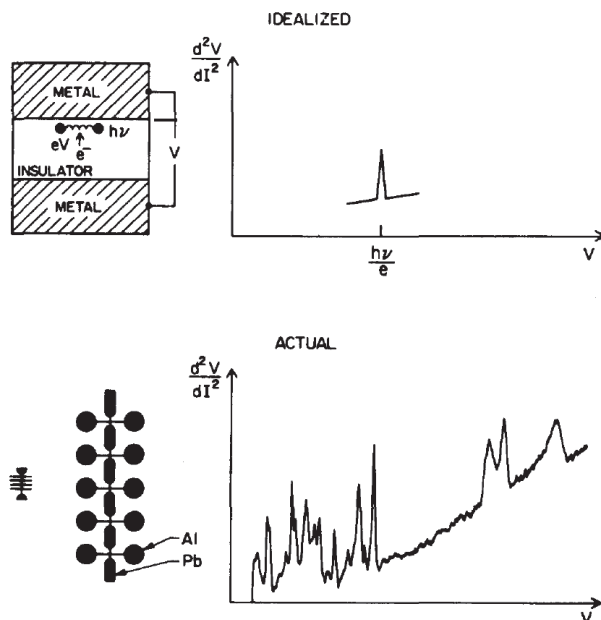


Figure 1.1: Sample and spectra of inelastic electron tunneling, where  $V$  is the voltage bias and  $I$  is the tunneling current. Top is the idealized view of IETS, where  $h\nu$  is the energy of a vibrational mode of the organic molecule. Bottom left is the actual sample which was made on glass slide by first depositing the aluminum electrode. Then the electrode was oxidized in air or in a glow discharge to form the insulating layer. Then the sample is doped with organic molecules. Finally the top electrode Pb is evaporated. A actual spectrum is shown in the right where the peaks represents the many vibrational mode of an organic molecule. The mechanism behind this is that when  $eV \geq h\nu$ , there is an inelastic tunneling path open beside of elastic tunneling from exciting a vibrational mode of a molecule. (Copied with permission from Hansma (1977))

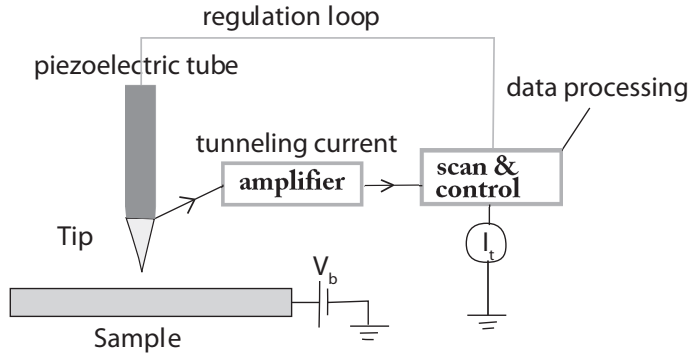


Figure 1.2: A sketch of STM instrument. Here the bias is applied to the sample and tunneling current is measured through the tip.

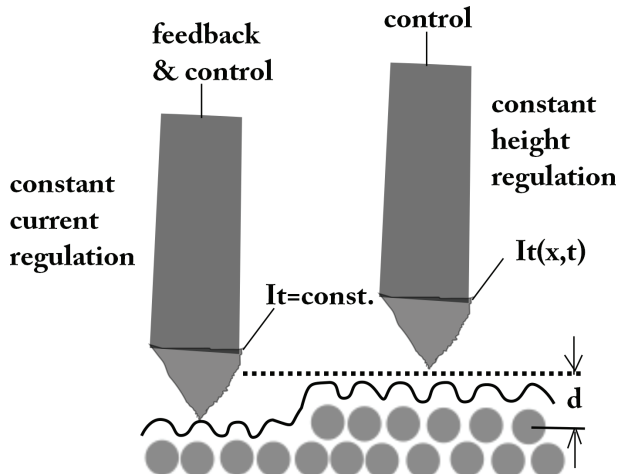


Figure 1.3: Illustration of the two regulation modes of STM topography scanning. Left: Scanning under constant current mode  $I_t = \text{const.}$ . Right: Scanning under constant height mode  $d = \text{const.}$ .

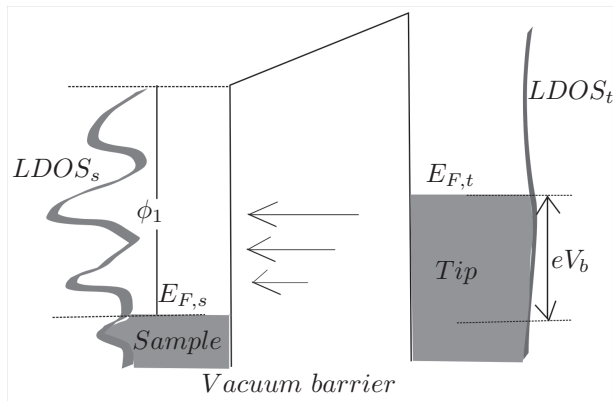


Figure 1.4: (Color online) Energy diagram of STM tunneling junction with a bias  $V_b$  on the sample.  $\phi_1$  is the work function of the sample surface.  $E_{F,s}$  and  $E_{F,t}$  are the Fermi levels of the sample and the tip. The gray regions show the filled energy levels of the tip and the sample.

In simple tunneling, called elastic tunneling, electrons have same energy before and after the tunneling events. If the energy of the electron is changed after the tunneling process due to electron-phonon coupling etc, we deal with inelastic tunneling. Both mechanisms have been observed in STM measurements.

For an electron elastically tunneling from one state  $\psi_\mu$  to another state  $\psi_\nu$ , the transmission coefficient is given by Fermi's golden rule (Fermi, 1949)

$$T = \frac{2\pi}{\hbar} |M_{\mu,\nu}|^2 \delta(E_\mu - E_\nu), \quad (1.1)$$

where  $M_{\mu,\nu}$  is the tunneling matrix element and  $E_\mu$  and  $E_\nu$  are the energy of state  $\psi_\mu$  and state  $\psi_\nu$ ,  $\delta(x)$  is the Dirac delta function.  $M_{\mu,\nu}$  is determined by the overlap of the two wavefunctions  $\psi_\mu, \psi_\nu$ .

$$M_{\mu,\nu} = \frac{\hbar^2}{2m} \int_V (\psi_\mu^* \nabla \psi_\nu - \psi_\nu^* \nabla \psi_\mu) dv, \quad (1.2)$$

where the integration is over the whole space.

We consider tunneling between a metallic tip and a metallic substrate; the bias  $eV_b$  is given by  $E_{F,t} - E_{F,s}$  (Fig. 1.4). To first order, the tunneling current is given by

$$I_t = \frac{2\pi e}{\hbar} \sum_{\mu,\nu} f(E_\mu) [1 - f(E_\nu + eV_b)] |M_{\mu,\nu}|^2 \delta(E_\mu - E_\nu), \quad (1.3)$$

where  $M_{\mu,\nu}$  is the tunneling matrix elements of tip state  $\psi_\mu$  and sample state  $\psi_\nu$ ,  $E_\mu$  is the energy of state  $\psi_\mu$ .  $f(E)$  is the Fermi-Dirac distribution function which is given by  $f(E) = 1/(\exp((E - \mu)/kT) + 1)$ , and  $\mu$  is the chemical potential.

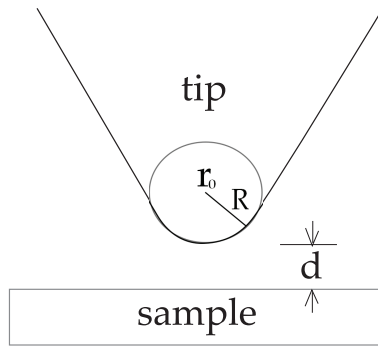


Figure 1.5: The parameters of the STM tip in the Tersoff-Hamann approximation, adapted from Tersoff and Hamann (1985).

In order to estimate the tunneling current, we need a practical way of calculating the matrix element  $M_{\mu,\nu}$ . Bardeen (1961) approached this problem with time-dependent perturbation theory. For a large enough tip-sample distance, he proved that matrix element  $M_{\mu,\nu}$  can be calculated as

$$M_{\mu,\nu} = \frac{\hbar^2}{2m} \int_S (\psi_\mu^* \nabla \psi_\nu - \psi_\nu^* \nabla \psi_\mu) ds, \quad (1.4)$$

where  $S$  can be any surface between the tip and the sample.

We need to know the wavefunctions of both of the tip and the sample surface to calculate the matrix element. In the work of Tersoff and Hamann (1985), they introduced an approximation for the tip atom wavefunction named s-wave approximation. It is widely used for interpreting STM results. It is assumed that the tip has a symmetric structure at the apex with curvature  $R$  with the center located at  $r_0$  (Fig.1.5). The wavefunction of the tip is assumed to be  $s$  wavefunction and the vacuum barrier is  $\phi$ . At the small bias voltage limit, they showed that tunneling current can be written as

$$I_t \propto V_b \frac{R^2}{\kappa^4} e^{2\kappa R} \rho_t(E_F) \rho_s(E_F, r_0) \quad (1.5)$$

where  $\kappa$  is the minimum inverse decay length and it equals to  $\sqrt{2m\phi}/\hbar$ ;  $E_F$  is the Fermi energy of the sample. As we can see from Eq. (1.5), the decay behavior of tunneling current depending on the tip-sample distance  $d$  is

$$I_t \propto e^{-2\kappa d}. \quad (1.6)$$

In view of the Tersoff-Hamann approach, “constant current” topography should be interpreted as an image of the LDOS at the Fermi energy of the tip. Though this

is a very successful theory, it fails in some cases as discussed by Chen (1990, 1992) due to the restriction of  $s$  wavelike tip orbitals. In order to correctly interpret the STM topography images, the electron orbital symmetry and size of the tip apex have to be considered. Recent experiment by Gross *et al.* (2011) shows that  $p$ -wave STM tip can be used to improve the imaging of the molecular orbitals.

### 1.2.2 Scanning tunneling spectroscopy

In addition to the measurements of the sample topography, STM set-up can also be used to probe the LDOS through spectroscopy under varying tip-sample bias. The method in general is called scanning tunneling spectroscopy (STS). There are three important parameters in STM, the tunneling current  $I_t$ , voltage bias  $V_b$  and tip-sample distance  $z$ . Keeping one of them constant and varying the others can give us different types of spectra such as  $I(z)$ ,  $I(V_b)$  etc, in which conductance spectroscopy  $I(V_b)$  measures the tunneling current as a function of the bias voltage with a fixed tip sample distance. There are many studies on how to extrapolate the LDOS from the conductance spectra, such as Koslowski *et al.* (2007); Passoni *et al.* (2009).

The basis of the discussion is the following expression of the tunneling current (Appelbaum and Brinkman, 1969)

$$I(V_b) = A \int_0^{eV_b} T(E, V_b, z) \rho_s(E) \rho_t(E - eV_b) dE, \quad (1.7)$$

where  $\rho_s$  and  $\rho_t$  are the tip and the sample LDOS,  $A$  is a dimensional coefficient, and  $T$  is the barrier transmission coefficient.

From Eq. (1.7) the conductance  $dI/dV_b$  at a given bias can be calculated (Passoni *et al.*, 2009).

$$\frac{dI}{d(eV_b)} = A \{ T(eV_b, V_b, z) \rho_s(eV_b) \rho_t(0) + \int_0^{eV_b} \rho_s(E) \frac{d[T(E, V_b, z) \rho_t(E - eV_b)]}{d(eV_b)} dE \} \quad (1.8)$$

where the sample LDOS  $\rho_s(eV_b)$  is given by the first term and second term is a background term. Since transmission coefficient  $T$  and  $\rho_t$  vary with bias, there is no direct way to extract  $\rho_s$  from the differential conductance spectrum. Only when it is assumed that the tip LDOS  $\rho_t$  and transmission coefficient  $T$  do not change with the bias voltage, the LDOS of sample is directly related to the conductance spectrum, which means that

$$\frac{dI}{dV_b} \propto LDOS(eV_b, tip). \quad (1.9)$$

This is the reason why it is advantageous to work with a metallic tip: it is not only a good conductor but also has a relatively flat LDOS as a function of energy. Hence by scanning the tip over a sample, the spectral function  $\frac{dI}{dV_b}$  reflects the sample LDOS.

In our experiments, the conductance signal is recorded through a lock-in amplifier. The principle is that by adding a small modulation signal  $V_m \cdot \sin(\omega t)$  to the bias

voltage, the tunneling current can be expanded with the modulation signal as,

$$I_t(V_b, V_m \sin(\omega t)) = I_0 + \underbrace{\frac{dI_t(V_b)}{dV_b} \cdot V_m}_{\text{Lock-in signal}} \cdot \sin(\omega t) + \frac{d^2 I_t(V_b)}{dV_b^2} \cdot V_m^2 \cdot \underbrace{\frac{\sin^2(\omega t)}{(1 - 2 \cos(2\omega t))/2}}_{(1 - 2 \cos(2\omega t))/2} + \dots \quad (1.10)$$

where  $I_0$  is the tunneling current without the modulation signal. The third term of Eq. (1.10) is related with the inelastic tunneling current, which is not shown in the lock in signal as it has a frequency of two times of the modulation signal.

### 1.2.3 Double-barrier tunneling junction

Investigating colloidal QDs using STM naturally leads to the formation of a double-barrier tunneling junction (DBTJ) geometry, which is illustrated in Fig. 1.6(a). One junction is between the tip and QD and the other is between the QD and substrate. Theories about the DBTJ in the STM measurements have been discussed by many authors, e.g. Schönenberger *et al.* (1992, 1993a,b); Bakkers and Vanmaekelbergh (2000); Bakkers *et al.* (2001); Niquet *et al.* (2002).

The energy diagram of the same DBTJ is shown in Fig. 1.6(b). When there is a small bias, the Fermi energy of the tip and substrate are located at between the HOMO and LUMO gap of the QD. This means that current transport is not possible as direct tunneling between the tip and substrate does not occur at an appreciable rate. When a sufficiently positive (negative) bias is applied between the tip and substrate, the Fermi level of the tip becomes resonant with the LUMO (HOMO) of the QD. This leads to an opening of a tunneling channel and a step increase (decrease) in the measured current.

Further increase of the bias voltage causes no changes in the current until the next quantum confined energy level becomes resonant with the Fermi energy of the tip. Consequently,  $I(V_b)$  and  $dI/dV_b$  can be used to deduce the energy positions of the quantum confined states.

Electron tunneling from the tip of the STM to the substrate involves two steps, tunneling between the tip and QD and between the QD and the substrate. These processes proceed at certain rates (the number of electrons tunneling through the junction per unit time),  $\Gamma_{in}$  and  $\Gamma_{out}$ , respectively. In the STM configuration, the tunneling rate between the QD and substrate is fixed by the geometry. On the other hand, the tunneling rate between the tip and QD can be varied by moving the tip and/or changing the bias voltage. Typically, the junctions are asymmetric and we have  $\Gamma_{in} \ll \Gamma_{out}$  and the bias voltage drops mainly between the tip and QD.

In the case of  $\Gamma_{in} \ll \Gamma_{out}$ , which is called the shell-tunneling regime, electrons tunneling through the QD one-by-one and electron-electron interaction (between added electrons) does not occur. This means that the number of added electrons in the QD at any given is either 0 or 1.

In the shell-tunneling limit, the first electron can be added to the QD when the Fermi level of the tip aligns with the first electron level of the QD. This can be

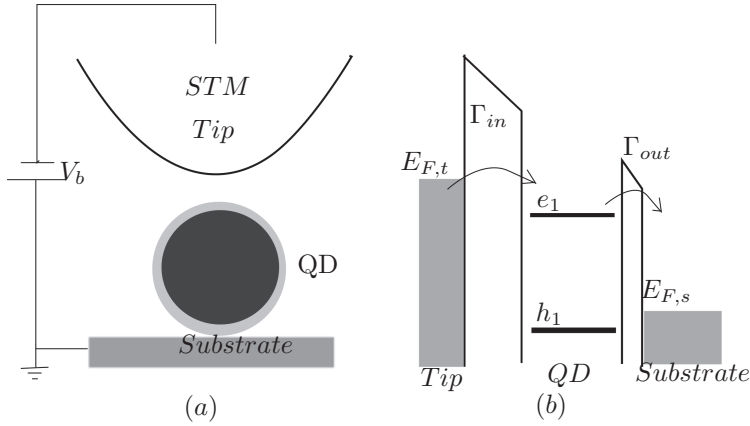


Figure 1.6: (a) An illustration of the tip-QD-substrate configuration in the STM measurement. (b) The energy configuration of the two tunneling junctions, where  $\epsilon_1$  is the lowest conduction level of the QD and  $h_1$  is the highest valence level. The Fermi energies of the tip and substrate have a relation as:  $E_{F,t} = E_{F,s} + eV_b$ .

expressed as

$$\eta V_b = \epsilon_{e1} + \Sigma_{e1}, \quad (1.11)$$

where  $\epsilon_{e1}$  is the energy of the LUMO of the QD and  $\eta$  is referred to as voltage lever arm and it is a parameter characterizing the potential distribution in the DBTJ (defined as the ratio between the potential drop between the tip and QD and the entire bias).  $\Sigma_{e1}$  is the electrostatic polarization energy associated with adding an electron onto the LUMO of the QD, which is also affected by the charge screening of the substrate and the tip.

Similarly, the first hole will be added when

$$\eta V_b = \epsilon_{h1} - \Sigma_{h1}, \quad (1.12)$$

where  $\epsilon_{h1}$  is the energy of the HOMO. The STM transport gap is

$$\eta \Delta V_g = \epsilon_{e1} - \epsilon_{h1} + \Sigma_{e1} + \Sigma_{h1}, \quad (1.13)$$

where  $\Sigma_{e1} \simeq \Sigma_{h1}$ . At positive bias, electrons can tunnel into the second lowest energy level when

$$\eta V_b = \epsilon_{e2} + \Sigma_{e2}. \quad (1.14)$$

The spacing between the first and second peak in the shell-tunneling regime directly gives the energy separation between the energy levels as the polarization energies  $\Sigma_{e1}$  and  $\Sigma_{e2}$  are equal to a good approximation.

In the opposite limiting case, when  $\Gamma_1 \gg \Gamma_2$ , it is possible to accumulate free carriers (more than one) inside the QD, once the associated energy barrier is overcome. This is referred to as the shell-filling regime. In this case we have to consider the Coulomb interactions between the free carriers inside the QD. A second electron is added to the level  $e1$  (two fold degenerate), when

$$\eta V_b = \varepsilon_{e1} + \Sigma_{e1} + J_{e-e}, \quad (1.15)$$

where  $J_{e-e}$  is the electron-electron Coulomb interaction energy between the added electrons and we neglect the spin interactions which are normally small. A third electron is added when

$$\eta V_b = \varepsilon_{e2} + \Sigma_{e2} + J_{e-e}. \quad (1.16)$$

If one wants to obtain quantitative estimates of the energetic positions of the quantum confined levels, the potential distribution in the DBTJ that is taken into account through  $\eta$  must be estimated. This is possible by solving the Laplace equation for a realistic STM tip - nanocrystal - substrate geometry (Jdira *et al.*, 2006; Liljeroth *et al.*, 2006a; Overgaag *et al.*, 2008).  $\eta$  depends on the tip radius of curvature and the QD dielectric constant, but has a typical value in the range of 0.75-0.8.

The STM gap  $\Delta E_{STM}$  can be compared with the optical gap  $\Delta E_{opt}$ ,

$$\begin{aligned} \Delta E_{opt} &= \varepsilon_{e1} - \varepsilon_{h1} + \Sigma_{e1} + \Sigma_{h1} + J_{e-h} \\ &= \Delta E_{STM} + J_{e-h} \end{aligned} \quad (1.17)$$

where  $J_{e-h}$  is the electron-hole attraction energy. The other difference is that optical transitions are subject to selection rules and hence not all transitions between valence band and conduction band levels are allowed. In STM and STS, in principle all the energy levels can be observed.

The discussion above only considered the elastic tunneling processes. However, there are cases where inelastic tunneling also needs to be taken into account. An example relevant to this thesis is the formation of polarons and the resulting polaronic transport in a DBTJ. It was realized in the early thirties of last century by Landau (1933) (see also Landau (1965)) that it is important to differentiate two essentially different transport cases: in the first one the electron moves ‘freely’ in the undistorted lattice and the other one, the electron is trapped in a self-induced distortion (polaronic transport). This distortion is caused by the electron interacting with the lattice through coupling with phonons. The transport must then be described in terms of quasiparticles named polarons by Pekar (1946), which correspond to the electron surrounded (dressed) by the lattice distortion. The electron-phonon coupling is strong in ionic materials and it will be relevant for the tunneling spectroscopy experiments on colloidal nanocrystals described in this thesis. In the case of polaronic transport, the single resonance corresponding to elastic tunneling through a quantum confined energy level is split into equally spaced peaks (see Fig. 1.7). The first peak corresponds to elastic tunneling and the subsequent peaks, spaced by the phonon energy, correspond to tunneling while exciting 1, 2, 3, etc. phonons. The relative amplitudes of these replica can be used to directly estimate the electron-phonon coupling strength.

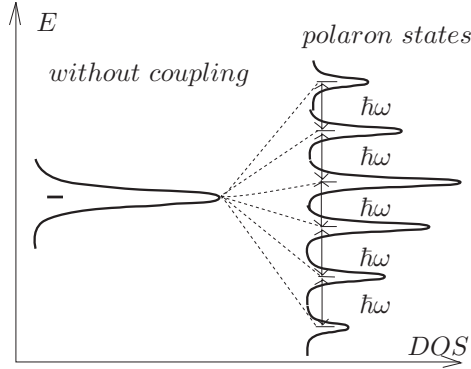


Figure 1.7: (Color online) An illustration of the polaron states caused by the electron-phonon coupling. For simplicity, here we only consider one type of phonon with a energy of  $\hbar\omega$ . Left: the energy state without electron-phonon coupling. Right: the polaron states caused by electron-phonon coupling where the inter-state spacing is the phonon energy,  $\hbar\omega$ . The curved show the relative density of states (DOS) of these states, which depend on the coupling strength.

#### 1.2.4 Calculation of electron-phonon coupling strength in QDs

In the polar materials such as CdSe, the dominating electron-phonon coupling mechanism is the Fröhlich coupling (Fröhlich, 1952; Fröhlich and Platzman, 1953) which was described by a dielectric continuum model by Huang and Zhu (1988). In the case of a spherical quantum dot, the coupling formula has been derived analytically by Klein *et al.* (1990).

A simple physics picture of the electron-phonon coupling can be given as follows. A free electron in a lattice field interacts with atoms through the Coulomb interaction. The kinetic energy of the electron is very large compared to that of the lattice atoms. The lattice can not respond instantaneously and can only ‘feel’ the average charge density of the electron, which makes lattice relax and decreases the electron energy. The total distortion energy, the Franck-Condon energy, can be related to the Huang-Rhys factor (Huang and Rhys, 1950) by the following equation

$$d_{FC} = \sum_k C_k \hbar\omega_{LO}, \quad (1.18)$$

where  $C_k$  is the Huang-Rhys factor for a single phonon mode. The Franck-Condon energy can be calculated through following equation,

$$d_{FC} = \left(\frac{1}{2} \int_V \rho_1(r) \phi_1(r) d\mathbf{r}\right)_\infty - \left(\frac{1}{2} \int_V \rho_2(r) \phi_2(r) d\mathbf{r}\right)_0, \quad (1.19)$$

where  $\phi_i(r)$  is the electrostatic potential induced by  $\rho_i(r)$  and  $\infty, 0$  are the high frequency and static cases, respectively.

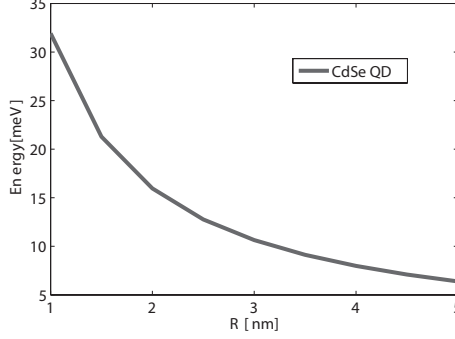


Figure 1.8: The electron-phonon interaction energy  $d_{FC}$  as a function of the radius  $R$  for a CdSe quantum dot. The parameters are  $\varepsilon(\infty) = 6.1$  and  $\varepsilon(0) = 9.15$  (Source see footnote).

We approximate the quantum dot as a potential well. For simplicity, we first set it as an infinite spherical quantum well and the charge density can be written as

$$\rho(r) = -\frac{e}{2\pi R} \left( \frac{\sin(\frac{\pi r}{R})}{r} \right)^2, \quad (1.20)$$

where  $R$  is the radius of the sphere.

Using the Gauss theorem, we have:

$$\begin{aligned} \frac{1}{2} \int_V \rho_1(r) \phi_1(r) d\mathbf{r} &= -\frac{\varepsilon}{2} \int_V \phi(r) \nabla^2 \phi(r) d\mathbf{r} \\ &= -\frac{\varepsilon}{2} \int_V \nabla(\phi(r) \nabla \phi(r)) d\mathbf{r} + \frac{\varepsilon}{2} \int_V \nabla \phi(r) \nabla \phi(r) d\mathbf{r} \\ &= -\frac{\varepsilon}{2} \int_S \phi(r) \nabla \phi(r) d\mathbf{s} + \frac{\varepsilon}{2} \int_V (\nabla \phi(r))^2 d\mathbf{r}. \end{aligned} \quad (1.21)$$

We set  $u = \frac{\pi r}{R}$ , then the electric field inside of the sphere can be written as,

$$\nabla \phi = \frac{e}{4\epsilon R^2} \frac{u - \sin(2u)/2}{u^2} \quad (1.22)$$

The first term of Eq. (1.21) in the high frequency limit and static cases cancels each other. Then the electron-phonon interaction energy can be written as,

$$d_{FC} = \frac{e^2}{4\pi\epsilon_0 R} \left( \frac{1}{\varepsilon(\infty)} - \frac{1}{\varepsilon(0)} \right) C \quad (1.23)$$

where  $C = \frac{2\pi - 2Si(2\pi) + Si(4\pi)}{4\pi} = 0.393$  and  $Si(x) = \int_0^x \frac{\sin \theta}{\theta} d\theta$ .

With Eq. (1.23), we calculated the Franck-Condon energy for spherical CdSe quantum dots and the result is shown in Fig. 1.8. A rigorous calculation of the charge density is not straight-forward as the lattice relaxation will influence the electron charge distribution, which in turn influences the lattice relaxation. This means that accurate calculations should be carried out self-consistently.

## 1.3 Introduction to AFM

### 1.3.1 Development of AFM

In the first article on AFM by Binnig *et al.* (1986), they described that they wanted to develop an instrument to be able to measure small forces as small as  $10^{-18} N$ . Even with the development in the following years, we have not reached this force resolution yet. But without any question AFM has turned into a powerful tool of modern science.

There are many similarities between STM and AFM, e.g. from the instrumentation point of view, both have a tip and a similar control unit to move it. The main difference is the feedback signal. STM tip-sample distance regulation depends on the tunneling current between the tip and the sample. In AFM the tip-sample distance is controlled by the interaction force between the tip and the sample. Since carrier transport is not necessary, the tip and sample can be insulators as well as conductors.

The design of AFM has been continually evolving since its invention. One example of that is how the deflection signal of the cantilever is detected. In the initial design (Binnig *et al.*, 1986), the motion of the cantilever was detected by a tunneling junction. This was soon changed to an optical approach (Martin *et al.*, 1987; Meyer and Amer, 1988). The idea there was to use a laser beam and photo diodes to detect the deflection of the cantilever. Later, advanced electronics were introduced to detect the deflection of the oscillating cantilever by Albrecht *et al.* (1991).

The interaction force gradually varies from attractive to repulsive as the tip is moved close to a surface as illustrated in Fig. 1.9. The relevant distance scale here is a few nanometers. There are many different operation modes for AFM. The two most commonly used are the contact mode and the non-contact mode, which is also called dynamic mode or tapping mode. Contact mode AFM is normally operated in the repulsive region. The cantilevers are soft and have a small spring constant  $k$ . Working in the repulsive region means the tip is close to the sample surface and there is a significant repulsive interaction between the tip apex and the region of the sample directly under the tip. For tapping-mode AFM, the tip is oscillating during scanning. This mode is normally operated in the attractive regime.

A simple illustration of the non-contact AFM (nc-AFM) working mechanism is shown in Fig. 1.10. The actuator can be made of a piezoelectric material. Alternating current electric signal is used to make the cantilever to oscillate. The detected deflec-

---

<sup>0</sup>Data taken from SpringerMaterials - The Landolt-Börnstein Database, volumes III/17B-22A-41B: Cadmium selenide (CdSe) dielectric constants. Madelung, O., Rössler, U., Schulz, M. (ed.)

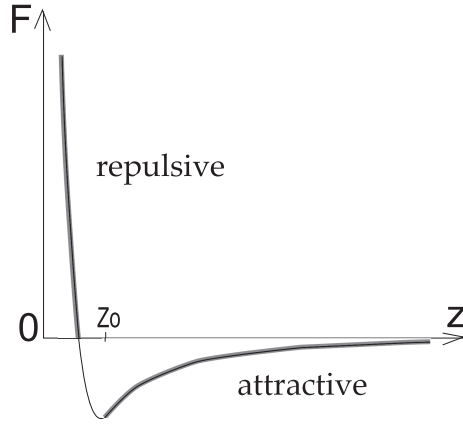


Figure 1.9: The interaction force between a tip and a surface as a function of the tip-sample distance. The long range attractive force arises from long range interaction such as van der Waals (vdW) interaction and static electromagnetic interaction. The repulsive forces include Pauli repulsion, chemical interaction etc.  $z_0$  is in the range of few Å and the typical interaction force is in the scale of  $nN$ .

tion signal is used for calculating the interaction force and also send to the control unit to regulate the cantilever oscillation amplitude or frequency.

For an ideal spring system with spring constant  $k$  and effective mass  $m$ , the resonance oscillation frequency is

$$f_0 = \frac{1}{2\pi} \sqrt{\frac{k}{m}}. \quad (1.24)$$

When an external load (force gradient) is applied to it, both its oscillation amplitude and resonance frequency will change.

### 1.3.2 Theory of nc-AFM

There are many review articles about the working mechanisms of AFM, such as Giessibl (2003); Abramovitch *et al.* (2007).

Different deflection signals can be used to control the tip-sample distance in non-contact AFM. Some instruments use amplitude, called amplitude modulation. There are also instruments using the variation of the cantilever oscillation frequency, called frequency modulation AFM. The low temperature STM/AFM used in the work presented in this thesis belongs to the second type.

Here we give the definition of quality factor ( $Q$ ) of the oscillator. It is an important parameter for characterizing the cantilever. The general definition is the energy stored in the oscillator over the energy supplied from outside per cycle to keep the oscillator

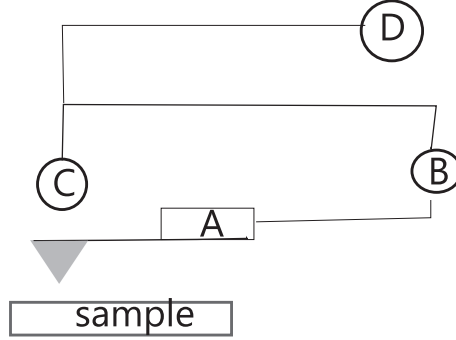


Figure 1.10: An illustration of the working mechanism of AFM. A is the actuator which oscillates the cantilever. B is the feedback loop. C is the deflection signal sensor. D is the signal used to calculate the interaction force.

oscillating with a constant amplitude

$$Q = 2\pi \times \frac{\text{Energy stored}}{\text{Energy dissipated}}. \quad (1.25)$$

When  $Q$  is very large ( $Q \sim f$ ), the following definition is applied.

$$Q = \frac{f}{\Delta f}, \quad (1.26)$$

where  $\Delta f$  is the full width at half maximum of the resonant spectrum.

To understand the principle of non-contact AFM, consider a damped harmonic oscillator with resonant angular frequency  $\omega_0$  and driven with an angular frequency  $\omega_d$  in  $z$  direction. The equation of motion can be written as (Albrecht *et al.*, 1991),

$$m\ddot{z} + \frac{m\omega_0}{Q}\dot{z} + m\omega_0^2 z = F_0 \cos(\omega_d t), \quad (1.27)$$

where  $m$  is the effective mass of the oscillator and  $F_0$  is the driving force amplitude. The solution of the equation is

$$z = A_0 \cos(\omega_d t + \theta_0), \quad (1.28)$$

where amplitude  $A_0$  and phase angle  $\theta_0$  are given by,

$$A_0 = F_0 G(\omega_d) = \frac{F_0/m}{\sqrt{(\omega_0^2 - \omega_d^2)^2 + (\omega_0 \omega_d / Q)^2}} \quad (1.29)$$

and

$$\theta_0 = \tan^{-1}\left(\frac{\omega_0 \omega_d}{Q(\omega_0^2 - \omega_d^2)}\right). \quad (1.30)$$



Figure 1.11: The changing of the oscillation frequency of a cantilever by an external force gradient  $dF_{ts}(z)/dz$  can be seen as the spring system in the right panel, where  $k_{ts}(z) = dF_{ts}(z)/dz$ .  $k$  is the spring constant of the cantilever and  $m$  is the effective mass.

In Eq. (1.29), function  $G(\omega)$  is called the response function.

The change of the oscillation frequency can be understood by the following analogy with a spring system. As illustrated in Fig. 1.11, the oscillating cantilever can be seen as a spring system with a spring constant  $k$ . When the cantilever is moved close to another object, the external force gradient can be described as another spring attached to the cantilever with effective spring constant  $\frac{dF_{ts}(z)}{dz} = k_{ts}(z)$ . This will cause a shift of the resonant frequency  $\Delta f = f - f_0$  of the spring system. One thing to note here is that  $k_{ts}(z)$  is not a constant but a function of tip sample distance.

For an AFM controlled by amplitude feedback, the cantilever oscillates slightly off its resonant frequency  $\omega_0$ . The force between the tip and the sample  $dF_{ts}/dz$  will shift the resonance frequency to  $\omega'_0$ . This will create a change in the oscillation amplitude  $\Delta A$ . The disadvantage of amplitude control is that the time constant for an amplitude change is  $2Q/\omega_0$  (Albrecht *et al.*, 1991). If the  $Q$  is very high, which is typically the case in UHV, long reaction time will limit the scanning speed.

In frequency modulation (FM) nc-AFM, one can overcome the long reaction time problem of amplitude modulation nc-AFM. The working principle is to excite the cantilever at a fixed amplitude  $A$  and the interaction between tip and sample will only change the resonance frequency of the cantilever. The advantage of FM-AFM is that its time constant is of the order of one oscillation cycle,  $2\pi/\omega_0$ .

There are many new developments in the AFM probing techniques. Today, AFM can not only be used to probe the surface topography, but also for atomic manipulation, small force measurements etc (Oyabu *et al.*, 2003; Sugimoto *et al.*, 2005; Ternes *et al.*, 2008). In order to image individual atoms by AFM, the short range forces (chemical bonding and Pauli repulsion) have to contribute significantly to the change of the regulation signal. While it is possible to achieve this with conventional FM-AFM as demonstrated for example in experiments of Sugimoto *et al.* (2007), it is beneficial to use as small oscillation amplitudes as possible.. In this case, short range forces act on the tip throughout the tip oscillation cycle. For a stable AFM operation with very small tip-sample oscillation amplitudes, the cantilever needs to

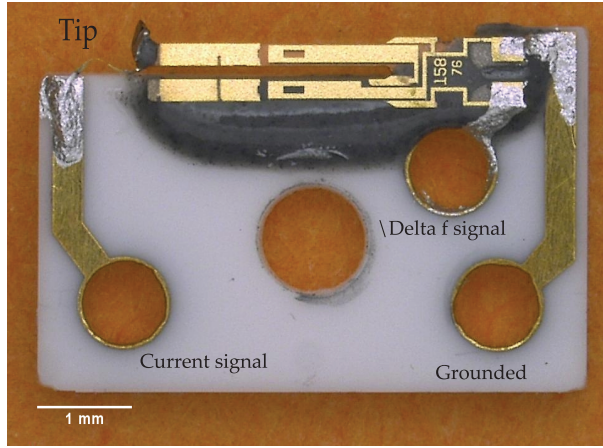


Figure 1.12: An image of a tuning fork sensor<sup>1</sup>.

be very stiff, i.e. have a high spring constant. One way to achieve this is to use a quartz tuning fork force sensor. It has a very large spring constant (about  $1800\text{ N/m}$ ) (Giessibl, 2000) and can oscillate at very small amplitude ( $< 1\text{ \AA}$ ) with a very large quality factor. At the same time, electrodes on the tuning fork can be used for all-electrical detection of these small oscillation amplitudes. A picture of the tuning fork sensor is shown in Fig. 1.12. The tuning forks used in AFM are the same as those in a quartz watch and have a resonance frequency of about  $32\text{ kHz}$ . In the tuning fork sensor for AFM, one prong is fixed on a white ceramic base. Then the resonance frequency of the other prong is smaller than  $32\text{ kHz}$ . The sensors in our experiments have a resonance frequency around  $24\text{ kHz}$ .

For a homogeneous cantilever with dimensions of  $w, t, L$ , the spring constant  $k$  is given by (Cleveland *et al.*, 1993)

$$k = \frac{Ywt^3}{4L^3}, \quad (1.31)$$

where  $Y$  is the Young's modulus. The first eigenmode of the transverse deflection a cantilever fixed in one end (as shown in Fig. 1.13, oscillating perpendicular to the  $L \times w$  plane) is given by (Rast *et al.*, 2000; Rabe *et al.*, 1996)

$$f_0 = 0.162 \frac{t}{L^2} \sqrt{\frac{Y}{\rho_d}}, \quad (1.32)$$

where  $\rho_d$  is the density of the beam material. If an extra small mass  $M$  is added to the free end of the cantilever, the eigenmode resonance frequency will have an

<sup>1</sup>Adapted from [http://www.physik.uni-regensburg.de/forschung/giessibl/neu/research/qplus-sensor\\_e.phtml](http://www.physik.uni-regensburg.de/forschung/giessibl/neu/research/qplus-sensor_e.phtml)

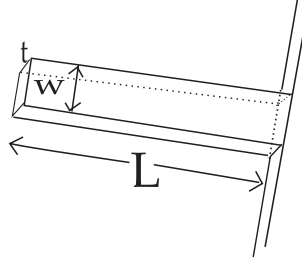


Figure 1.13: Cantilever made by a uniform beam fixed at one end.

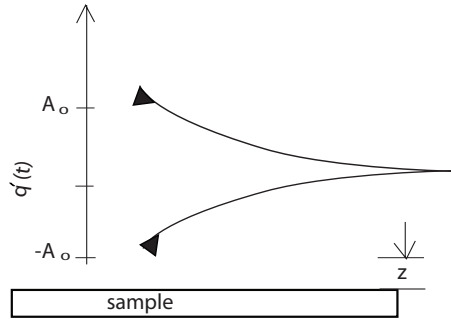


Figure 1.14: Illustration of the cantilever oscillation near a sample surface.  $z$  is the tip-sample distance at the closest point.  $A_0$  is the oscillation amplitude.

linear dependence on  $1/\sqrt{M + m^*}$ , where  $m^*$  is the effective mass of the cantilever (Cleveland *et al.*, 1993).

### 1.3.3 Force spectroscopy with FM-AFM

In many cases one wants to quantitatively measure the interaction force between the tip and the sample, the so called force-distance curve. Here we consider the case of frequency modulation AFM. In order to do that, we need to know the relation between frequency shift and the force applied on the tip. The situation is depicted in Fig. 1.14. Under the assumption that the frequency shift  $\Delta f$  is much smaller than the resonance frequency of the cantilever  $f_0$ , the relation between  $\Delta f$  and the tip-sample interaction force  $F_{ts}$  is given by Giessibl (1997),

$$\Delta f = -\frac{f_0}{kA_0^2} \langle F_{ts}q' \rangle, \quad (1.33)$$

where  $k$  is the spring constant and the other variables are illustrated in Fig. 1.14. The average is taken over a cycle. To write it down explicitly,

$$\Delta f(z) = -\frac{f_0}{\pi k A_0} \int_{-1}^1 F_{ts}(z + A_0(1+u)) \frac{u}{\sqrt{1-u^2}} du, \quad (1.34)$$

where  $u$  is the integration variable.

In order to apply the equation to the experiments, we need to deduce the relation between the interaction force  $F_{ts}$  and the frequency shift  $\Delta f$ . It is necessary to invert Eq. (1.34) to get a formula of  $F_{ts}$  for all possible amplitudes. This has been derived by Sader and Jarvis (2004) with Laplace and inverse Laplace transforms. The exact formula is

$$F_{ts}(z) = L\left\{\frac{kA_0}{T(\lambda A_0)} L^{-1}\left\{\frac{\Delta f(z)}{f_0}\right\}\right\}, \quad (1.35)$$

where  $L\{\}$  and  $L^{-1}\{\}$  refer to Laplace and inverse Laplace transforms,  $T(x) = I_1(x) \exp(-x)$  and  $I_n(x)$  is the modified Bessel function of the first kind of order  $n$ . By using an approximation of  $T(x)$ ,

$$T(x) = \frac{x}{2} \left(1 + \frac{1}{8} \sqrt{x} + \sqrt{\frac{\pi}{2}} x^{3/2}\right)^{-1}, \quad (1.36)$$

the explicit formula of  $F_{ts}(z)$  as a function of frequency shift is deduced as

$$F_{ts}(z) = \frac{2k}{f_0} \int_z^\infty \left(1 + \frac{A_0^{1/2}}{8\sqrt{\pi(t-z)}}\right) \Delta f(t) - \frac{A_0^{3/2}}{\sqrt{2(t-z)}} \frac{d\Delta f(t)}{dt} dt. \quad (1.37)$$

This can be further integrated to yield the interaction potential  $V_{ts}(z)$ .

In the case when the cantilever oscillation amplitude is very large or small,  $F_{ts}$  can be written down explicitly (Giessibl, 1997; Durig, 1999). For example, when the oscillation amplitude is small enough such that the force gradient is roughly constant during the oscillation cycle,

$$\Delta f(z) \simeq -\frac{f_0}{2k} \frac{dF_{ts}(z)}{dz}, \quad (1.38)$$

$F_{ts}(z)$  can be written as (Sader and Jarvis, 2004)

$$F_{ts}(z) = \frac{2k}{f_0} \int_z^\infty \Delta f(t) dt, \quad (1.39)$$

where  $k$  is the spring constant of the cantilever.

### 1.3.4 Oscillation amplitude effects

In AFM, the long-range interaction involves many atoms of the tip and the sample, while the short-range interaction is determined by the last atoms of the tip and a

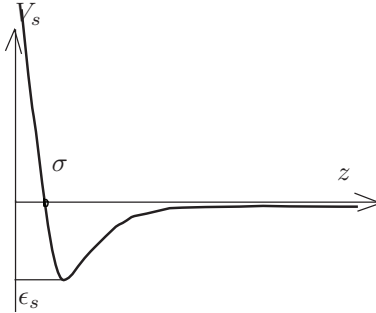


Figure 1.15: Illustration of the Lennard-Jones potential and the variables used in Eq. (1.40).

few atoms of the sample. Consequently, the tip shape has a strong effect on the the strength of the long-range force component. Blunt tips may favor a larger long range interaction with the substrate with respect to the short range interaction in the attractive region. In the case of a metallic tip, the structure of the tip apex is to a certain extent an unknown parameter in our measurements. However modifying the tip apex by small molecules can be used to obtain an atomically well-defined AFM tip termination (Gross *et al.*, 2009).

Here, we study the influence of the oscillation amplitude on the accuracy with which the tip-sample force can be measured. We start with a realistic tip-sample interaction. Then we calculate the frequency shift as a function of the tip-sample distance at different oscillation amplitudes. Afterwards, we calculate the interaction forces through different approximations and compare them. This can be used to establish the range of validity of the different approximations.

For simplicity, we assume that the interaction between the tip apex and the sample surface behaves as a Lennard-Jones interaction in  $z$  direction. The interaction potential is

$$V_s(z) = 4\epsilon_s \left( \left( \frac{\sigma}{z} \right)^{12} - \left( \frac{\sigma}{z} \right)^6 \right), \quad (1.40)$$

where  $\sigma$  is a distance scale parameter where and  $\epsilon_s$  is the depth of the interaction potential well.

For the long-range interaction between the body part of the tip (without the tip apex) and the sample, we assume that the interaction has following form,

$$V_l(z) = \epsilon_l \left( \frac{d_l}{z + d_0} \right)^3, \quad (1.41)$$

where  $d_l$  and  $d_0$  are distance parameters which describe the interaction decay length in  $z$  direction and  $\epsilon_l$  is the interaction energy parameter.

We use the following parameters for calculation:  $\epsilon_s = 20 \text{ meV}$ ,  $\sigma = 4 \text{ \AA}$ ,  $\epsilon_l =$

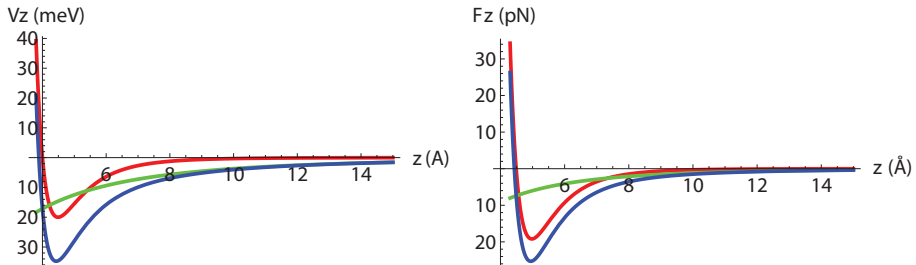


Figure 1.16: Interaction between the tip and the sample. Left graph shows the interaction potential. Red: Interaction potential between the tip apex and the sample. The green curve depicts the long range interaction between the body part of the tip and the sample. The blue curve presents the total interaction potential. The right graph shows the corresponding force contributions.

$-100 \text{ meV}$ ,  $d_t = 5 \text{ \AA}$  and  $d_0 = 5 \text{ \AA}$ . Using these parameters, the interaction potentials and forces are shown in Fig. 1.16.

We use the following parameters for the AFM sensor: resonance frequency  $f_0 = 24 \text{ kHz}$  and spring constant of the cantilever  $k = 1800 \text{ N/m}$ . Then the frequency shift at different tip sample distance according to Eq. (1.34) can be calculated for different amplitudes (see Fig. 1.17).

One way to calculate the interaction force is using the small amplitude limit. The corresponding equation is Eq. (1.38). We re-calculated the interaction using this equation for  $\Delta f$  signal with different amplitudes. The results are shown in Fig. 1.18. From the graph we can see for amplitudes larger than  $50 \text{ pm}$ , we already observe a considerable derivation. For amplitude smaller than  $50 \text{ pm}$ , the results agree well with the original force. But there is still a large deviation at short distances and large repulsive force region. This results in a shallower slope compared with the original force.

Instead of Eq. (1.39), it is also possible to use the method of Sader and Jarvis (2004), which takes into account the effects of different oscillation amplitudes rigorously. Results calculated from Eq. (1.37) are shown in Fig. 1.19. From the figure we can see the Sader-Jarvis method gives a very good agreement on both short and long tip-sample distances. However, close to the minimum of the force-distance curve, the results still show small deviations.

## 1.4 Scope and outline of this thesis

This thesis can be divided into three main parts. The first part focuses on the experiments on the electronic structure of colloidal semiconductor nanocrystals studied by LT-STM, which includes chapters 2 and 3. Experiments aimed at a direct measurement of the electron-phonon coupling in CdSe quantum dots are discussed in

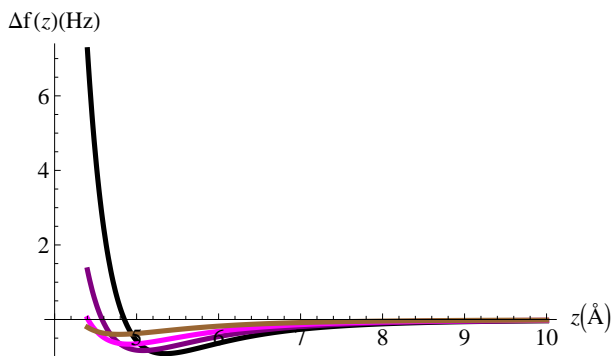


Figure 1.17: Calculated frequency shift signals by Eq. (1.38) with the total force shown in Fig. 1.16 for oscillation amplitudes of 10  $\mu\text{m}$  (Black), 50  $\mu\text{m}$  (Purple), 100  $\mu\text{m}$  (Magenta) and 200  $\mu\text{m}$  (Brown).

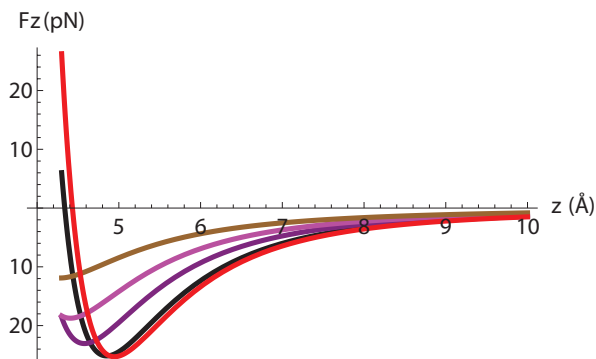


Figure 1.18: Calculated interaction force from frequency shift signals generated with different oscillation amplitudes by Eq. (1.38). 10  $\mu\text{m}$  (Black), 50  $\mu\text{m}$  (Purple), 100  $\mu\text{m}$  (Magenta) and 200  $\mu\text{m}$  (Brown). The red curve is the initial interaction force used in the calculations.

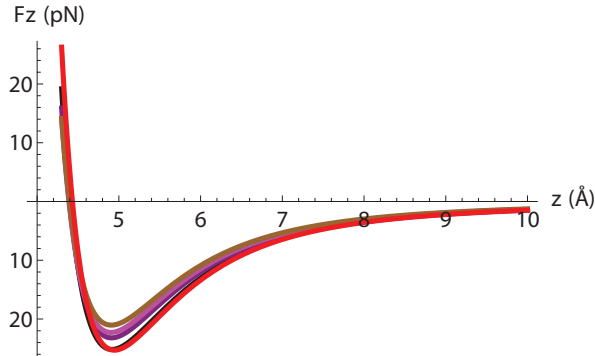


Figure 1.19: Calculated interaction force from frequency shift signals by Sader-Jarvis method for oscillation amplitudes: 10  $pm$  (Black) and 50  $pm$  (Purple), 100  $pm$  (Magenta) and 200  $pm$  (Brown). The red curve is the initial total interaction force. The black curve is almost fully overlapped with the red one.

Chapter 2. It is shown that the electron-phonon coupling can be detected from the conductance resonances. The strength of the electron-phonon coupling is enhanced by wavefunction confinement. Chapter 3 discusses the electronic structure of core-shell quantum dots.

The second part of this thesis deals with the properties of epitaxial graphene grown on an Ir(111) surface. We explored the origin of the graphene moiré pattern using LT-STM and FM-AFM. We found that in order to extract the real corrugation of the moiré pattern from the AFM images, the vdW interaction between the tip and the Ir(111) substrate has to be considered. These results will be discussed in Chapter 4. In Chapter 5, I will discuss our STM results on the electronic structure of graphene nanoflakes on an iridium surface. In this study we found that the low energy electrons still behave as having zero effective mass. The confined states are analogous to the solutions of the two-dimensional “particle-in-a-box” problem for relativistic fermions.

Last part of the thesis is about experiments on probing intermolecular interaction between two carbon monoxide molecules with nc-AFM, which will be included in Chapter 6. In this study we found that the relaxation of the molecules has to be considered for both topography imaging and calculation of the tip-sample interaction force.



---

## Chapter 2

# Electron-phonon coupling in CdSe nanorods

### 2.1 Introduction

Quantum dots (QDs) refer to the nanostructures which contain about  $10^2 - 10^9$  atoms and have a size between a few angstrom to micrometers. These include metal clusters, small insulator and semiconductor crystals and small structures made through electrical or mechanical methods. What they all have in common is that their electrical properties show quantum effects. In the following discussion, we will focus on semiconductor QDs. They can be made by self assembled growth (Tersoff *et al.*, 1996), wet chemical synthesis (e.g. see Dabbousi *et al.* (1997)) and lithographic techniques (Petta *et al.*, 2005). Colloidal QDs refer to the QDs made by chemical synthesis.

In a semiconductor, almost all the electrons are strongly bonded with the nucleus. Only small numbers of carriers can move "freely" inside the semiconductor because the periodic potential of the lattice cannot confine them. The interaction between the lattice and free electrons gives the electrons an effective mass  $m^*$  and changes the dispersion relation into:  $E = p^2/(2m^*)$ . This has a strong effect on the properties of the material. For example, in CdSe, the effective mass of the electron is  $0.11 m_e$  and for a free electron with energy of  $1 eV$  the characteristic length of the electron wave is  $h/\sqrt{2m^*E} = 3.7 nm$ . When the length is comparable to the size of the structure, quantum effects have to be considered.

The behavior of free electrons in a semiconductor QD can be approximated by the textbook particle-in-a-box model. These free carriers confined in the QDs show the quantum confinement effect: the energy of the electronic states is discrete and the energy splitting  $\Delta E$  is proportional to  $1/L^2$ , where  $L$  is the diameter of the QDs. For electrons confined in a three-dimensional spherical potential well, their wavefunctions are normally named by their spatial symmetry, such as  $1s, 2s, 2p, 3s, \dots$ , which is borrowed from atomic physics and this is the reason that QDs are called

artificial atoms (Kastner, 1993). If there are more than one free carrier inside a QD, the interactions between these carriers need to be considered for understanding the behavior of the QD. The well separated energy levels in these QDs provide special optical and electrical properties (Klimov, 2007; Pandey and Guyot-Sionnest, 2008; Talapin and Murray, 2005; Banin *et al.*, 1999; Urban *et al.*, 2007; Delerue and Lannoo, 2004) and many applications have been proposed. Colloidal QDs have been used for biosensors (Alivisatos, 2004; Alivisatos *et al.*, 2005; Medintz *et al.*, 2005; Michalet *et al.*, 2005), optical sensors (Konstantatos *et al.*, 2006), electronic transistors (Klein *et al.*, 1997) and solar cells (Robel *et al.*, 2006) etc.

Free carriers in a semiconductor can cause a local lattice deformation due to the interaction between the carriers and the lattice and the deformation is enhanced due to the confinement of the carriers inside the QD (Delerue and Lannoo, 2004; Wingreen *et al.*, 1989; Hameau *et al.*, 1999; Melnikov and Fowler, 2001; Jdira *et al.*, 2008b). The interaction can be considered as the free carrier coupling with phonons and the resulting quasiparticle (electron dressed by the lattice deformation) is called a polaron (Pekar, 1946). The coupling is central for understanding the transport and energy relaxation processes in nanostructures (B. J. LeRoy, 2004; Klein *et al.*, 1997; Yu *et al.*, 2003; Bakkers *et al.*, 2001; Schaller *et al.*, 2006; Hendry *et al.*, 2006). It is an intrinsic process (Pandey and Guyot-Sionnest, 2008) and relates to the temperature dependence of the electron transport in the QD superlattices (Houtepen *et al.*, 2008; Yu *et al.*, 2004).

Even though there are many theoretical results on electron-phonon coupling in QDs (Delerue and Lannoo, 2004; Wingreen *et al.*, 1989; Hameau *et al.*, 1999; Melnikov and Fowler, 2001), there is no clear-cut experimental data about electron-phonon coupling in the QDs (Boebinger *et al.*, 1990; Carpenter *et al.*, 2006). In this chapter, we discuss our study on the electronic properties of CdSe colloidal QDs. We measure the single dot DOS under shell-tunneling regime and extract the electron-phonon coupling strength for different orbital symmetries.

CdSe has the wurtzite crystal structure as shown in Fig. 2.1 and it is a polar material because of the charge transfer between cadmium and selenium atoms. The long axis of the nanorod is along the (0001) direction of the crystal. The CdSe lattice can host two types of phonons: acoustic and optical phonons. In an ionic crystal, optical phonons are caused by the cation and anion at neighboring lattice sites moving against each other. The eigenenergies of the optical phonons are larger than those of acoustic phonons and have a flatter dispersion (Corso *et al.*, 1993). Both types of phonon have transverse and longitudinal modes.

The main coupling mechanism between electron and longitudinal optical phonons (LO-phonon) has been discussed by many authors, e.g. Wingreen *et al.* (1989); Gadzuk (1991); Alivisatos *et al.* (1989); Klein *et al.* (1990). The electrons couple with LO-optical phonons through the Fröhlich interaction (Fröhlich, 1952).

The coupling principle can be understood intuitively as that in a polar material, free electrons interact with the polar electric field of the lattice caused by the electrons themselves. The interaction is characterized by a dimensionless constant  $\alpha$ , the Fröhlich coupling constant, and it can be deduced from the following arguments. The

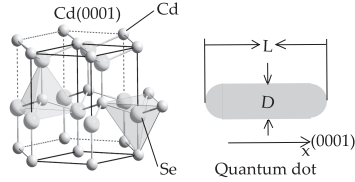


Figure 2.1: (Color online) (Left) Wurtzite lattice structure of CdSe crystal and (right) the illustration of the structure of the QDs that were probed in this experiment. (Adapted from [http://en.wikipedia.org/wiki/File:Wurtzite\\_polyhedra.png](http://en.wikipedia.org/wiki/File:Wurtzite_polyhedra.png))

self-energy potential of a free electron in a polar material can be written as

$$V(r) = \begin{cases} -\frac{e^2}{r} \frac{1}{\bar{\epsilon}}, & \text{if } r \geq r_0 \\ -\frac{e^2}{r_0} \frac{1}{\bar{\epsilon}}, & \text{if } r < r_0, \end{cases} \quad (2.1)$$

where  $r_0$  is a distance below which the material is fully polarized, and  $1/\bar{\epsilon} = 1/\epsilon_\infty - 1/\epsilon_0$  and  $\epsilon_\infty$  and  $\epsilon_0$  are the dielectric constants at the high frequency and static cases. If the crystal lattice has an eigenfrequency of  $\omega$ , the energy of the corresponding phonon is  $\hbar\omega$ . Once the electron couples with the phonon, we have a relation as following

$$\frac{\Delta p^2}{2m^*} = \hbar\omega. \quad (2.2)$$

From the uncertainty principle in quantum physics, we have

$$\sigma_x \cdot \sigma_p \geq \hbar/2. \quad (2.3)$$

By combining these two equations and assuming  $\sigma_p \simeq \Delta p$ , we can have a unit length

$$l_c = 2\sigma_x = \sqrt{\frac{\hbar}{2m^*\omega}}. \quad (2.4)$$

The Fröhlich coupling constant  $\alpha$  can be written as (Devreese, 2000)

$$\alpha = \frac{1}{2} \frac{e^2}{l_c \bar{\epsilon}} \cdot \frac{1}{\hbar\omega} \quad (2.5)$$

$$= \frac{e^2}{\bar{\epsilon}} \sqrt{\frac{m^*}{2\omega\hbar^3}}. \quad (2.6)$$

When  $\alpha$  is smaller than 1, we say the coupling is weak.

The Fröhlich constant  $\alpha$  is a microscopic parameter. In order to relate experiment results to the coupling strength, Huang-Rhys parameter and Franck-Condon energy shift are normally used and they have a relation, as discussed in previous chapter,

$$d_{FC} = \sum_k S_{hr,k} \hbar \omega_{LO}, \quad (2.7)$$

where  $S_{hr,k}$  is the Huang-Rhys parameter for a single phonon mode characterized by an parameter  $k$  and  $d_{FC}$  is the Franck-Condon energy. Huang-Rhys parameter is proportional to the Fröhlich coupling constant in the case of the QD (Hopfield, 1959)

$$S_{hr} \propto \alpha \sum_k \left( \frac{\rho_k}{|k|} \right)^2, \quad (2.8)$$

where  $k$  is the wavevector of phonon and  $\rho_k$  is the  $k_{th}$  Fourier coefficient of the electron charge density. More detailed theoretical treatment of the electron-phonon coupling can be found in many articles, such as Huang and Zhu (1988); Klein *et al.* (1990); Devreese (2000).

## 2.2 Experimental

We have carried out LT-STM experiments on arrays of colloidal CdSe QDs (3 and 6 nm in diameter) and mixtures of dot and rod shaped QDs (diameter of 3.5 nm and an aspect ratio between 1 and 4). The QDs were synthesized with chemical method (Grodzińska *et al.*, 2011) and deposited on highly oriented pyrolytic graphite (HOPG) or flame annealed gold thin film substrate as described previously by Jdira *et al.* (2008a,b). STM experiments were carried out at LHe temperature (4.7 K) with cut PtIr tips (typical bias of 2.5V and setpoint current of 10 pA). The conductance spectra were acquired with decreased bias and increased setpoint (typically 1.5 V/100-200 pA) and the conductance was recorded simultaneously using a lock-in amplifier (amplitude 3mV rms. and frequency 300Hz). We performed STS on several samples; in total ca. 100 QDs were investigated. A typical large scale STM image is shown in Fig. 2.2.

## 2.3 Results and discussion

One set of conductance spectra ( $dI/dV_b$ ) for a CdSe nanorod is shown in Fig. 2.3; we immediately notice the progression of peaks corresponding to each of the quantum confined energy levels. These peaks are equally spaced and strongly resemble the expected response when the electron level is coupled with phonon modes (Delerue and Lannoo, 2004; Wingreen *et al.*, 1989). This coupling between the confined electron and a lattice deformation results in the formation of a polaronic DOS, where each one-electron configuration is characterized by several vibrational states, separated by the phonon energy.

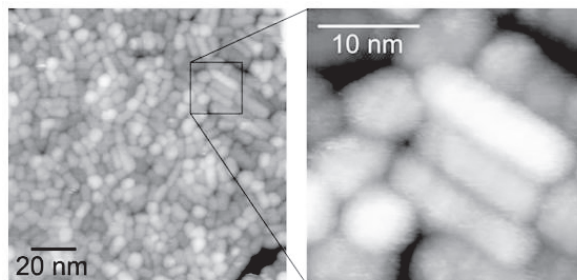


Figure 2.2: A large scale STM topography image of a monolayer CdSe QDs on HOPG. Right: Zoom in image of a sample region with several long nanorods. Set point:  $V_b = 3V$ ,  $I_t = 10pA$ .

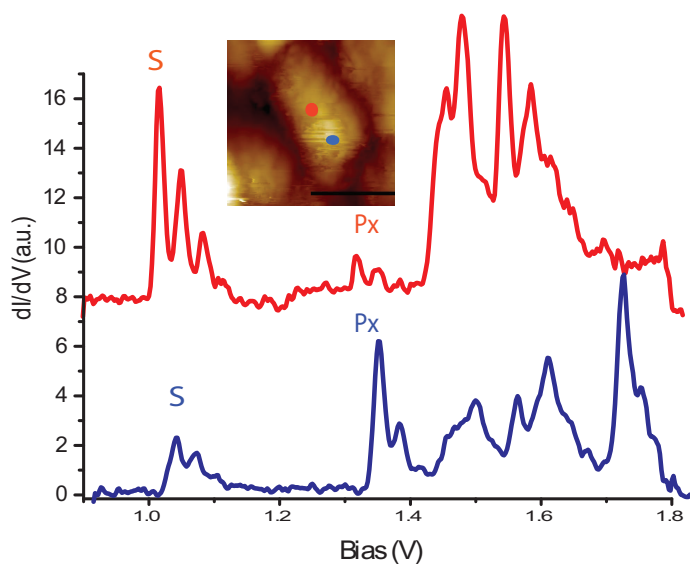


Figure 2.3: Conductance spectra on a CdSe nanorod with aspect ratio of 3. Red curve is the conductance spectrum taken at the center of the QD. Blue spectrum is taken at one end of the QD (with a constant shift in y direction). Inset: The topography of the QD and the positions where the spectra were acquired. Scale bar: 4nm.

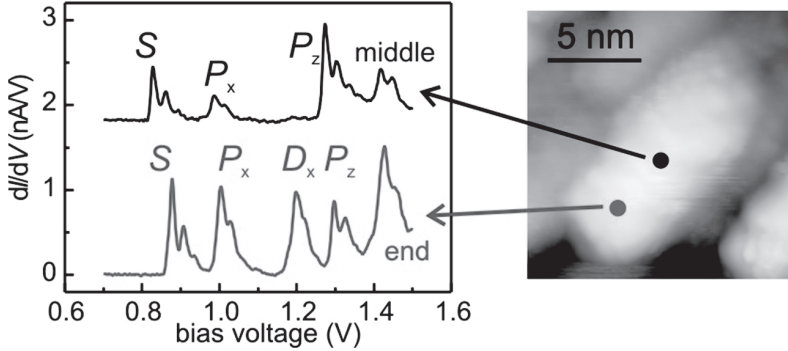


Figure 2.4: Spectroscopy on a CdSe nanorod with an aspect ratio of ca. 2.5 showing identification of the levels based on spatial resolved measurements. The positions where the spectra were recorded are indicated in the right image.

The coupling among the CdSe QDs is weak (Jdira *et al.*, 2008a) and we can neglect the inter-QD electronic coupling in the experiment and consider the system as a double-barrier tunneling junction as described in the previous chapter. The ratio  $\Gamma_{in}/\Gamma_{out}$  will determine the number of additional electrons in the QD. Under the shell-tunneling conditions, electrons tunnel through the QD one by one and electron-electron interactions do not occur. In this case, the peaks in the tunneling spectrum reflect the polaronic DOS, and the electron-phonon coupling strength can be directly quantified based on the amplitudes of the elastic peak and replica.

The dependence of the electron-phonon coupling strength on the orbital symmetry can be conveniently studied in rod shaped QDs. The crystal shape asymmetry along the  $x$  axis (Fig. 2.1) will break the degeneracy of the  $P$  (and higher lying) levels and cause the  $P_x$  state to decrease in energy with respect to  $P_y$  and  $P_z$  states. Depending on the aspect ratio of the nanorod, the spectrum can be rather complex with for example  $D_x$  and  $P_z$  states having similar energy. These states can be distinguished by probing their symmetry with spatial resolved spectroscopy experiments (Millo *et al.*, 2001) as illustrated in Fig. 2.3: just below the rod midpoint, we are close to a node of the  $P_x$  and  $D_x$  states, while the  $P_z$  state has significant weight. Conversely, at the end of the nanorod, resonances corresponding to  $P_x$  and  $D_x$  states have higher amplitude than the one corresponding to the  $P_z$  state. As can be seen from Fig. 2.4, we can resolve the phonon replica of all the levels, and hence directly quantify the electron-phonon coupling strength for orbitals with different symmetry.

In the case of a single phonon mode, theory predicts a series of equally spaced peaks (spacing  $\hbar\omega$ ) with the intensity of the  $n$ th peak being proportional to  $S_{hr}^n/n!$ , where  $S_{hr}$  is the dimensionless Huang-Rhys parameter. For comparison with experiments, the theoretical response is broadened by Gaussians. We show two examples in Fig. 2.5(a); in both cases, there is quantitative agreements between theory and experiment.

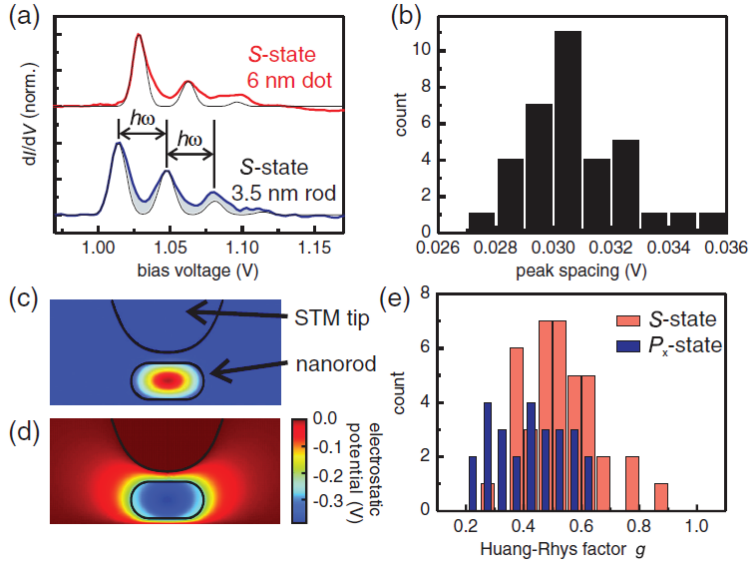


Figure 2.5: Analysis of the electron-phonon coupling strength. (a) Experimental data for 6 nm spherical dot and 3.5 nm diameter nanorod (aspect ratio ca. 2) along with the fits to a theory with a coupling strength of  $S_{hr} = 0.35$  (dot) and  $S_{hr} = 0.62$  (rod). (b) Distribution of the spacing of the phonon replica. (c) Solution of the Schrödinger equation for a nanorod (diameter 3.5 nm, aspect ratio 2) in the STM-substrate junction. (d) The resulting electrostatic potential distribution based on the solution of the Poisson equation. (e) Electron-phonon coupling strength for the  $S$  and  $P_x$  states measured on several nanorods.

The fitting yields spacings of the replica of 34 and 33  $mV$ , coupling strengths  $S_{hr}$  of 0.35 and 0.62 for the dot and rod, respectively.

There is a small but systematic difference between the theoretical predictions and the experimental results. We always observe the first resonance to be slightly asymmetric and broader on the higher bias side, see Fig. 2.5(a). This is likely to be caused by coupling to other (acoustic) phonon modes with smaller energies. In addition, the replicas are broader than the elastic resonance; this might indicate some dispersion in the phonon energies or life-time broadening of the vibrationally excited states due to the presence of rapid relaxation processes (in the sub-ps time scale).

In order to remove the broadening due to modulation voltage  $V_{ac}$ , we measured how the FWHM of a resonance depends on the modulation voltage. Using the

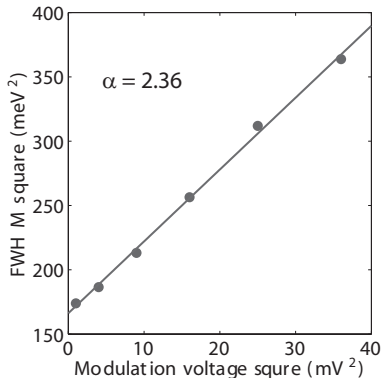


Figure 2.6: FWHM of resonance peak and the modulation voltage.

fitting method of Lauhon and Ho (2001),

$$W^2 = W_0^2 + W_T^2 + (\alpha V_{ac})^2, \quad (2.9)$$

where  $W_0$  is the intrinsic broadening plus the broadening caused by coupling with phonons,  $W_T$  is the thermal broadening and  $\alpha$  is a fitting parameter, we fitted the data (see Fig. 2.6) and found  $\alpha$  to be 2.36. According to Lambe and Jaklevic (1968), the thermal broadening contribution is about  $5.4 kT$ . The value is around  $2 meV$  if we assume that the QD under the tip has a temperature of  $4.7 K$ . With this, we find that  $W_0$  is about  $13 meV$ .

We show a histogram of the measured peak spacings over several samples in Fig. 2.5(b). The distribution is strongly peaked around  $31 mV$ . In order to convert this number to the true energy scale, the potential distribution in the tip-QD-substrate junction has to be taken into account. Based on the solution of the Poisson equation for a realistic tip-QD-substrate geometry (Delerue and Lannoo, 2004; Liljeroth *et al.*, 2006a; Jdira *et al.*, 2008a), ca. 85% of the bias voltage drops over the tip-QD junction, and hence, the bias voltage has to be multiplied by 0.85 to convert it to the energy scale. This gives an energy spacing of  $26 meV$ , in excellent agreement with the known LO-phonon energy of CdSe (Alivisatos *et al.*, 1989; Klein *et al.*, 1990; Tanaka *et al.*, 1992). As discussed above, there is further theoretical evidence that the electrons indeed couple to the LO-phonons. For a spherical QD, the coupling strength can be estimated analytically in the effective mass approximation (Delerue and Lannoo, 2004; Melnikov and Fowler, 2001; Jdira *et al.*, 2008b). Numerical simulations can be used to take into account the effects of finite confining potential, orbital symmetry, dot shape and dielectric environment on  $S_{hr}$ . The coupling strength for this Fröhlich coupling is given by  $S_{hr} = d_{FC}/\hbar\omega$  where  $d_{FC}$  is the relaxation energy of the crystal lattice due to the addition of the electron, i.e., formation of a polaron. This energy

can be estimated as

$$d_{FC} = \frac{1}{2} \left\{ \left[ \int \rho(\mathbf{r})\phi(\mathbf{r})d\mathbf{r} \right]_{\infty} - \left[ \int \rho(\mathbf{r})\phi(\mathbf{r})d\mathbf{r} \right]_0 \right\}, \quad (2.10)$$

where  $\rho$  is the charge density caused by the free electron and  $\phi$  is the corresponding electrostatic potential, evaluated at high frequency ( $\infty$ ) or static (0) limits (Delerue and Lannoo, 2004).  $d_{FC}$  can be numerically estimated by first solving the Schrödinger equation for a particle in a finite box to obtain the charge density as illustrated in Fig. 2.5(c). This charge density gives rise to an electrostatic potential distribution (Fig. 2.5(d)), which is obtained as a solution of the Poisson equation, either using the high frequency or static dielectric constants. Despite the known problems of the effective mass approach, this procedure is expected to give a good approximation of the electron-phonon coupling strength as it involves a volume integral that is insensitive to the details of the wavefunction and the response of the ions to the local electric field is not affected by quantum confinement effects. The calculation is done in a realistic STM junction geometry to include the screening from the metallic tip and the substrate. The calculations was performed using the finite element method. Parameters used were: barrier outside of the QD  $V_0 = 4eV$ , effective mass  $m^* = 0.11$ ,  $\varepsilon_{\infty} = 6.1$  and  $\varepsilon_0 = 9.3$ . Ignoring the screening from the neighboring QDs, this gives an estimate for the coupling strengths of 0.42 (rod) and 0.36 (dot), in fair agreement with the experimental results shown in Fig. 2.5(a).

The effect of the orbital symmetry on the coupling strength is summarized in Fig. 2.5(e) for the  $S$  and  $P_x$  states for several nanorods with different aspect ratios. There is a significant difference in the coupling strength between the  $S$  and  $P_x$  states (average values  $S_{hr} = 0.53$  and  $0.42$ , respectively). We observe (both experimentally and theoretically) only a weak dependence of  $S_{hr}$  on the nanorod aspect ratio (Fig. 2.7). The widths of the distributions shown in Fig. 2.5(e) reflect significant variations in the coupling strengths. In principle, the e-ph coupling is an intrinsic effect. However, the extension of the electrostatic potential distribution outside the nanorod makes the coupling strength sensitive to the dielectric environment of the QD. As limiting cases, we consider theoretically an isolated QD and a QD embedded in a slab of dielectric (same  $\varepsilon_{\infty}$  and  $\varepsilon_0$  as CdSe) in the STM junction geometry. The calculated values for a 3.5 nm diameter nanorod with an aspect ratio of 2 are  $S_{hr} = 0.42$  (isolated) and  $0.71$  (slab) for the  $S$  state and  $S_{hr} = 0.29$  (isolated) and  $0.60$  (slab) for the  $P_x$  state. Thus, the variation in the dielectric environment of the QDs provides a reasonable explanation for the average and the spread of the experimentally observed values of the coupling strength.

Typically, due to the asymmetric junction geometry,  $\Gamma_{in} < \Gamma_{out}$  as the setpoint current is limited to  $< 1nA$  (higher currents cause instabilities in the double-barrier tunneling junction). However, in some cases, the QD is weakly coupled with the substrate, making it possible to reach  $\Gamma_{in} > \Gamma_{out}$ . In this case, the degeneracy of the levels is lifted due to interactions between the carriers accumulating in the QD. An example of this is shown in Fig. 2.8(a): as the setpoint current is increased, we observe a new resonance at a bias of ca. 1.2 V. This corresponds to the addition of a

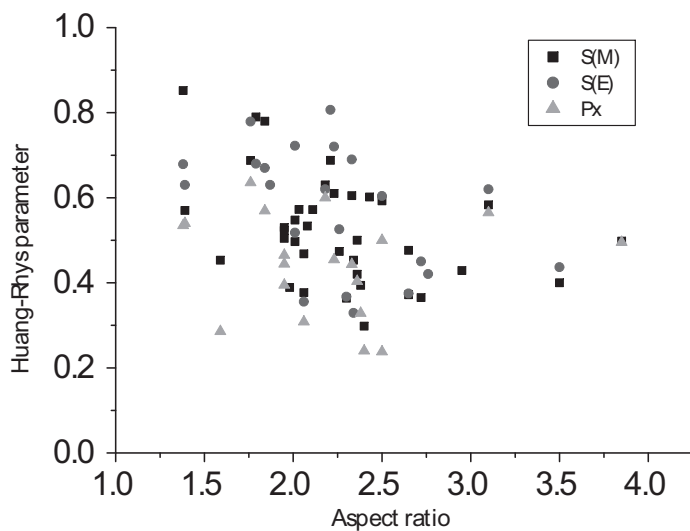


Figure 2.7: (Color online) Huang-Rhys parameter as a function of the aspect ratio of CdSe QDs we have measured. Filled squares: Huang-Rhys parameter of  $S$  state measured at the middle of the QD. Circles: Huang-Rhys parameter of  $S$  state measured at the end of these QDs. Triangles: Huang-Rhys parameter measured for  $P_x$  state, where  $x$  is the long axis of the nanorod.

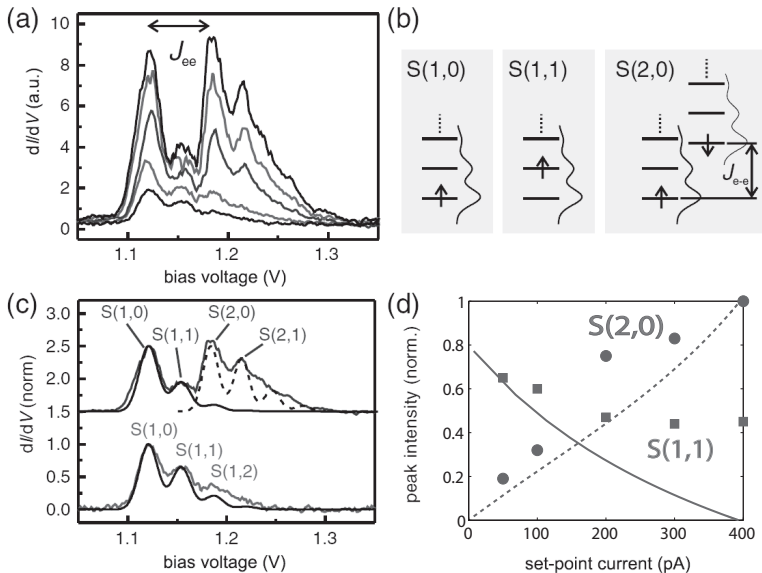


Figure 2.8: (Color online) Electron-phonon coupling under shell-filling conditions. (a) Evolution of the spectra from shell-tunneling to shell-filling when the setpoint is increased (50, 100, 200, 300, 400 pA). (b) Level occupations corresponding to the first 3 resonances. (c) Fitting of the spectra shows that the amplitude of the electron-phonon replica is enhanced for the second added electron. The labeling for the different resonances is indicated. (d) Evolution of the peak intensities with the setpoint current: for the first phonon replica ( $S(1,1)$ , squares), for the addition of second electron ( $S(2,0)$ , circles) along with the corresponding numerical fitting.

second electron into the  $S$  orbital of the QD and the spacing between the resonances (see Figs. 2.8(b) and 2.8(c) for the labeling of the resonances) is equal to the e-e repulsion ( $J_{e-e}$ ), 55 meV in the present case. The spectra acquired at the highest and lowest setpoints, normalized by the amplitude of the first resonance, are shown in Fig. 2.8(c). The relative amplitudes of the  $S(1,0)$  and  $S(2,0)$  resonances give information on the ratio of  $\Gamma_{in} = \Gamma_{out}$ ; in the limit of  $\Gamma_{in} \gg \Gamma_{out}$ , the amplitudes are equal as in the measured spectra at the highest setpoint currents.

In the shell-filling regime, the current is determined by  $\Gamma_{out}$ . We use a master equation approach to simulate the spectra (Delerue and Lannoo, 2004). We use  $\Gamma_{in1}, \Gamma_{in2}$  and  $\Gamma_{out1}, \Gamma_{out2}$  for the tunneling in and out rates of zero phonon states  $S(1,0)$  and  $S(2,0)$ . We choose  $\Gamma_{in1} = \Gamma_{in2}$  and  $\Gamma_{out1} = \Gamma_{out2}$  and we investigate how the relative intensities of both peaks vary with the setpoint current. By fitting the peak intensity data, we find that maximum tunneling out rate  $\Gamma_{out1}$  in this case is about  $10^9 \text{ s}^{-1}$ . The simulated evolution of the relative peak intensities as a function

of current is shown in Fig. 2.8(d), where we set Huang-Rhys parameter as 0.8. In the simulation, we assumed that the two electrons have the same electron-phonon coupling strength and fast internal relaxation.

## 2.4 Summary and outlook

In summary, our experiments provide quantitative orbital and charge-resolved information on the electron-phonon interaction in CdSe QDs. It is shown that Fröhlich coupling to the LO-phonon mode is the dominant mechanism. The dependence of the coupling strength on the QD shape and size, the symmetry of the electronic orbital, and the dielectric environment of the QD can be understood within the effective mass and continuum dielectric picture. Our results provide fundamental information required in understanding electron transport in QD devices and superlattices (Talapin and Murray, 2005; Houtepen *et al.*, 2008; Yu *et al.*, 2004) and the intraband relaxation of hot carriers in QDs (Klimov, 2007; Pandey and Guyot-Sionnest, 2008; Schaller *et al.*, 2006; Hendry *et al.*, 2006).

## 2.5 Acknowledgement

We thanks Rolf Koole for providing us the CdSe sample for study.

---

## Chapter 3

# Hole-Induced Electron Transport through PbSe/CdSe Core-Shell QDs

### 3.1 Introduction

Colloidal semiconductor quantum dots (QDs) are well-known for their tunable optoelectronic properties; for example, their emission color can be adjusted by changing the QD size due to quantum confinement (Murray *et al.*, 2000; Talapin *et al.*, 2010; de Mello Donegá *et al.*, 2005). Recent advances in the wet-chemical synthesis of QDs have further enhanced these possibilities by making it possible to create hetero-nanostructures, where two different semiconductors are incorporated into a single colloidal QD (Kim *et al.*, 2003; Balet *et al.*, 2004; Kudera *et al.*, 2005; Milliron *et al.*, 2004; Chin *et al.*, 2007; Klimov *et al.*, 2007). As the band offsets can be tuned through the choice of the materials and by quantum confinement, the optoelectronic properties of these materials can be engineered with a high level of control (Talapin *et al.*, 2010; Kim *et al.*, 2003; Balet *et al.*, 2004). In particular, the resulting systems can be classified according to their relative band alignment (see Fig. 3.1(a)). "Type I" is where both the electrons and holes are confined in the core and "type II" is where electrons and holes are separated (Talapin *et al.*, 2010; Kim *et al.*, 2003). Type II structures have recently attracted considerable interest as the formation of indirect excitons (separation of the electron-hole pair between the core and the shell) leads to significant increase in the exciton life-time with possible applications in e.g. solar cells and zero-threshold lasers (Klimov *et al.*, 2007; Gur *et al.*, 2005).

The hetero-nanostructures have been previously studied by optical spectroscopy focusing on the effects of band alignment on absorption and emission spectra and exciton recombination dynamics. On the other hand, hetero-nanocrystals may show novel charge transport phenomena related to the asymmetric transport pathways for

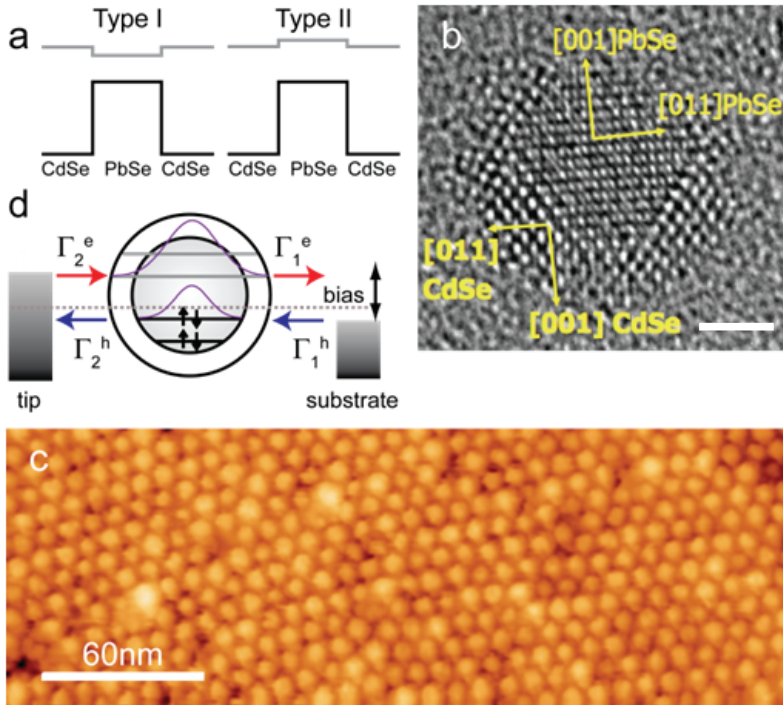


Figure 3.1: (a) Possible band-alignments of PbSe-CdSe core-shell QDs. (b) High-resolution TEM image of a PbSe-CdSe core-shell QD. Orientations of different crystal planes are indicated. Scale bar: 2 nm. (c) STM topography image of an array of PbSe-CdSe QDs on an HOPG substrate. (d) Schematic illustration of the transport processes in a double-barrier tunneling junction.

electrons and holes. This should have important consequences for optoelectronic devices that convert light into electrical current, or vice versa. The effects on charge transport due to the quantization of charge and the discrete energy levels of nanostructures are well-established (Averin *et al.*, 1991; Likharev, 1999; Sohn *et al.*, 1997; Delerue and Lannoo, 2004). For instance, addition of a single electron is possible only if the associated energy barrier is overcome, e.g. by applying a sufficient bias voltage between the source and the drain electrodes (Coulomb blockade). It should be realized, however, that in devices where both electrons and holes are present, new effects arise due to the electron-hole attraction and possibly, spin interactions (Delerue and Lannoo, 2004; Hanson *et al.*, 2007). Understanding these effects requires well-defined, quantitative experiments that allows one to separate the electron and hole currents, and measure the electron-hole interaction energy.

Under ambipolar charge transport conditions the electron-hole attraction will lower the energy barrier associated with electron tunneling. The offset between the hole-induced and bare electron tunneling channels provides a direct experimental access to the electron-hole interaction energy (*vide infra*). However, hole-induced electron tunneling is usually obscured by the fact that it is impossible to separate electron and hole currents. In addition, ambipolar transport typically requires high bias voltages (Jdira *et al.*, 2006; Liljeroth *et al.*, 2006a; Niquet *et al.*, 2002). Here, we demonstrate that these complications can be avoided by using PbSe-CdSe core-shell QDs (Fig. 3.1(b)), where the hole levels are localized in the PbSe core while the electron levels are delocalized over the entire hetero-nanostructure. This results from both the high effective mass of the hole in CdSe and the asymmetric band alignment between the conduction and valence bands of PbSe and CdSe. This type II (or quasi type II) band level alignment shown in Fig. 3.1(a) allows holes to be injected into the core at low bias voltage, which gives rise to hole-induced electron tunneling, while simultaneously the absolute magnitude of the hole current is strongly suppressed due to the higher barrier and higher effective mass of holes in CdSe. Our experiments demonstrate the simultaneous presence of two different tunneling channels: normal single-electron tunneling and hole-induced single-electron tunneling. The peak-spacing gives thus direct information on the electron-hole interaction energy.

## 3.2 Experimental

The charge transport through the core-shell QDs was investigated using LT-STM/STS, which have been extensively utilized in measuring the LDOS in single-electron charge transport experiments in QDs and QD assemblies (Banin *et al.*, 1999; Banin and Millo, 2003; Liljeroth *et al.*, 2006b; Overgaag *et al.*, 2008; Steiner *et al.*, 2008). Colloidal PbSe-CdSe core-shell QDs (overall diameter 6nm with a shell thickness of 1.5nm, Fig. 3.1(b)) were synthesized through a cation-exchange reaction (Pietryga *et al.*, 2008; Lambert *et al.*, 2009) and deposited on highly oriented pyrolytic graphite (HOPG) substrates as described in previous chapter. TEM measurements showed that the shell-thickness is not isotropic within a QD, i.e. there are regions with thicker and

thinner shells. STM experiments were carried out at  $T = 4.7$  K with cut PtIr tips. A large scale STM image is shown in Fig. 3.1(c). The QDs appear as bright protrusions (bias voltage: 2.5 V, setpoint current: 10 pA). The differential conductance was recorded using a lock-in amplifier (amplitude 3 mV rms. at a frequency of 300 Hz).

### 3.3 Results and discussions

The overall band alignment of the PbSe-CdSe core-shell QDs is such that the hole-levels are strongly confined to the PbSe core, whereas the electron levels are more delocalized over the entire QD (Fig. 3.1(a)). The tip-QD-substrate geometry forms a double-barrier tunneling junction, as shown in Fig. 3.1(d). It is characterized by the electron tunneling rates  $\Gamma_1^e$  and  $\Gamma_2^e$  and the hole tunneling rates  $\Gamma_1^h$  and  $\Gamma_2^h$ , where the indices 1 and 2 refer to the tunneling barriers as defined in Fig. 3.1(d). The ratio  $\Gamma_1^e/\Gamma_2^e$ , ( $\Gamma_1^h/\Gamma_2^h$ ) will determine the number of additional electrons (holes) in the QD. For example, in the limiting case  $\Gamma_1^e \gg \Gamma_2^e$ , that is, under shell-tunneling conditions for electrons, electrons tunnel through the QD one by one, and electron-electron interactions do not occur. In this case, the peaks in the tunneling spectrum at positive bias reflect the single-electron energy levels, provided that no holes are present.

A typical tunneling spectrum ( $dI/dV_b$  vs.  $V_b$ ) recorded on a PbSe-CdSe core-shell QD (top trace, 4 nm core, overall diameter 6 nm) is compared to representative spectra of pure PbSe and CdSe QDs (middle and bottom traces, respectively) in Fig. 3.2(a). The spectrum of the core-shell QD is very different from those measured on pure PbSe and CdSe QDs (Jdira *et al.*, 2006; Liljeroth *et al.*, 2005) suggesting a novel electron transport mechanism through these hetero-nanostructures. The most striking observation is that the spectrum of the heterostructure consists of a series of doublet peaks with constant intra-doublet spacing, absent in the spectra of pure CdSe or PbSe QDs. The inter-doublet spacing is not constant, suggesting a different physical origin from the intra-doublet spacing. We have observed these characteristic features for a large fraction ( $\sim 30\%$ ) of the core-shell QDs. It is likely that the position of the core in the tip-QD (core-shell)-substrate junction is similar for all these QDs. In Fig. 3.2(b), a histogram of the measured peak-spacings is given for 20 QDs. The intra-doublet spacing is strongly peaked around  $110 \pm 8$  meV, demonstrating that the spacing is essentially the same for all QDs. In contrast, the inter-doublet spacing is considerably larger than the intra-doublet spacing and is QD dependent. All the above strongly suggests that the doublets arise due to a charge transport mechanism that is specific to the PbSe-CdSe core-shell QDs.

To investigate the origin of these doublet-peaks, we performed simulations of the tunneling conductance spectra based on a master-equation approach, which is widely used in simulating electron and hole transport (Averin *et al.*, 1991; Likharev, 1999; Delerue and Lannoo, 2004; Niquet *et al.*, 2002). Due to the band alignment in the PbSe-CdSe core-shell QDs, both the height and width of the tunneling barriers are larger for holes than for electrons (hole states are localized in the core, see Fig.

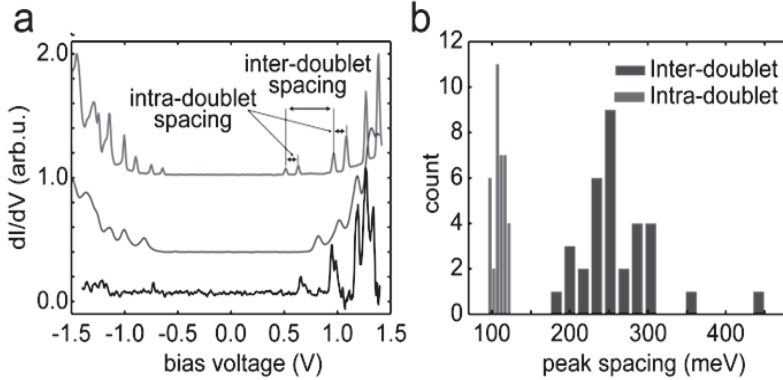


Figure 3.2: (a) Differential conductance spectra of a PbSe-CdSe core-shell QD (top), a 4.3 nm PbSe QD (middle), and a 6.1 nm CdSe QD (bottom). (b) Histogram of inter- and intradoublet peak spacing.

3.1(d)). Hence, the hole-tunneling rates are smaller than the electron-tunneling rates. Since the experiments are performed under shell-tunneling conditions, the current is limited by the electron-tunneling rate from tip to QD,  $\Gamma_2^e$ . This rate is set to  $10^8 \text{ s}^{-1}$ , as this gives tunneling currents comparable to the experimental setpoint currents. Both electron and hole transport, as well as electron-hole recombination rate (R) are considered. While we expect the electron tunneling to occur under shell-tunneling conditions, this may not hold for the holes. Due to the asymmetric position of the PbSe core in the QDs and the random deposition process, there is a distribution of different QD orientations in the arrays. The position of the core inside the QD strongly influences the widths of the tunneling barriers for holes, and therefore the hole-tunneling rates. Hence, a distribution in the  $\Gamma_2^h/\Gamma_1^h$  ratios, and therefore in the observed spectra can be expected. We will investigate this effect theoretically by varying the ratio of the hole-tunneling rates  $\Gamma_2^h/\Gamma_1^h$ , while keeping the absolute values smaller than the electron-tunneling rates. The electron-electron interaction energy,  $E_{e-e}$ , the position of the Fermi-level of the tip and substrate with respect to the QD energy levels,  $\varepsilon_F$ , as well as the fraction of the applied bias that drops in the tip - QD junction,  $\eta$ , are considered as parameters. The polarization energies for electrons and holes,  $E_{pol}^e$  and  $E_{pol}^h$ , are set to  $E_{e-e}/2$  (Delerue and Lannoo, 2004; Franceschetti *et al.*, 2000).

Based on our master equation simulations, reproducing the doublets observed experimentally requires that the Fermi levels of the tip and substrate are closer to the valence levels than to the conduction levels (at zero applied bias). In Fig. 3.3(a), the evolution of the simulated differential conductance spectra as a function of  $\Gamma_2^h$  ( $10^7$ ,  $10^6$ ,  $10^5$ ,  $10^4$ , and  $10^3 \text{ s}^{-1}$ ) is shown.  $\Gamma_1^h$  was fixed at  $10^5 \text{ s}^{-1}$ . The hole energy level positions are such that hole injection occurs at positive bias before electron injection.

Table 3.1: Parameter values used in the calculation of the differential conductance spectra shown in Fig. 3.3(d).

	$\Gamma_1^e(s^{-1})$	$\Gamma_2^e(s^{-1})$	$\Gamma_1^h(s^{-1})$	$\Gamma_2^h(s^{-1})$	$R(s^{-1})$
blue spectrum	$10^9$	$10^8$	$10^7$	$10^7$	$10^7$
red spectrum	$10^9$	$10^8$	$10^7$	$10^7$	0
black spectrum	$10^{12}$	$10^8$	$10^7$	$10^7$	0
green spectrum	$10^{12}$	$10^8$	$10^0$	$10^0$	0

Under the condition that  $\Gamma_2^h \gg \Gamma_1^h$  (top trace in Fig. 3.3(a)), all holes that tunnel into the QD at positive bias immediately tunnel out, leading to an average hole occupation of zero. In this regime the normal electron-tunneling resonance is observed. When  $\Gamma_2^h \ll \Gamma_1^h$  (bottom trace in Fig. 3.3(a)) electrons will always tunnel in the presence of a hole. In this situation, the non-zero hole occupation of the QD leads to an overall shift of the orbitals to lower energy (Fig. 3.2(c)), causing the electron-tunneling channels to open at lower applied bias.

In Fig. 3.3(b), the spectrum simulated with  $\Gamma_2^h/\Gamma_1^h = 1$  is shown, together with the bias dependence of the electron and hole occupations calculated with the same parameters. For this ratio of  $\Gamma_2^h/\Gamma_1^h$ , the average hole occupation is smaller than the maximum value and therefore both the hole-induced electron tunneling channel and the conventional tunneling process occur. In this regime, the spectrum consists of a series of doublet peaks, as observed experimentally. Considering the asymmetric position of the PbSe core in the core-shell geometry, a ratio of  $\Gamma_2^h/\Gamma_1^h = 1$  is realistic. The inset in Fig. 3.3(b) shows the relative contributions of electrons and holes to the total current. Since the hole-tunneling rates are much smaller than the electron-tunneling rates, the hole contribution to the total tunnel current is negligible, i.e. all resonances are due to electron tunneling.

The doublet features observed for the core-shell QDs appear in the simulations over a wide range of electron and hole tunneling rates. In Fig. 3.3(d), several simulated differential conductance spectra are shown. For all simulations, the same energy level structure of the QDs was used, as well as the same values of  $E_{e-e}$ ,  $\eta$ , and  $\varepsilon_F$ , i.e. only the values of the tunneling rates and the recombination rate were changed; the values are given in table 3.1. The doublet-peaks are clearly recognizable in all 4 spectra, demonstrating that the hole-tunneling rates can be varied over 7 orders of magnitude. In addition, including electron-hole recombination does not lead to any qualitative changes in the spectra, as long as the recombination rate is smaller than  $\Gamma_2^h$ . If the value becomes larger, the hole occupation of the QD decreases and the hole-induced tunneling resonance becomes less pronounced.

We demonstrate below that the observed resonances both at negative and positive bias can be reproduced within the hole-induced electron tunneling scheme. In Fig. 3.4 experimental spectra of two different QDs and the corresponding simulated spectra are shown. The experimental conductance spectra can be reproduced by the simulations. The master equation simulations allow us to assign specific transitions in the QD to the

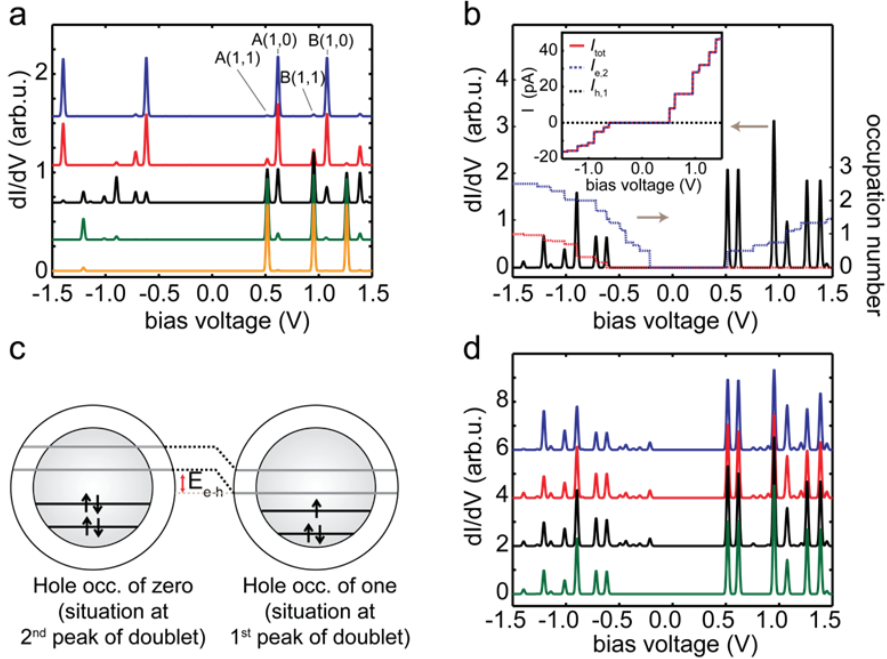


Figure 3.3: (a) Evolution of simulated differential conductance spectra as a function of  $\Gamma_2^h$  ( $10^7, 10^6, 10^5, 10^4$ , and  $10^3$   $s^{-1}$ , bottom to top).  $\Gamma_1^h$  was fixed at  $10^5$   $s^{-1}$ . The labels  $Z(x,y)$  refer to the conduction level, the number of holes and the number of electrons involved in the tunneling process, respectively. (b) Electron (red) and hole (blue) populations corresponding to  $\Gamma_2^h/\Gamma_1^h = 1$  (black spectrum, reproduced from Fig. 3(a)). The inset shows the relative contributions of electrons and holes to the total current. (c) Schematic of the influence of a hole on the electron levels. (d) Simulated differential conductance spectra, calculated with different values of the hole and electron tunneling rates. Parameter values given in Table 3.1.

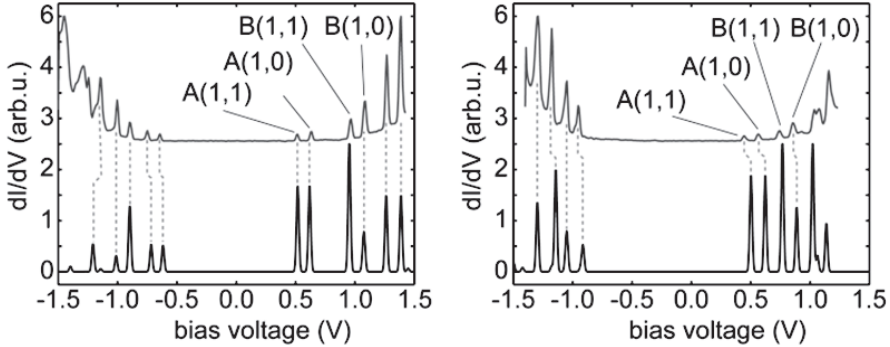


Figure 3.4: Comparison between simulated (bottom) and experimental (top) differential conductance spectra of two PbSe/CdSe core-shell QDs (left and right panels). The labels  $Z(x,y)$  refer to the first (A) and second (B) conduction levels, with the number of electrons and holes involved in the tunneling process indicated by  $x$  and  $y$ , respectively.

tunneling resonances (see Fig. 3.4). We did not include electron-hole recombination in these specific simulations due to the long exciton life-time in PbSe and type II QDs (Chin *et al.*, 2007; Allan and Delerue, 2004; An *et al.*, 2007). In addition, the peak intensities are influenced by factors that are not included in the model, such as the envelope wavefunction and the change in barrier height with increasing bias voltage. In addition, due to the small offset of the conduction band of the PbSe core and the CdSe shell, the electronic structure of the unoccupied levels is complicated by hybridization between PbSe and CdSe orbitals. Elucidating the finer details of the electronic structure, including the effect of the CdSe shell on the intervalley splitting in PbSe, will require numerical tight-binding or pseudopotential calculations. The resonances at negative bias are also reproduced by the theory and are due to electron tunneling in the presence of holes. However, the situation is more complicated than at positive bias. The same parameters can be used to reproduce the experimental conductance spectra of several different QDs.

Now, we will turn to the interpretation of the intra-doublet peak spacing. The reference energy is taken to be the energy of a neutral QD. The total energy of the QD in the presence of a hole is then given by:  $E_{QD,h} = \varepsilon_{1h} + E_{pol}^h$ , where  $\varepsilon_{1h}$  is the energy of the first hole level and  $E_{pol}^h$  is the polarization energy for a hole. When an electron is injected in the presence of a hole (first peak of the doublet), the total energy becomes:  $E_{QD,eh} = \varepsilon_{1h} + E_{pol}^h + \varepsilon_{1e} + E_{pol}^e - E_{e-h}$ , with  $\varepsilon_{1e}$  the energy of the first electron level and  $E_{e-h}$  the electron-hole interaction energy. Hence, the energy that is needed to inject an electron in the presence of a hole is:  $E_1 = \varepsilon_{1e} + E_{pol}^e - E_{e-h}$ . With similar arguments, the energy required to inject an electron in a neutral QD (second peak of the doublet) is found to be:  $E_2 = \varepsilon_{1e} + E_{pol}^e$ . Therefore, the energy difference,

$E_2 - E_1$ , i.e. the intra-doublet peak spacing, gives the electron-hole interaction energy. By taking into account the bias voltage distribution in the double-barrier tunneling junction ( $\eta = 0.7 - 0.8$ ) (Liljeroth *et al.*, 2006a; Overgaag *et al.*, 2008) we obtain a value of  $80 \pm 10$  meV for the electron-hole interaction energy in these PbSe-CdSe core-shell QDs. These measurements provide direct experimental information of the electron-hole interaction energy in QDs.

### 3.4 Summary

In summary, we have demonstrated a robust hole-induced electron tunneling mechanism in PbSe-CdSe core-shell QDs. By trapping a hole in the core of the QD, an additional channel for electron transport opens up at lower applied bias compared to a neutral QD. The difference in the bias voltage between the novel transport channel and the traditional tunneling pathway gives directly the electron-hole interaction energy for each electron level. Our results are important for electrically controlled single-photon emission. For instance, setting a bias between the peaks of the first doublet will lead to the emission of single photons. The emission rate is controlled by the rate of hole injection into the core of the core-shell QD.

### 3.5 Acknowledgement

We thank Dominika Grodzińska, Wiel Evers and Celso de Mello Donegá for providing the QDs and Christophe Delerue for discussions.



---

## Chapter 4

# Epitaxial graphene moiré pattern on Ir(111) measured by nc-AFM

### 4.1 Introduction

Graphene is a two-dimensional crystal formed by a single layer of carbon atoms and its lattice structure is formed by hexagonal honeycomb rings as illustrated in Fig. 4.1(a). The ground state electron configuration of a carbon atom is  $1s^2 2s^2 2p^2$ . These orbitals can be hybridized when the carbon atoms form molecules or crystals. In graphene every carbon atom has three covalent  $\sigma$  bonds, which are formed through hybridized  $sp^2$  orbitals, connected to nearest neighbor carbon atoms.  $sp^2$  orbital mixes one  $2s$  orbital with  $2p_x, 2p_y$  orbitals as shown in Fig. 4.2 (Pauling, 1931). The  $\sigma$  bond length in graphene is about  $1.42\text{\AA}$ .

Graphene has many unique properties. It is one of the strongest materials that has been measured and it has the largest surface area, very good thermal conductivity and it is impermeable to gases, even to helium. Free carriers in graphene have the highest intrinsic mobility and largest mean free path of any material at room temperature. Due to these unique properties, there are many proposed applications for graphene; for example, it is one of the most promising substitutes of silicon based electronics Geim and Novoselov (2007); Castro Neto *et al.* (2009); Sarma *et al.* (2011).

Wafer-sized graphene grown on *SiC* surface and transition metal surfaces by chemical vapor deposition (CVD) has been demonstrated recently (Emtsev *et al.*, 2009; Sutter *et al.*, 2008). Different growth methods such as CVD (Reina *et al.*, 2009) and chemical synthesis (Park and Ruoff, 2009) make large amount of high quality graphene available for industrial applications, such as making circuits or sensors. Those could also be integrated into silicon based electronics (Kim *et al.*, 2009) if the interaction between graphene and other materials is well understood.

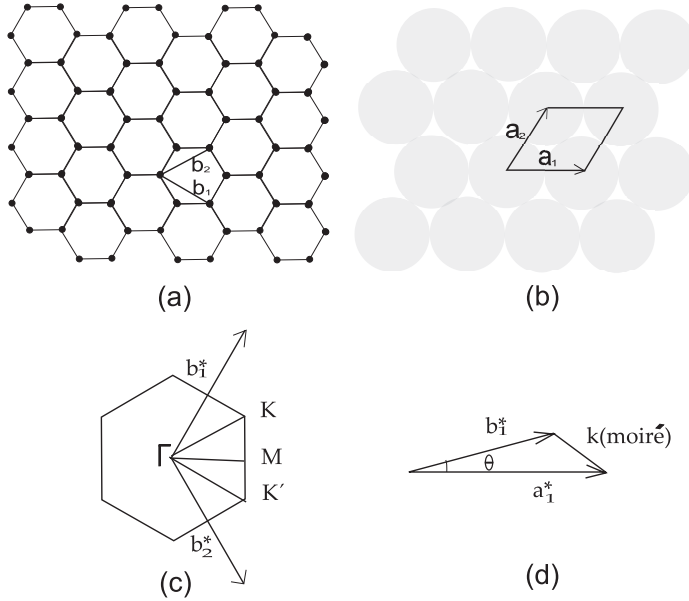


Figure 4.1: (a) The atomic lattice structure of graphene.  $b_1$  and  $b_2$  are the lattice constants of graphene.  $b_1 = b_2 = 2.46\text{\AA}$  (Ohta *et al.*, 2006). (b) The atomic lattice structure of Ir(111) surface.  $a_1$  and  $a_2$  are the lattice constants.  $a_1 = a_2 = 2.715\text{\AA}$ . (c) The Brillouin zone of graphene. The symmetry is the same with that of Ir(111). (d) Lattice mismatch and moiré pattern lattice in the  $k$  space.  $a_1^*$  is the reciprocal lattice constant of Ir(111) and  $b_1^*$  is the reciprocal lattice constant of graphene.  $k(\text{moiré})$  is that of the moiré pattern.

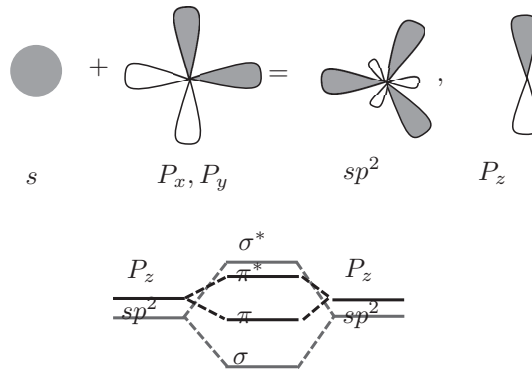


Figure 4.2:  $sp^2$  hybridization of carbon atom in graphene.

The present study focuses on the interactions between graphene and transition metal surfaces. The different metal surfaces can be coarsely classified based on how strongly the graphene layer interacts with the underlying metal substrate (Preobrajenski *et al.*, 2008). For example, Ir(111) and Pt(111) surfaces interact weakly with the graphene layer and consequently, graphene still exhibits linear Dirac-like dispersion characteristic of isolated graphene (Preobrajenski *et al.*, 2008; Pletikosić *et al.*, 2009; Sutter *et al.*, 2009b). On the other hand, on Ru(0001) and Ni(111) surfaces, the graphene band structure is strongly modified (Preobrajenski *et al.*, 2008; Sutter *et al.*, 2009a). While the CVD growth occurs epitaxially, the lattice mismatch between graphene and the metal substrate (see Fig. 4.1(b)) gives rise to a moiré pattern that is observed on most metal surfaces (notably Ir(111) (N'Diaye *et al.*, 2006, 2008; Loginova *et al.*, 2009; Coraux *et al.*, 2009), Rh(111) (Wang *et al.*, 2010), Ru(0001) (Vázquez de Parga *et al.*, 2008; Martoccia *et al.*, 2008; Moritz *et al.*, 2010), and Cu(111) (Gao *et al.*, 2010)).

This moiré pattern can be readily observed by STM (N'Diaye *et al.*, 2006; Vázquez de Parga *et al.*, 2008; Gao *et al.*, 2010). However, STM images do not directly probe the topography of the surface; instead, the STM tip traces constant integrated LDOS surfaces at energies close to the Fermi level (Giessibl, 2003; Hofer *et al.*, 2003). This causes the contrast and apparent corrugation of the graphene moiré on Ir(111) to depend on the STM imaging conditions (N'Diaye *et al.*, 2006, 2008). It is not a priori clear which STM images correspond to the actual topography of the surface.

We use simultaneous low-temperature AFM and STM measurements on epitaxial graphene monolayers on Ir(111) to understand the contributions of actual topography, charge transfer giving rise to local variations in the tunneling barrier height and contact potential difference, and variations of the LDOS on the observed moiré pattern.

## 4.2 Experimental

We investigated epitaxial monolayer graphene grown on Ir(111) single surface by chemical vapor deposition (CVD) method (Coraux *et al.*, 2009). Iridium crystal was prepared by several sputtering-annealing cycles. The (111) surface was first cleaned by  $3kV$   $Ar^+$ -ion sputtering at room temperature followed by flashing to  $1400K$  and annealing at  $1200K$ . After the last annealing cycle, the sample was first annealed for 3 min at  $800K$  in  $1 \cdot 10^{-7}$  mbar  $O_2$ , then flashed to  $1400K$  before starting the CVD process. In order to ensure the formation of a full graphene monolayer, the sample was exposed to  $5 \cdot 10^{-7}$  mbar ethylene at  $1250K$  for 100 s. The sample was then transferred *ex situ* to the LT-STM/AFM system. Before transferring to the SPM chamber, the sample was annealed to  $800K$ . All SPM experiments (LT-SPM with qPlus sensor) were carried out under UHV and LHe temperature ( $4.7K$ ). The instrument is capable of simultaneous frequency modulation (FM) noncontact tuning fork AFM (Giessibl, 2003) and STM measurements. For nc-AFM experiments, the tip cantilever oscillation frequency was about  $24kHz$  and had a quality factor of 18800.

The tip oscillation amplitude was  $5\text{\AA}$ . Tip was made of PtIr wire. Voltage was applied to the tip and defined as sample vs. tip.  $dI/dV_b$  and  $dI/dz$  signals were recorded with a lock-in amplifier by applying a small sinusoidal variation to the bias voltage or the z-piezo position, respectively.

### 4.3 Results and discussion

Fig. 4.3(a) shows a constant current STM topography image of a graphene monolayer on Ir(111). In addition to the atomically resolved hexagonal structure, a moiré pattern with a period of about  $2.5\text{ nm}$  is clearly visible. It has been shown by N'Diaye *et al.* (2008) that this superstructure preferentially orients along the atomic rows of graphene, which is also the case in Fig. 4.3. The moiré unit cell is indicated with solid lines and the three inequivalent areas (with respect to the registry of Ir(111) lattice) are indicated by A, B and C. It has been previously suggested that they correspond to areas where the graphene honeycomb is centered on the underlying iridium atoms (atop, A), or the fcc (B) or hcp (C) threefold hollow sites (N'Diaye *et al.*, 2006, 2008). We also observed that the apparent height corrugation depends on the tip conditions and bias voltage, in agreement with earlier results of N'Diaye *et al.* (2008). STM images at a higher bias ( $> 0.5V$ , Fig. 4.3(b)) exhibit inverted moiré contrast compared to the low-bias images.

In addition to standard STM imaging, we can get further information on the local electronic properties by mapping out the LDOS ( $\propto dI_t/dV_b$ ) and the tunneling decay constant  $\kappa$  ( $\propto dI_t/dz$ ) signals in the constant-current mode. These quantities vary over the moiré pattern, as shown in Fig. 4.3(c). Both LDOS and  $\kappa$  are lower at region A of the moiré.

The apparent peak to peak (p-p) corrugation of the moiré pattern in Fig.4.3(a) is  $45\text{ pm}$ . As the STM image is clearly influenced by electronic effects, we carried out nc-AFM experiments to probe the surface topography of graphene monolayer on Ir(111). Fig. 4.3(d) shows a typical nc-AFM topography image. In addition to the contrast on the atomic scale, we observe a moiré pattern with similar contrast as in STM and the apparent p-p corrugation is about  $30\text{ pm}$ . Careful inspection of Fig. 4.3(d) shows a variation in the atomic scale contrast. On the bright area of the moiré pattern, the carbon atoms are imaged as depressions, inline with earlier atomically resolved images of carbon nanotubes (Ashino *et al.*, 2004). The contrast changes on the dark areas, indicating that the tip-graphene distance is different on the different regions of the moiré pattern.

The simultaneously measured tunneling current during the AFM imaging is shown in Fig. 4.3(e). It again shows both atomic and morié contrast, where low current region is aligned with the depressions in the topography image. We found the same qualitative moiré contrast with different tips and on different locations of the sample.

The tip-sample interaction causes a frequency shift  $\Delta f$  of the cantilever. At small oscillation amplitudes, the measured detuning is directly proportional to the

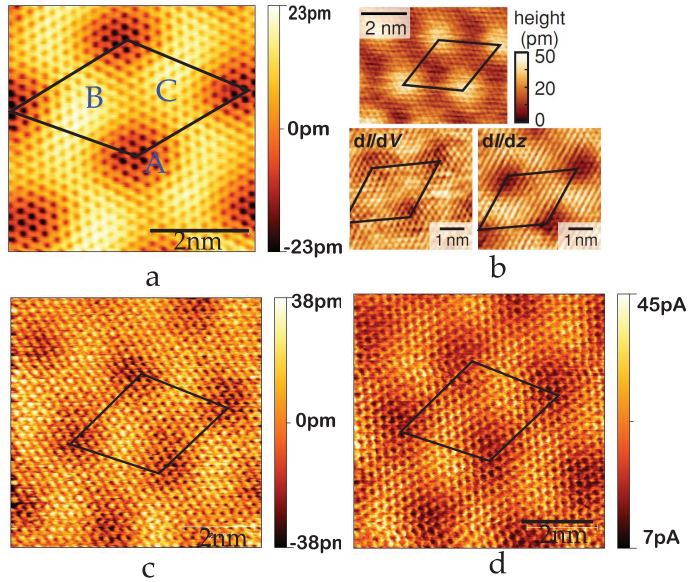


Figure 4.3: (a) Constant-current STM topography image of epitaxial graphene on Ir(111) taken under bias voltage  $V_b = 0.3V$  and set-point current  $I_t = 0.3nA$ . The diamond structure is the unit cell of the moiré pattern and the three inequivalent areas within it are denoted by A, B and C. (b) High-bias STM image taken at  $0.45V/1nA$  showing the inverted moiré pattern. (c) Constant-current  $dI/dV_b$  and  $dI/dz$  maps recorded at a bias of  $0.05V$ . (d) Constant frequency shift nc-AFM image taken with  $V_b = 0.15V$  and  $\Delta f = -45Hz$ . (e) Average current over the tip oscillation cycle measured simultaneously under AFM feedback.

interaction force gradient.

$$\Delta f = -\frac{f_0}{2k} \frac{\partial F_{ts}}{\partial z}, \quad (4.1)$$

where  $F_{ts}$  is the total interaction force between tip and sample,  $k$  is the spring constant of the cantilever and  $f_0$  is the tip oscillation frequency (Giessibl, 2003). Different forces contribute to  $F_{ts}$  and the most relevant ones in our experiment are quantum mechanical forces between the tip apex and the surface (Pauli repulsion, chemical bonding); vdW interaction between the tip and graphene and tip and the iridium substrate; and electrostatic forces (Giessibl, 2003; Hofer *et al.*, 2003; Gross *et al.*, 2009). AFM topography might also be affected by chemical inhomogeneity of the surface (different regions of the graphene moiré are known have different chemical reactivities (N'Diaye *et al.*, 2006; Wang *et al.*, 2010; Vázquez de Parga *et al.*, 2008)). However, we have observed the same qualitative moiré contrast with different tip terminations, consistent with the expected weak interaction between graphene and the Ir(111) surface.

Experimental results based on photoelectron spectroscopy (ARPES and XPS) and *ab initio* calculations show that the interaction between graphene and iridium is weak (N'Diaye *et al.*, 2006; Preobrajenski *et al.*, 2008; Pletikosić *et al.*, 2009; Feibelman, 2008). Theoretical calculations give an average graphene-Ir(111) distance of 3.9Å (GGA-DFT) (N'Diaye *et al.*, 2006) or 3.42Å (LDA-DFT) (Feibelman, 2008). It is well-known that GGA underestimates and LDA overestimates binding in systems where vdW interactions are important. Recent DFT calculations using vdW-corrected functionals have found binding distances of 3.6 – 3.7Å for graphene on weakly interacting metals (e.g. Pt) (Vanin *et al.*, 2010). Despite the large binding distance, it is important to realize that the vdW forces between the tip and the sample are sufficiently long range to include contributions from the iridium substrate. In the attractive regime, the background vdW from the Ir substrate results in increased attraction in the area A of the moiré, which causes the AFM feedback to increase the tip-sample distance in order to keep  $\Delta f$  constant. Hence, the AFM corrugation underestimates the real topographic corrugation of the graphene moiré as illustrated in Fig. 4.4(a).

We model this effect within the small amplitude approximation (detuning proportional to force gradient). This approximation is valid if the force gradient is roughly constant throughout the oscillation cycle of the tip. We use relatively small oscillation amplitudes and consider here only the vdW interactions that are relevant for the AFM observation of the moiré pattern on an otherwise chemically homogeneous surface. The chemical interactions between the tip apex and the surface act at very short distances, which are much smaller than the tip oscillation amplitude. The long-range electrostatic force remains almost constant over the oscillation cycle assuming that neither the tip nor the surface is charged. Consequently, these forces make only a minor contribution to the observed AFM response.

The tip is modeled as a paraboloid  $z = x^2/(2R)$ , where  $R$  is the tip radius. The total vdW force felt by the tip can be calculated by integrating the vdW potential

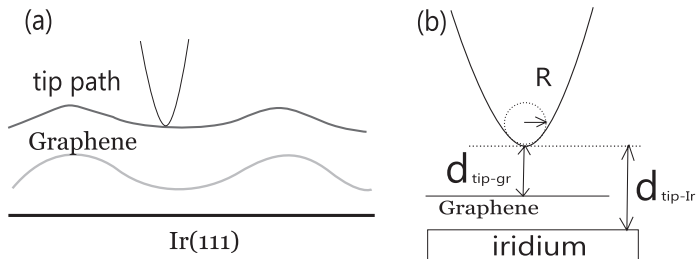


Figure 4.4: (Color online) (a) Schematic view of AFM scanning line profile and real graphene corrugation. (b) Variables in Eq. 4.3.

(where  $\epsilon$  is an energy parameter)

$$w_{vdW} = -4\epsilon\left(\frac{\sigma}{r}\right)^6 \quad (4.2)$$

over the tip and Ir bulk, and the tip and the two-dimensional graphene layer (Hofer *et al.*, 2003). We assume that the vdW interaction between the tip and Ir bulk is not screened by the graphene layer. Hence, we obtain an upper limit of the background vdW interaction. The derivative of the total force is then proportional to the detuning  $\Delta f$  of the tip

$$\Delta f = -\frac{f_0 R}{2k} \left( \frac{\sqrt{A_{tip} A_{Ir}}}{3d_{tip-Ir}^3} + \frac{\sqrt{A_{tip} A_{HOPG}}}{d_{tip-gr}^4 l_{HOPG}} \right), \quad (4.3)$$

where  $A = 4\pi^2 \epsilon_i \rho_i^2 \sigma_i^6$  is the Hamaker constant and  $d_{tip-Ir}$  and  $d_{tip-gr}$  are the tip-Ir and the tip-graphene distances corresponding to the midpoint of the tip oscillation cycle. In the case of a two-dimensional layer, the vdW force depends on the surface atom density rather than the volume density. We take this into account by using the HOPG Hamaker constant  $A_{HOPG}$  and the layer density  $l_{HOPG}$ .

In Eq. 4.3, the first term of the detuning caused by the tip-Ir vdW force and the second term is the tip-graphene vdW force. The relation of these terms is illustrated in Fig. 4.5(a), where we plot them and the total  $\Delta f$  as a function of the tip-graphene distance. The contribution from the Ir substrate increases and even becomes dominant term at large distances.

We have solved the tip-graphene distance  $d_{tip-gr}$  from Eq. 4.3 numerically as a function of the graphene-Ir distance ( $d_{tip-Ir} - d_{tip-gr}$ ).  $d_{tip-gr}$  changes almost linearly over a reasonable range of graphene-Ir distances. The slope  $s$  of this curve represents the underestimation of the moiré corrugation due to the background vdW forces from the Ir substrate. So the real corrugation of the moiré is given by  $a_{real} = (1 - s)a_{AFM}$ . The Hamaker constants have a fairly small effect on the slope, whereas  $R$  and  $\Delta f$  have a quite significant effect. This is illustrated in Fig. 4.5(c), where we plot the average slope in the range of  $d_{gr-Ir}$  between 3 and 4 Å. This can be understood by the fact that  $\Delta f$  and  $R$  determine the absolute tip-graphene distance, which governs the

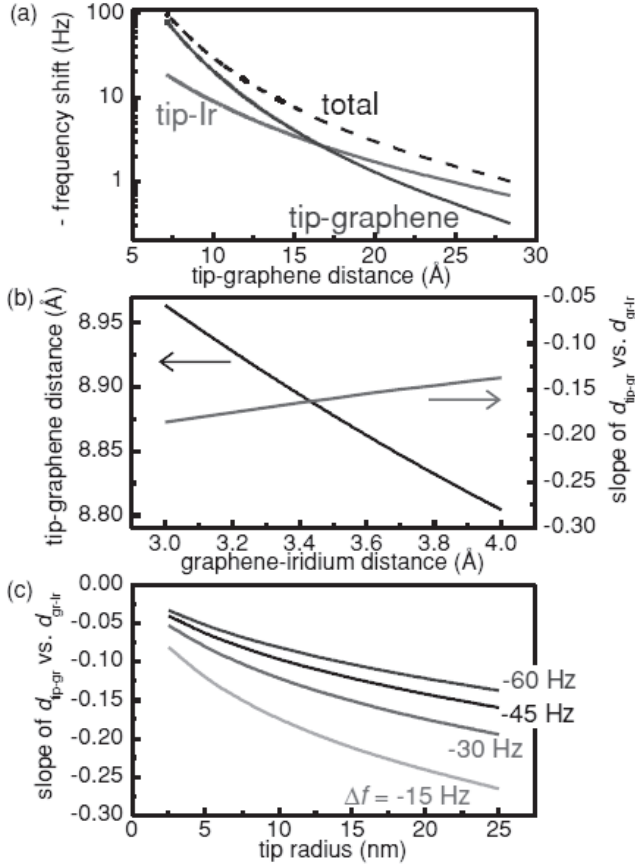


Figure 4.5: (Color online) Theoretical modeling of the vdW forces in the AFM tip-graphene-Ir substrate system. (a) The contributions of graphene and iridium substrate to the total frequency shift  $\Delta f$ . (b) Tip-graphene distance as a function of graphene-Ir distance calculated with  $\Delta f = -45 Hz$ . The corresponding slope is plotted on the right  $y$  axis. (c) Slope  $s$  of the  $d_{tip-Ir}$  vs.  $d_{tip-gr}$  curve for different tip radii and different  $\Delta f$ . Panels (a) and (b) are calculated with  $R = 10 nm$ .  $A_{HOPG} = 3.42 \times 10^{-19} J$ ,  $A_{tip} = A_{Ir} = 4 \times 10^{-19} J$  (Visser, 1972; Israelachvili, 1992) and  $l_{HOPG} = 1/335.4 pm$  were used in all the calculations.

proportion of the vdW force from the bulk Ir with respect to the total force. While our estimation of  $d_{tip-gr}$  depends on  $R$ , which is difficult to estimate independently, we can also estimate  $d_{tip-gr}$  based on the simultaneously recorded tunneling current (Giessibl, 2003). Taking into account the tip oscillation and using a measured value of the tunneling decay constant  $0.55\text{\AA}^{-1}$ , we can extrapolate the distance to point contact. This gives an average tip-graphene distance of  $7.2\text{\AA}$  in Fig. 4.3.

The data shown in Fig. 4.5(c) shows that even though the background vdW from the Ir bulk affects the apparent AFM corrugation, the effect is rather small. The correction factor is 10% – 20% for reasonable tip radii and at sufficiently negative frequency shift  $\Delta f$ , which yields  $35 \pm 10\text{pm}$  as our estimation of the actual moiré corrugation. Here we did not take into account the actual shape of moiré pattern. The model only corrects the measured corrugation by the background vdW from the Ir bulk.

The increase in the tip-graphene distance caused by the increased background vdW interaction between the tip and the Ir substrate in the area  $A$  of the moiré reduces the tunneling current as seen in Fig. 4.3. However, if we use the estimated changes in  $d_{tip-gr}$ , we only get a current variation of about 10%. On the other hand, the experimentally measured variation is much larger, about a factor of 2. Apart from the  $d_{tip-gr}$ , the tunneling current is influenced by the LDOS and the decay constant  $\kappa$ . These quantities have opposite effects on the tunneling current: the larger the LDOS, the larger the tunneling current. On the other hand, the larger the decay constant, the smaller the tunneling current as it is proportional to  $\exp(-2\kappa d_{tip-gr})$ . Then our results imply that at small bias, the reduced LDOS in the region A of the moiré is mostly responsible for the reduced tunneling current in the simultaneously measured tunneling current images under AFM feedback.

We can get more detailed information on the interaction between graphene and the Ir(111) substrate from STS experiments. Two typical conductance spectra are shown in Fig. 4.6(a), which were taken at different positions with respect to the moiré pattern. These spectra did not exhibit an electron-phonon gap, as suggested by Zhang *et al.* (2008). In the work of Zhang *et al.* (2008), the graphene was deposited on an insulating substrate and hence, our experiments cannot be directly compared. The conductance spectra are slightly different on different locations with respect to the moiré pattern. On top of the moiré pattern (regions B, C), spectrum (blue) shows deeper slope at negative bias side than that (red) taken at the bottom of the moiré pattern (region A). This indicates that the LDOS of the graphene sheet is modified due to the interaction with the Ir substrate. On the top of the moiré, distance between graphene and iridium is larger than that on the bottom of the moiré pattern. The interaction in the region A should be stronger, which decreases the LDOS of graphene (about 5%) (see Fig. 4.6(b)).

The variable graphene-iridium interaction can also be seen in the  $dI/dz$  map recorded by adding a small external  $z$  direction oscillation to the STM tip (Fig 4.3(c)). From the  $dI_t/dz$  map and the tunneling current  $I_t$  data  $\kappa$  can then be calculated. Fig. 4.7 shows the calculated  $\kappa$  of graphene from  $dI_t/dz$  map and the simultaneously measured topography image at a small voltage bias (10mV) under constant-current

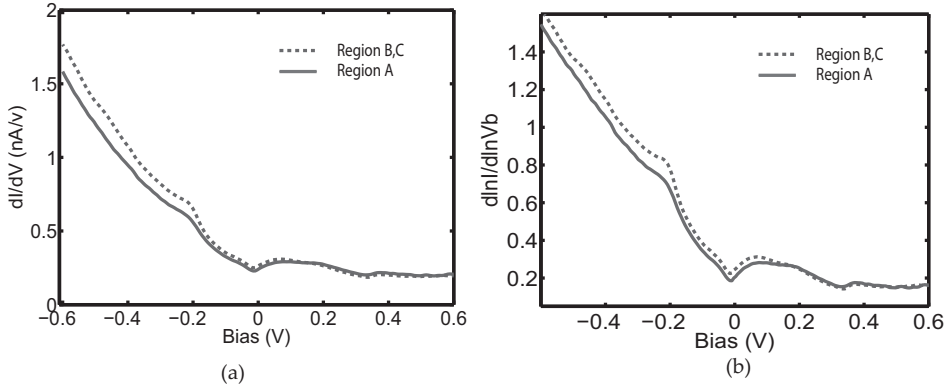


Figure 4.6: (Color online) (a) Conductance spectra on different positions of graphene with respect to the moiré pattern with the same metallic tip. Region A, B and C are denoted in Fig. 4.3(a). (b) The corresponding  $d \ln I / d \ln V_b$  spectra.

mode. In the topography image (b) the positions of carbon atoms are clearly resolved. From the map (a) we can observe that  $\kappa$  varies by 20% with respect to different positions of the moiré pattern. The average value of  $\kappa$  on top of the carbon atom is about  $0.6 \text{ \AA}^{-1}$ . In region A of the moiré pattern,  $\kappa$  is around  $0.55 \text{ \AA}^{-1}$ , while in regions B and C where  $\kappa$  is about  $0.65 \text{ \AA}^{-1}$ .

## 4.4 Conclusions

In summary, we achieved atomic resolution imaging on graphene on iridium (111) surface with both low temperature nc-AFM and STM measurements. While STM topography is dominated by electronic effects, nc-AFM gives qualitatively correct image of the surface topography. A more quantitative estimation of the moiré corrugation based on the AFM images requires considering the background tip-Ir vdW interaction. Taking this effect into account, we find that the p-p ‘geometric’ corrugation of the epitaxial graphene on Ir(111) is  $35 \pm 10 \text{ pm}$ .

In addition, we measured conductance spectra on different positions with respect to the moiré pattern. We find that the inverse decay length  $\kappa$  depends on both the moiré pattern and the exact atomic site. At small bias, inverse decay length varies about 20% with respect to the different positions on the moiré pattern.

## 4.5 Acknowledgement

We thank Sami Paavilainen for discussions.

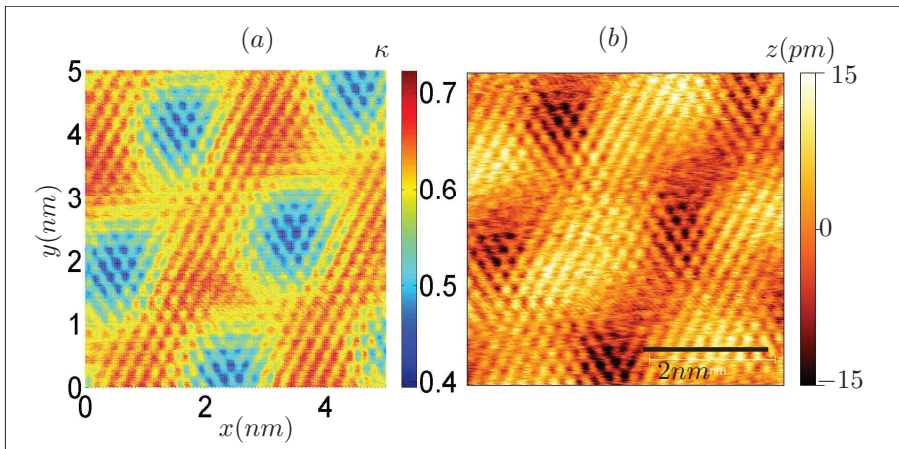


Figure 4.7: (a) Inverse decay length  $\kappa$  ( $\text{\AA}^{-1}$ ) of graphene varies respect to moiré pattern calculated from  $dI/dz$  mapping with constant current  $500\text{pA}$  as feedback.  $dI/dz$  mapping were taken with bias  $10\text{mV}$ . Tip oscillation frequency is  $1700\text{Hz}$ . (b) The STM topography image measured simultaneously with  $dI/dz$  mapping used to calculated the inverse decay length in (a).



---

## Chapter 5

# Confined electronic states in graphene nanoflakes on Ir(111) probed with nc-AFM

The properties of graphene can be altered by the interaction with the substrate as we discussed in the previous chapter. In addition, its electronic properties can be tuned by quantum confinement in nanometer-scale graphene nanoflakes, where both the size and the crystallographic termination of the flake edges can be important. Despite the potential of graphene nanostructures in electronic applications (Han *et al.*, 2007; Rycerz *et al.*, 2007; Ponomarenko *et al.*, 2008; Jiao *et al.*, 2009; Kosynkin *et al.*, 2009; Ritter and Lyding, 2009; Cai *et al.*, 2010; Sprinkle *et al.*, 2010), the study of quantum confined electronic states in atomically well-defined graphene nanostructures remains an experimental challenge. Basic questions, such as the relation between the atomic configuration of graphene nanostructures and the spatial distribution and energy of their electronic states have not been experimentally addressed. In this chapter, we explore the size- and shape-dependent LDOS by low-temperature STM and STS experiments on graphene nanoflakes<sup>1</sup> with well-defined atomic structures grown by CVD on an Ir(111) substrate.

### 5.1 Electronic structure of graphene

The electronic properties of graphene have been extensively reviewed; see, for example the articles by Geim and Novoselov (2007); Castro Neto *et al.* (2009); Sarma *et al.* (2011).

In graphene, every carbon atom has three nearest neighbor carbon atoms and

---

<sup>1</sup>In the following part of this chapter, graphene nanoflakes are also called as graphene quantum dots (g-QDs).

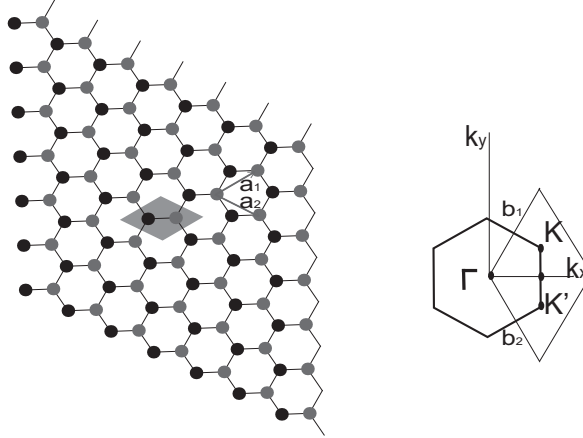


Figure 5.1: (Color online) Illustration of the graphene lattice structure and its first Brillouin zone. Left: The lattice structure of graphene and its unit cell is shown as the gray area. The two points inside the unit cell illustrate the two inequivalent atoms.  $\vec{a}_1$ ,  $\vec{a}_2$  are the two unit vectors. Right: The first Brillouin zone of graphene.  $K$  and  $K'$  are the Dirac points.

the unit cell has two carbon atoms. The lattice structure of graphene and its first Brillouin zone are shown in Fig. 5.1. The primitive translational vector length is  $2.46\text{\AA}$ ,  $\sqrt{3}$  times of the  $\sigma$  bond length. The lattice vectors can be written as  $\vec{a}_1 = a(\frac{\sqrt{3}}{2}, \frac{1}{2})$  and  $\vec{a}_2 = a(\frac{\sqrt{3}}{2}, -\frac{1}{2})$ . In the reciprocal space, we have  $\vec{b}_1 = \frac{2\pi}{a}(\frac{1}{\sqrt{3}}, 1)$  and  $\vec{b}_2 = \frac{2\pi}{a}(\frac{1}{\sqrt{3}}, -1)$ . The coordinates of the  $\vec{K}$  and  $\vec{K}'$  points in the Brillouin zone are  $\vec{K} = \frac{2\pi}{a}(\frac{1}{\sqrt{3}}, \frac{1}{3})$  and  $\vec{K}' = \frac{2\pi}{a}(\frac{1}{\sqrt{3}}, -\frac{1}{3})$ .

In graphene,  $2s$  and  $2p$  orbitals of the carbon atom are hybridized and form  $sp^2$  orbitals. Electrons in  $sp^2$  orbital form  $\sigma$  bonds between the nearest-neighbor carbon atoms. There is one electron left for every carbon atom in its  $2p_z$  orbital. These electrons form  $\pi$  bonds between neighboring carbon atoms and the  $\pi$  band is half filled.

The band structure of graphene was calculated sixty years ago with the tight-binding method (Wallace, 1947)<sup>2</sup>, much earlier than monolayer graphene was isolated and characterized experimentally by Novoselov *et al.* (2004). The calculated  $\pi$  band structure using nearest neighbor tight-binding model is shown in Fig. 5.2. It has no band gap. Since the  $\pi$  band is half-filled, the Fermi level of graphene locates at the middle of the  $\pi$  band. It was found that in the  $\pi$  band close to the  $\vec{K}$  and  $\vec{K}'$

<sup>2</sup>At that time, people were interested in the electronic structure of graphite, which can be considered as a graphene multilayer with an ordered stacking.

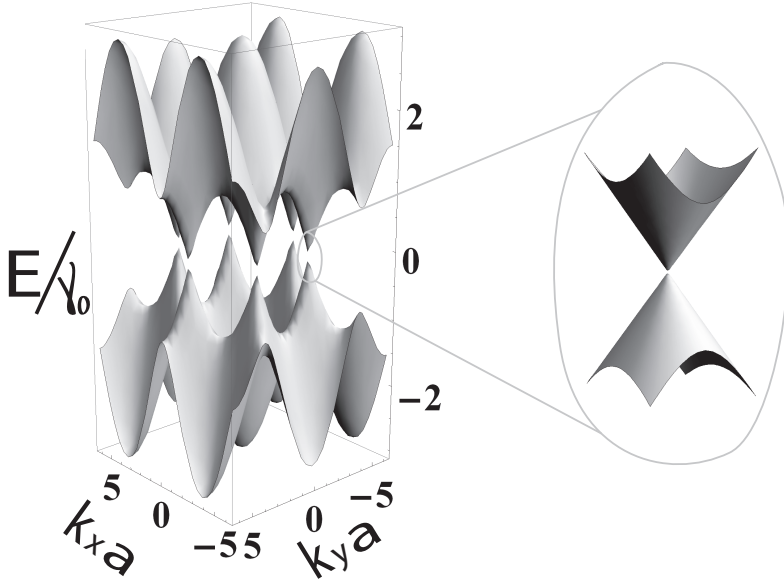


Figure 5.2: The  $\pi$  band structure of graphene calculated with the nearest-neighbor tight-binding model, where  $\gamma_0$  is the nearest-neighbor hopping energy and  $a$  is the unit vector length. (The calculation can be found in the Appendix.)

points of the Brillouin zone, (when  $|\vec{k} - \vec{K}|a = |\vec{k}|a \ll 1$ ), electron energy has a linear dependence on the relative momentum with respect to  $\vec{K}$  and  $\vec{K}'$ . The dispersion relation can then be written as (Wallace, 1947)

$$E_{\pm}(\vec{k}) = \pm \hbar v_F |\vec{k}|, \quad (5.1)$$

where  $v_F$  is the Fermi velocity  $v_F = \sqrt{3}\gamma_0 a/2 \simeq 10^6 m/s$  and  $\gamma_0$  is the nearest-neighbor hopping energy ( $\simeq 3eV$ )<sup>3</sup>.

The linear dependence of the electron energy on the momentum close to the Dirac points makes graphene different from other semiconductor materials which have the dispersion relation  $E(\vec{k}) = (\hbar\vec{k})^2/2m^*$  and  $m^*$  is the effective mass of the electron. The dispersion relation resembles that of massless fermions in the relativistic case. This results in many interesting quantum transport phenomena in graphene, such as Klein tunneling (Beenakker, 2008).

The linear dispersion relation of Eq. (5.1) means that low energy electron excitations in graphene have zero effective mass. The transport properties of those low

<sup>3</sup>It has been shown recently by Elias *et al.* (2011) that the linear dependence varies with the carrier concentration due to the electron-electron interaction effect.

energy carriers can be described by the massless Dirac equation (McClure, 1956).

$$-i\hbar v_F \begin{pmatrix} 0 & \partial_x - i\partial_y \\ \partial_x + i\partial_y & 0 \end{pmatrix} \begin{pmatrix} \Psi_A \\ \Psi_B \end{pmatrix} = E \begin{pmatrix} \Psi_A \\ \Psi_B \end{pmatrix}, \quad (5.2)$$

where the two spinor components  $\Psi_A, \Psi_B$  are the amplitudes  $\Psi_A(\mathbf{r})e^{i\mathbf{K}\cdot\mathbf{r}}, \Psi_B(\mathbf{r})e^{i\mathbf{K}\cdot\mathbf{r}}$  of the wavefunction of the electron in the two sublattices  $A$  and  $B$  (as illustrated in Fig. 5.1 by the black and red dots). Since Eq. (5.2) is similar to the equation describing the electron spins, this property of electrons in graphene is called pseudospin, which distinguishes the electrons belonging to the different sublattice of graphene. By using the Pauli matrices  $\sigma = (\sigma_x, \sigma_y, \sigma_z)$  and the momentum vector  $\mathbf{p} = -i\hbar(\partial_x, \partial_y)$  the previous equation can be written as

$$v_F \mathbf{p} \cdot \sigma \psi = E \psi, \quad (5.3)$$

where  $\psi = (\Psi_A, \Psi_B)$ .

Equation (5.3) only describes the states in the valley centered at  $\vec{K}$  with wave vector  $\vec{k}$ . At the opposite valley centered at  $-\vec{K}$ , there are states with amplitudes  $\Psi'_A(\vec{r})e^{-i\vec{K}\cdot\vec{r}}, \Psi'_B(\vec{r})e^{-i\vec{K}\cdot\vec{r}}$  on  $A, B$  sublattices (Beenakker, 2008). Those two components satisfy the same Dirac equation but with  $p_x = -p_x$ . By defining a spinor  $\Psi = (\Psi_A, \Psi_B, -\Psi'_A, \Psi'_B)$ , the four-dimensional equation turns into

$$\begin{pmatrix} v_F \mathbf{p} \cdot \sigma & 0 \\ 0 & v_F \mathbf{p} \cdot \sigma \end{pmatrix} \Psi = E \Psi. \quad (5.4)$$

The effect of the real electron spin is neglected in the discussion above, since we assume that energy levels for the electrons with same quantum number but with different spins are degenerate. If one considers the spin-orbit interaction in graphene, graphene shows the quantum spin hall effect (QSHE) (Kane and Mele, 2005a) and its band structure has a nontrivial  $\mathbb{Z}_2$  topological order (Kane and Mele, 2005b).

In order to calculate the electronic states in graphene nanostructures, Eq (5.4) has to be solved with the appropriate boundary conditions. This is simple for a well-defined graphene edge. In the case of a zigzag edge, depending on the sublattice we have either  $\Psi_A = \Psi'_A = 0$  or  $\Psi_B = \Psi'_B = 0$ . For armchair edges, the boundary condition is  $\Psi_A e^{iKr} + \Psi'_A e^{iKr} = 0$  and  $\Psi_B e^{iKr} + \Psi'_B e^{iKr} = 0$ .

The low energy carriers in graphene show ‘‘relativistic’’ behavior (Dirac electrons) with a very high Fermi velocity. However, questions such as how to confine electrons in graphene flakes and how this affects their electronic properties have not been experimentally addressed in well-defined graphene nanostructures. Theoretical studies have shown that the Dirac electrons cannot be confined in a quantum dot defined by a smooth electrostatic potential well on the graphene sheet and there are only quasi-bound states in this type of quantum dots (Silvestrov and Efetov, 2007; Matulis and Peeters, 2008; Bardarson *et al.*, 2009). A natural idea to confine the Dirac electrons in graphene is to cut the graphene sheet into fabricated nanostructures. Despite the enormous interest in science and technological potential of graphene nanostructures

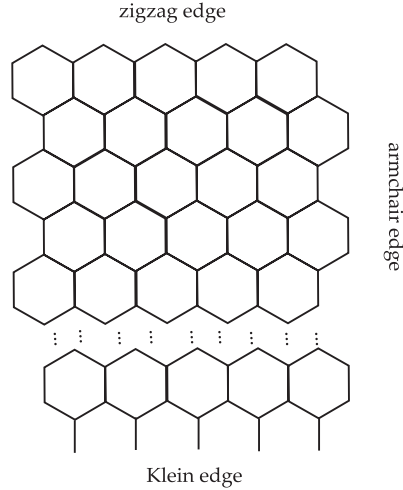


Figure 5.3: Some possible terminations of graphene sheet: zigzag edge, armchair edge and Klein edge. Here we only show the carbon skeleton.

(Rycerz *et al.*, 2007; Ponomarenko *et al.*, 2008; Jiao *et al.*, 2009; Kosynkin *et al.*, 2009; Ritter and Lyding, 2009; Cai *et al.*, 2010; Sprinkle *et al.*, 2010), it is still very difficult to fabricate and identify graphene nanostructures with well-defined edges. Lithographically defined g-QDs have been extensively studied, e.g. Han *et al.* (2007); Sols *et al.* (2007). Nevertheless, the predicted signatures of the edge states have not been observed because lithography is not precise enough to produce atomically well-defined structures. For graphene structures with well-defined edges (see Fig. 5.3), the boundary conditions were discussed by (Akhmerov and Beenakker, 2008). They showed that the zigzag terminated graphene edge exhibits metallic behavior and has continuous edge states. At the zigzag edge, the Dirac electrons only have intravalley scattering (Park *et al.*, 2011). The electron pseudospins will not be conserved during scattering at the zigzag edge.

In the previous experiments, macroscopic graphene sheets have been studied by STM and STS, focusing on electronic structure and scattering processes in epitaxial graphene (Rutter *et al.*, 2007) and the LDOS and charge puddles in graphene sheets deposited on an insulator (Feldman *et al.*, 2009; Zhang *et al.*, 2008, 2009; Deshpande *et al.*, 2009). It is, however, also possible to grow much smaller graphene nanostructures by CVD and characterize them with scanning probe methods (Wang *et al.*, 2011; Eom *et al.*, 2009; Coraux *et al.*, 2009).

In this chapter, we will discuss our LT-STM/STS experiments on g-QDs with well-defined atomic structures grown by CVD and on an Ir(111) substrate.

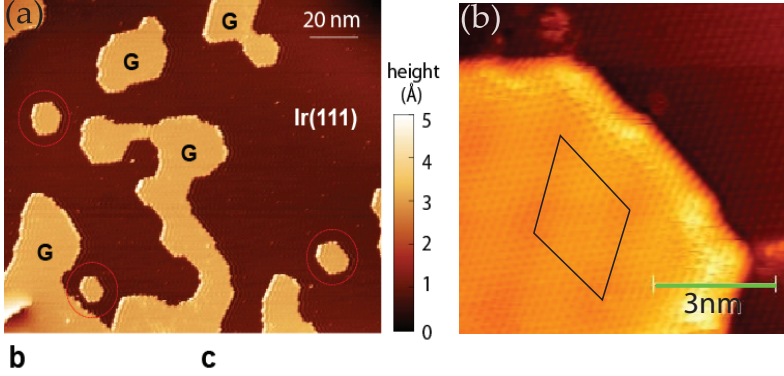


Figure 5.4: (a) Large scale STM imaging of graphene islands (G) on iridium substrate. ( $V_b = 1.0V$  and  $I_t = 40 pA$ ). (b) STM topography over an edge of a graphene flake with atomic resolution on both the iridium surface and the graphene flake.  $V_b = 0.1V$ ,  $I_t = 100pA$ . Atomic kinks can be observed in the image. The solid line is for eye guide of the moiré unit cell.

## 5.2 Experimental

We grew graphene flakes on Ir(111) using CVD following the procedure of Coraux *et al.* (2009). The iridium crystal was first cleaned by sputtering (1100K) and annealing (1500K) for several cycles. After the crystal was cooled down to 570K, ethylene ( $C_2H_2$ ) was deposited ( $10^{-7}mbar$  for 10 seconds). The g-QD size could then be controlled by the growth temperature (Coraux *et al.*, 2009), larger (smaller) g-QDs were grown by heating the sample to 1470K (1170K) for 10 s. After the CVD growth of the g-QDs, the sample was inserted into a low temperature STM ( $T=4.7K$ ) housed in the same vacuum system (base pressure  $< 10^{-10}mbar$ ). We used PtIr tips and the bias voltage  $V_b$  was defined as sample voltage with respect to that of the tip.  $dI/dV_b$  signal was recorded with a lock-in amplifier by applying a small sinusoidal variation to the bias signal (typically 30mV rms at 600Hz). This gives an energy resolution of about 75meV in our STS experiments (Morgenstern, 2003). To ensure that the modulation signal would not couple to the feedback loop, a 300Hz low-pass filter was used for the feedback input.

A STM topography images of the sample surfaces are shown in Fig. 5.4. We find interconnected graphene patches as well as isolated g-QDs. The growth method yields a relatively broad distribution of different g-QD sizes ranging from a couple of nanometers to ca. 20nms in diameter, most of them with a roughly hexagonal shape.

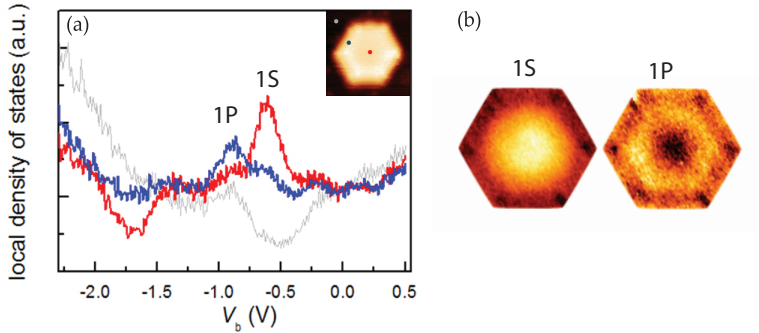


Figure 5.5: The  $d\ln I/d\ln V$  spectra taken on top of the center (blue), edge (red) of the flake and on top of the iridium surface (gray). Inset: The STM topography of the graphene flake with 7 hexagonal carbon rings at each edge. (b) Measured LDOS maps at energies corresponding to the two resonances in the spectra shown in panel (a).

### 5.3 Results and discussions

We find that all the graphene flakes have edges terminated in the zigzag direction (corresponding to the close-packed atomic rows of the underlying Ir(111) surface) with a very small roughness. By extrapolating atomic positions from atomically resolved STM images (see Fig. 5.4(b)<sup>4</sup>), we identify the relative positions of carbon atoms and iridium atoms. The center of the moiré pattern is located where carbon hexagons are centered on top of the iridium atoms. The areas with higher carbon-iridium distance correspond to regions where the carbon hexagons are centered at the FCC/HCP positions of the iridium surface. We also noticed that there are single atomic kinks, which have a spacing determined by the moiré period, at the edges of large graphene flakes (diameter larger than 3nm)<sup>6</sup>.

We now focus on the delocalized, quantum confined states inside the g-QDs. We can access the LDOS of graphene by measuring the  $dI/dV_b$  signal. One set of conductance spectra measured on a small perfectly hexagonal flake with 7 benzene rings at each edge is shown in Fig. 5.5. At positive bias, the spectra recorded on the g-QD and on the Ir(111) substrate appear very similar to each other. At negative bias, we can see resonant peaks that stem from the electronic structure of the g-QD.

There is a pronounced maximum of the LDOS measured in the center of the flake (Fig. 5.5(a)) at a bias of  $-0.6V$ . Moving away from the center of the flake, the intensity of this peak is reduced, and another resonance emerges at a bias of  $-0.9V$ . We can map the spatial shape of the orbitals responsible for these resonances by

<sup>4</sup>This may be taken with a molecule modified tip; we also have atomic resolution on the iridium surface.

<sup>6</sup>for details on the moiré pattern, see Chapter 4 of this thesis.

measuring the  $dI/dV_b$  signal during STM imaging under constant-current feedback at biases corresponding to the resonances (Fig. 5.5(b)). These states have familiar appearance of the lowest energy levels of the textbook "particle-in-a-box" problem and can be characterized using symmetry labels borrowed from atomic physics. The lowest energy state has  $1S$  symmetry (no nodal planes) and the first excited state is composed of two  $1P$  type orbitals ( $1P_x$  and  $1P_y$ ) which are degenerate in this case of a perfect hexagonal g-QD. STM probes the sum of the squared wavefunctions  $\psi_{1P_x}^2 + \psi_{1P_y}^2$  leading to a doughnut shaped  $dI/dV_b$  signal as we observe in the experiment.

We note here that at positive bias, electronic resonances with clear peaks in the  $dI/dV_b$  spectrum cannot be observed. Base on DFT calculations on Ir(111), there is a dense set of energy bands above the Fermi energy at the  $K$  point of the Brillouin zone. It is likely that interaction with these states masks the intrinsic graphene states at positive bias (Pletikoscic *et al.*, 2010).

We assume that the free carriers in these g-QDs still have the linear relation of Eq. (5.1). These electronic states can be described by the *Klein-Gordon equation*

$$-\hbar^2 v_F^2 \nabla^2 \Psi = E^2 \Psi, \quad (5.5)$$

where  $\Psi$  is the hybridized state of the two pseudospins, including valley degeneracy. We use the experimentally determined geometries of the g-QDs in our calculations. The boundary condition is  $\Psi = 0$ . It is clear that the KG equation cannot be used to model the edge states (in contrast to the Dirac equation and TB calculations (Castro Neto *et al.*, 2009; Son *et al.*, 2006; Brey and Fertig, 2006)). However, as shown below, the results from solving the Klein-Gordon equation give remarkably good agreement for the quantum confined levels with both experimental results and atomistic tight binding calculations, which should yield the most realistic description of the electronic properties of our g-QDs.

We have measured the LDOS at different biases on a graphene flake as shown in Fig. 5.6(a). The periodic variation with a period of 2.5 nm seen on the topographic STM images is a moiré pattern resulting from the lattice mismatch between graphene and Ir as we discussed in the previous chapter. The STM contrast results mostly from a small geometric modulation of the graphene structure. Our calculations neglecting this moiré induced potential modulation yield quantitative agreement with the experimental results and the expected potential modulation due to the moiré pattern is small compared to the confinement energy in our g-QDs. While these facts indicate that the electronic effects of the moiré pattern can be neglected, it is clear that the sizes of these g-QDs are determined by the moiré period. The sizes of all the flakes correspond to the integer multiple of the moiré period within one graphene lattice constant. The kinks on the edges of the g-QD are also spaced by roughly one moiré period.

The shape asymmetry of the g-QD breaks the degeneracies (e.g.  $1P_x$  and  $1P_y$  states) of the purely hexagonal g-QD. This can be seen in the measured LDOS maps shown in Fig. 5.6: after the  $1S$  state (bias -0.25V), we observe an increased intensity at the top and bottom of the end of the g-QD consistent with the  $1P_y$  envelope wavefunction along the long g-QD axis (bias -0.3V). At more negative bias, the  $1P_x$  state

also contributes and the long g-QD edges are brighter (bias -0.35V). Subsequently, the next eigenstate becomes relevant, which is seen as an increased intensity in the middle of the g-QD (bias -0.4V).

The experimental LDOS is broadened compared to the discrete eigenvalues of the Klein-Gordon equation due to mainly two physical effects (in addition to the instrumental broadening due to the ac bias modulation used to measure the  $dI/dV_b$  signal). The first effect is simple life-time broadening caused by the coupling with the substrate. The second one is related to the atomic scale details neglected in the solution of Eq. (5.5). The solutions of the Klein-Gordon equation are related to the LDOS based on atomistic theories; in the latter the number of molecular orbitals (MOs) (every carbon atom contributes one occupied state in the  $\pi$  band) is much larger than the number of energy eigenvalues of Eq. (5.5) over a given energy interval. The eigenvalues of Eq. (5.5) correspond to the energies with higher density of MOs. The MOs based on a microscopic calculation are more spread out in energy; this reflects the lifting of degeneracies due to the lack of symmetry of the atomic-scale g-QD geometry. This effect is naturally absent in the Klein-Gordon equation description that neglects atomic scale details, including the presence of two different carbon sublattices.

In order to compare experiment and theory in detail, we have generated a series of theoretical LDOS maps, which are calculated as a weighted sum of squares of wavefunctions close to a given energy (see Fig. 5.6). In the case of the calculations based on the Klein-Gordon equation, the wavefunctions and their eigenenergies are given by the solution of Eq. (5.5) using the overall shape of the g-QD. In the tight-binding calculations (we used third-nearest neighbor tight-binding) (Castro Neto *et al.*, 2009; Son *et al.*, 2006; Hancock *et al.*, 2010), they correspond to the calculated MOs for the g-QD with an exact atomic structure as obtained from experiment (Fig. 5.6(a)). Based on a comparison between the experimental and computed LDOS maps, we have identified energies that give the same spatial features in the LDOS with an associated error estimate indicated by error bars in Fig. 5.6(e).

It is clear that with the Fermi velocity  $v_F$  as the only adjustable parameter (in case of tight-binding calculations,  $v_F$  is directly related to the value of the hopping integrals), both calculations agree strikingly well with the experiments. This is also evident from Fig. 5.6(e), where we show the correspondence between the experimental and theoretical energies. This gives the Fermi velocity  $v_F = (6.2 \pm 0.1) \times 10^5 m/s$  as the best-fit to both the Klein-Gordon equation and the tight-binding calculations. The two theories yield slightly different values for the doping of the g-QD, i.e. the intercept of the  $y$ -axis, due to the differences in the theoretical approaches.

In fact, the Schrödinger equation predicts the same spatial distribution of the LDOS as the Klein-Gordon equation since both are second order linear differential equations; the corresponding eigenenergies are related as  $E_s = E_{KG}^2/2mv_F^2$ . This also explains the different dispersion relations for free electrons, which are either parabolic (Schrödinger) or linear (Klein-Gordon). Moreover, the energy of the lowest (and the other) quantum confined states scale as  $1/A^{1/2}$  ( $A$  is the area of the g-QD) in the case of the relativistic massless particles, instead of  $1/A$  for the particles obeying the

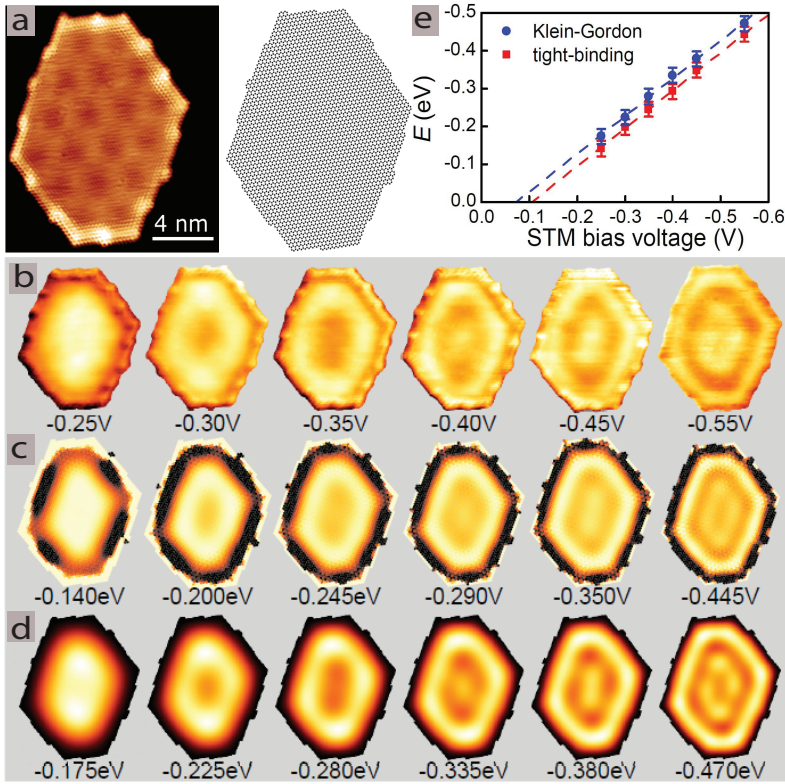


Figure 5.6: (a) An example graphene flake with atomic from the STM topography. (b) The  $dI/dV_b$  conductance maps of the flake shown in (a) at different biases under constant-current feedback ( $I=1\text{nA}$ ). (c) The calculated LDOS based on Eq. 5.5. (d) LDOS calculated by third-nearest neighbor tight-binding model. (e) Correspondence between the experimental and the calculated energies based on tight-binding (red squares) and the Klein-Gordon equation (blue circles) calculated with  $v_F = (6.2 \pm 0.1) \times 10^5 \text{m/s}$ .

Schrödinger equation. We show in Fig. 5.7 that the free charge carriers in our g-QDs fulfil the condition  $E \propto 1/A^{1/2}$  and have a linear dispersion. Fig. 5.7(b) shows the energy of the lowest quantum confined level (determined by the peak position in  $dI/dV_b$  vs.  $V_b$  spectra acquired at the center of the g-QD) on many different g-QDs. The dashed line is a fit with the expected  $1/A^{1/2}$  scaling.

In Fig. 5.7(c), we show the correspondence between the experimental energies (x-axis) and the theoretical energies calculated with the Klein-Gordon equation (y-axis) for many states on several g-QDs. The one-to-one correspondence confirms the linear dispersion of the quantum confined states in g-QDs. The corresponding Fermi velocity  $v_F = (6.0 \pm 0.3) \times 10^5$  m/s is in line with the previous results on macroscopic graphene samples on Ir(111) (Pletikosić *et al.*, 2009; Rusponi *et al.*, 2010; Starodub *et al.*, 2011). Remarkably, we do not observe any change of  $v_F$  down to the smallest g-QD that we have measured.

## 5.4 Summary

In this chapter we discussed our STM and STS work aimed at understanding the quantum confined energy states and their spatial distribution in atomically resolved graphene nanoflakes. The experimental LDOS consists of a number of molecular orbitals close in energy, which we have demonstrated by tight-binding calculations on the experimentally obtained atomic structure of the g-QD. The clusters of these energy states can be understood and reproduced by considering a relativistic wavefunction for massless particles. Our experiment shows that the intrinsic electronic states of graphene nanoflakes can be studied on a weakly coupled metal surface (e.g. Ir(111)). These systems can act as future test beds for studying the effects of chemical modifications or doping of graphene.

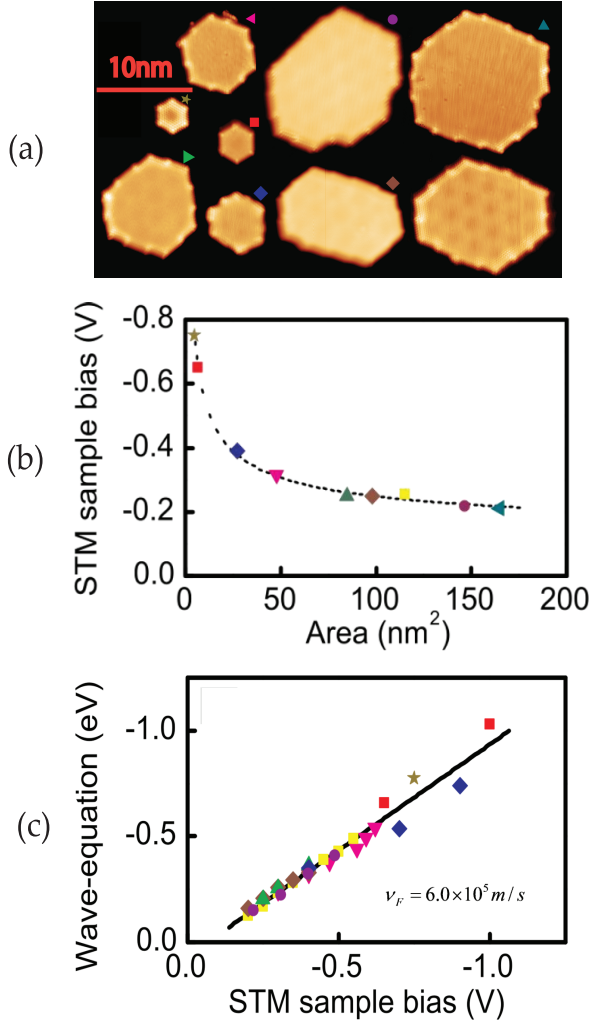


Figure 5.7: Electronic structure of g-QDs as a function of their size. (a) STM topography images of the g-QDs we measured. (b) STM sample bias corresponding to the  $S$  state as a function of the area  $A$  of the g-QD. The dashed line is a fit to  $1/A^{1/2}$ . (c) The correspondence between the energies derived from the STM experiments (x-axis) and those calculated from Klein-Gordon equation using a single value for  $v_F$ .

---

## Chapter 6

# CO-CO intermolecular interaction probed with nc-AFM

### 6.1 Introduction to the problem

Intermolecular interaction is an important concept for both physics and chemistry. For physics, it is critical for understanding the formation of different condensed states of matter (Barker and Henderson, 1976; Feinberg *et al.*, 1989). It is also crucial for understanding the chemical structures (Reed *et al.*, 1988). Intermolecular interactions can be indirectly probed by measuring the bulk properties of a certain condensed phase and subjecting them to an analysis based on statistical physics. Alternatively, *ab initio* computational studies are also widely used to calculate the intermolecular interaction. However, it is very difficult to accurately reproduce the interaction in the van der Waals (vdW) range. Despite the long history of the study of the van der Waals force (Margenau, 1939), compared to the short range interaction (i.e. Pauli repulsion, chemical bonding) and long range interaction (e.g. multi pole interaction), it is still not been fully characterized and probing it directly is an experimental challenge. One of the reasons is that the intermolecular interaction is normally very weak (range from a few meV to few tens of meV ). In order to measure it one needs very high force sensitivity. In addition, it is not easy to couple the intermolecular interaction with simple optical and electrical processes because the intermolecular interaction is a many body problem, intrinsically. Furthermore, to measure the intermolecular interaction between individual molecules, one needs to “hold” them and precisely control their separation. With these concerns in mind, we will show that nc-AFM is one of the tools capable of reaching these requirements.

A schematic illustration of the AFM-based approach to measure the intermolecular interaction between two molecules is shown in Fig. 6.1. From the sketch we can

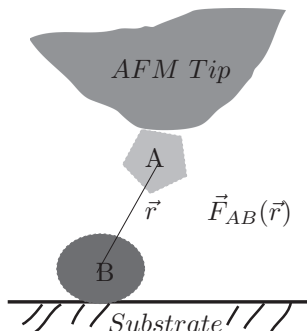


Figure 6.1: (Color online) Illustration of using nc-AFM to measure the intermolecular interaction, where  $\vec{r}$  is the distance between molecules *A* and *B* and  $\vec{F}_{AB}(\vec{r})$  is the interaction force in between.

already ask many questions about this approach. How to extract the intermolecular interaction from the background signals caused by the tip and substrate? How do the stability of the bonding between the tip and the molecule and the oscillation of the tip affect the measurements? How to attach the molecule to the tip apex and check that? We will try to address some of these questions with our experimental results.

Low-temperature STM (LT-STM) is known for being able to manipulate individual atoms (Eigler and Schweizer, 1990; Stroscio and Celotta, 2004; Stroscio *et al.*, 2006) and molecules (Grill *et al.*, 2007; Moresco, 2004; Choi *et al.*, 2006). Moreover, it can control chemical reactions and charges at the molecular scale (Hahn and Ho, 2001; Hla and Rieder, 2003; Mikaelian *et al.*, 2006; Wegner *et al.*, 2008), and be used to study photon coupling processes on a single molecule level (Wu *et al.*, 2006). These successes are due to the relative ease of achieving high spatial resolution and the fact that STM directly probes the electronic structure of the sample. On the other hand, AFM uses tip-sample interaction force as the feedback signal. At first sight, it is natural to expect AFM would reach similar resolution as STM. Still, only recent developments of nc-AFM have made it possible to reach this level of performance. In addition to atomic topography imaging (Hembacher *et al.*, 2003; Giessibl, 2005), nc-AFM has been recently used to probe the surface interaction potential (Caciuc *et al.*, 2005, 2008) and to manipulate atoms and characterize the related forces (Oyabu *et al.*, 2003; Sugimoto *et al.*, 2005; Ternes *et al.*, 2008). For a more detailed account of the force measurements with nc-AFM, we point to the extensive reviews on the subject, e.g. Morita and Giessibl (2009).

The system we focus here is a carbon monoxide molecule on the Cu(111) surface studied by nc-AFM using CO-terminated tips. It is well known both in STM and AFM that the tip termination has a crucial effect on the topography imaging and theories have been developed for this (DRAKOVA *et al.*, 2006; Hembacher *et al.*, 2004; Enevoldsen *et al.*, 2007, 2008; Hofer *et al.*, 2003; Kantorovich and Trevethan, 2004a; Pou *et al.*, 2009). Previous experiments have demonstrated that a carbon monoxide

terminated tip (formed by controllable vertical manipulation of a CO molecule from the sample surface onto the tip apex) forms a well-defined tip apex and yields enhanced image resolution (Gross *et al.*, 2009, 2010). In this chapter, we will use the same approach and present a precise measurement of intermolecular forces between two CO molecules: one absorbed on the Cu(111) single crystal substrate and the other on the AFM tip apex.

## 6.2 Experimental

We used (111)-terminated copper single crystal as the substrate, which was cleaned by several sputtering-annealing cycles. The AFM and STM experiments were carried out in UHV and LHe temperature. The Qplus sensor (resonance frequency 21575 Hz and quality factor of 21600) was used in the frequency modulation mode with a tip oscillation amplitude of  $A = 67 \text{ pm}$ . All the AFM experiments were carried out at zero bias voltage. The tip was cleaned by controlled contact with the copper surface, resulting in a copper-coated tip. A CO molecule was vertically manipulated onto the tip as described by previously and it absorbs with the carbon atom towards the metal tip (Gross *et al.*, 2009). The presence and orientation of the CO molecule on the tip apex was verified by the shape and characteristic change in the STM contrast of imaging another CO molecule from a depression (metal tip) to a protrusion (CO terminated tip) as illustrated in the insets of Fig. 6.2(a) and 6.2(b).

## 6.3 Results and discussion

AFM images acquired under constant frequency shift conditions are shown in Fig. 6.2(a) and 6.2(b) with a clean metal tip and a CO terminated tip, respectively. CO imaged with a clean metal tip appears as a protrusion (height ca.  $25 \text{ pm}$ ) as can be seen in the cross-section profile shown in Fig. 6.2(a) indicating that there are attractive interactions between the tip and the CO molecule on the surface. Decreasing the  $\Delta f$  setpoint further results in lateral manipulation of the CO molecule. In contrast, CO appears as a depression-provided that the  $\Delta f$  setpoint is sufficiently negative-when imaged with a CO-terminated tip. This indicates that we are able to approach the CO sufficiently close such that repulsive short range chemical interactions contribute significantly to the total force gradient. This reduces the total attractive ( $\Delta f$  is still negative) interaction and the tip has to approach the surface to maintain constant  $\Delta f$ . Again, decreasing the  $\Delta f$  setpoint further resulted in lateral manipulation of the CO along the surface.

To get a more quantitative handle on the interaction of the tip (either metallic or functionalized with a CO molecule) with the CO on the surface, we acquired constant height line scans at different tip-sample distances over the CO molecule. The results obtained with a CO terminated tip are shown in Fig. 6.3(a). Before further analysis of the frequency shift directly above a CO molecule, the measured background signal (independent of the lateral position) due to the vdW interaction between the tip and

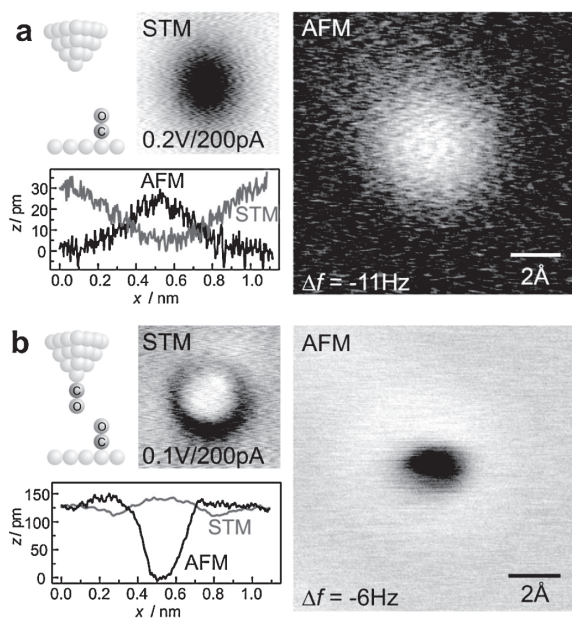


Figure 6.2: (Color online) STM and AFM images of a CO molecule adsorbed on Cu(111) surface acquired with (a) a clean metal tip and (b) a tip that is terminated by a CO molecule. The line profiles are taken from the images across the middle of the molecule. All images were taken at constant current (STM) and constant frequency shift (AFM) with setpoints indicated in the figure.

the Cu was subtracted from the line scans (see Fig. 6.3(b)). It can be seen that the background-corrected signal is attractive at large tip-sample distances ( $z > 0.2 \text{ nm}$ ). As we reduce the tip-sample separation, we find an increasing repulsive interaction that starts to saturate at the closest achievable distances ( $z < 50 \text{ pm}$ ). The data are represented in a color scale plot in Fig. 6.3(c), where the  $x$  is the lateral position ( $x = 0$  indicates the position directly above the CO molecule) and  $z$  is the tip-sample distance. The height  $z = 0$  is taken as the closest achievable tip-sample separation; approaching the tip more closely resulted in lateral manipulation of the adsorbed CO molecule. We used the method developed by Sader and Jarvis (2004) to convert the measured  $\Delta f$  to the vertical force  $F_z$ ,

$$F_z(z) = 2k \int_z^\infty \left(1 + \frac{a^{1/2}}{8\sqrt{\pi(t-z)}}\right) \Omega(t) - \frac{a^{3/2}}{\sqrt{2(t-z)}} \frac{d\Omega(t)}{dt} dt, \quad (6.1)$$

where  $\Omega(z) = \Delta f(z)/f_0$ ,  $f_0$  is the tip resonance frequency far from the substrate,  $k$  is the spring constant of the cantilever,  $a$  is the oscillation amplitude and  $z$  is the closest separation between tip and the surface. The quartz tuning fork used in the present study had  $k = 1800 \text{ N/m}$ . The calculated vertical force map obtained with a CO terminated tip over an adsorbed CO molecule is shown in Fig. 6.3(d). It indicates the presence of both attractive (red) and repulsive (blue) regions depending on the lateral and vertical position of the tip. We have carried out the same experiment using a clean metallic tip and consistent with the AFM imaging, we only detect attractive force between the metallic tip and adsorbed CO molecule.

The interaction potential between the tip and the substrate can be obtained by integrating the vertical force. The results for the background-corrected potential values are shown in Figs. 6.4(a) and 6.4(b) for the CO-terminated and clean metal tips, respectively. As already suggested by the force maps, the interaction between the CO-terminated tip and the adsorbed CO molecule have both repulsive and attractive contributions, whereas only attractive contributions are present with a clean metal tip. To obtain further insight into the measured interaction energy maps, we have carried out a DFT (ADF2009.01B program with the dispersion corrected Perdew-Burke-Ernzerhof functional and triple-zeta plus double polarization basis set (te Velde *et al.*, 2001; Lenthe and Baerends, 2003)) and molecular mechanics (COMPASS force field (Yang *et al.*, 2004)) calculations. The molecular mechanics calculations were included to validate the use of semiempirical vdW correction in the DFT calculations. The results for two isolated CO molecules (based on molecular mechanics) are shown in the left half of Fig. 6.4(c). The other half of the panel shows the interaction energy calculated by DFT between an isolated CO molecule and a CO molecule adsorbed on a  $\text{Cu}_4$  cluster, which serves as a simple model of the AFM tip. The DFT results agree well with the force field based calculation. As can be seen, these model calculations without geometry relaxation agree with the experiment in a semiquantitative fashion. They correctly reproduce the magnitude and extent of the attractive part of the interaction potential, which is mostly due to attractive vdW interaction between the two CO molecules. However, both DFT and molecular mechanics overestimate the

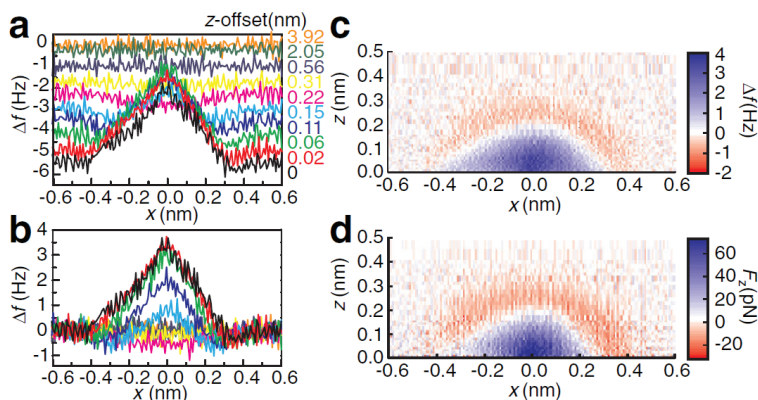


Figure 6.3: Mapping the force landscape over a CO molecule. (a) Frequency shift measured by constant height line scans over a CO molecule with a CO molecule adsorbed at the tip apex. Numbers indicate the  $z$  height of the line scans with respect to the closest achievable tip-sample separation; i.e.,  $z < 0$  results in lateral manipulation of the CO molecule. (b) Same data after removing the constant background due to the Cu(111) substrate. (c) The background-corrected  $\Delta f$  and (d) the corresponding vertical force  $F_z$  landscape presented in a color scale plot for the CO terminated tip as a function of the horizontal position and tip-sample distance.

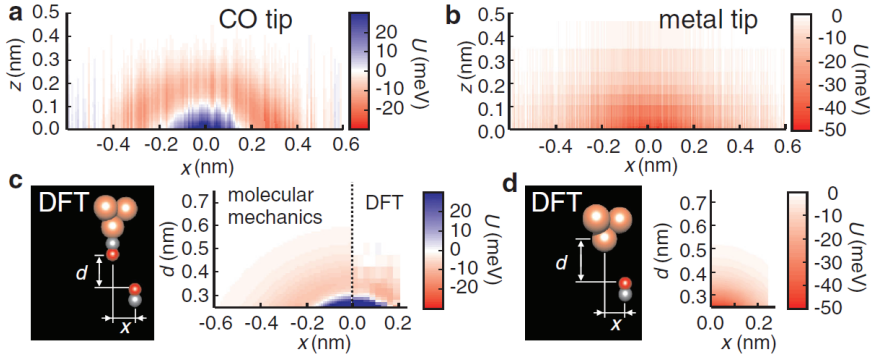


Figure 6.4: Experimental interaction energy obtained by integration of vertical force data with (a) a CO terminated and (b) a clean metal tip. (c) Calculated interaction energy between two CO molecules based on molecular mechanics between two isolated CO molecules and DFT calculations between a CO molecule and a CO adsorbed on a  $Cu_4$  cluster. (d) The corresponding DFT calculation for the interaction energy between a  $Cu_4$  cluster and an isolated CO molecule.

repulsive potential at short distances, which we will show to result from the elasticity of the adsorbed CO molecules.

The purely attractive interaction in the case of a clean metal tip can also be reproduced by the DFT calculations, where we use a  $Cu_4$  cluster as a very simple model of the AFM tip and calculate its interaction with an isolated CO molecule (Fig. 6.4(d)). The negative  $U$  is due to the attractive vdW interaction and, at short distances, chemical bonding between the last tip atom and the oxygen atom in CO.

We have carried out more detailed DFT calculations including  $Cu_4$  and  $Cu_{10}$  clusters as simple models of the tip and the substrate, respectively, in order to understand why the measured repulsive interaction between two CO molecules is much weaker than that calculated between two aligned CO molecules (Fig. 6.5(a)). The geometries of the Cu clusters were fixed, and the CO molecules were allowed to relax (with no symmetry restrictions) to minimize the total energy of the system. As can be seen in the calculated geometries at different distances, both CO molecules undergo relaxation as the tip-substrate distance is decreased. This reduces the repulsive interaction and brings the calculated interaction energy significantly closer to the experimental results (Fig. 6.5(b)). Hence, chemical repulsion between the CO molecules is relaxed at the expense of weaker bonding of the CO molecules to the Cu atoms of the tip and substrate, respectively.

What is actually measured in our experiment? This is generally problematic in AFM, where it has been realized that the tip structure and the relaxation usually have to be considered in understanding the force response (Hofer *et al.*, 2003; Kantorovich and Trevethan, 2004b; Pou *et al.*, 2009). The background correction procedure implies

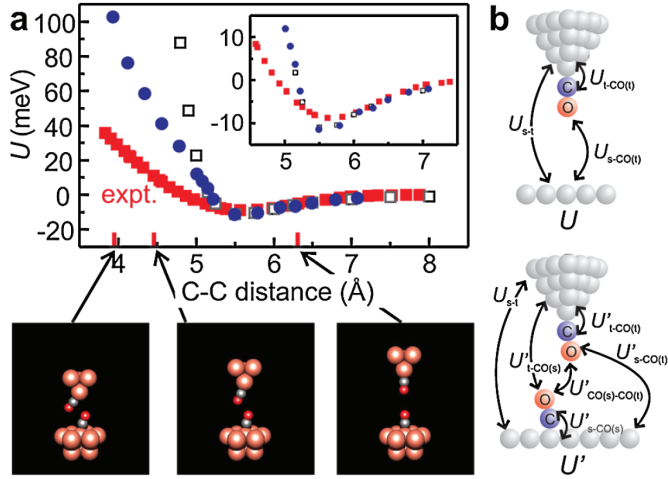


Figure 6.5: Effect of relaxation on the force distance curves. (a) The experimental background-corrected interaction energy directly above a CO molecule (filled red squares, data taken from Fig. 6.4(a)) compared with DFT calculation of two isolated CO molecules without geometry relaxation (open grey squares) and the full model that includes  $Cu_4$  and  $Cu_{10}$  clusters as tip and substrate models, respectively, and where the CO molecules are allowed to relax (filled blue circles). Inset is a zoom into the attractive regime. The DFT energies correspond to the experimental situation, that is, the energy difference between a CO-modified tip approaching a bare metal substrate or an adsorbed CO molecule. The tip-sample distance in the experimental data has been shifted to overlay the vdW part of the interaction potential with the theoretical predictions. The lower images show the relaxed geometry at tip-substrate distances indicated by the arrows. (b) Schematics of the different interaction energy terms for the case of an CO-terminated tip on top of a clean metal substrate (top, term  $U_{s-CO(s)}$  not indicated). and on top of an adsorbed CO molecules (bottom).

that we are measuring the energy difference ( $\Delta U$ ) between a CO molecule adsorbed on the tip on top of a clean Cu(111) surface ( $U$ ) and on top of a CO molecule adsorbed on the substrate ( $U'$ ) (at a given tip-sample separation) (Fig. 6.5(b)):

$$\begin{aligned} \Delta U = & U'_{t-CO(s)} + (U'_{s-CO(s)} - U_{s-CO(s)}) + (U'_{s-CO(t)} - U_{s-CO(t)}) \\ & + (U'_{t-CO(t)} - U_{t-CO(t)}) + U'_{CO(t)-CO(s)}, \end{aligned} \quad (6.2)$$

where  $CO(s)$  and  $CO(t)$  refer to the CO molecule adsorbed on the substrate and tip. In the absence of relaxation, all the terms in the parentheses are zero. Based on the data shown in Fig. 6.4, we can estimate that the  $|U'_{t-CO(s)}| < 10 \text{ meV}$  even for the shortest distances in Fig. 6.5(a). In this case, it is possible to extract the interaction energy between the two CO molecules ( $U'_{CO(s)-CO(t)}$ ) directly from the experiment as it forms the major contribution to the measured interaction energy. However, if the CO molecules structurally relax, the terms in the parentheses are nonzero. While  $|U'_{s-CO(t)} - U_{s-CO(t)}|$  is small as vdW forces between the substrate and the CO adsorbed on the tip are not very sensitive to the small changes in the orientation and rotation of the CO, this is not necessarily the case for  $|U'_{s-CO(s)} - U_{s-CO(s)}|$  and  $|U'_{t-CO(t)} - U_{t-CO(t)}|$ . The decreased repulsion between the CO molecules due to the geometric relaxation occurs at the expense of these adsorption energy terms. Finally, the problem with the  $|U'_{t-CO(s)}|$  term is that it cannot be directly measured experimentally as it is the interaction between the tip and the CO at the relaxed geometry.

## 6.4 Summary and outlook

In this chapter, we use non-contact AFM to probe the intermolecular interaction between two CO molecules. Our results show that at close tip-sample distances, the geometric relaxation of these molecules has to be considered. The relaxation of the molecules is an important factor in the interpretation of the nc-AFM images taken with the molecule-functionalized tips and it gives the physical limits of measuring intermolecular interactions with scanning probe methods.

It will be of immense interest to combine STM and AFM measurements in the future: in addition to atomic resolution imaging on molecules, electrostatic effects (e.g. contact potential, charge distributions) can be studied simultaneously with the information on the local density of states given by the STM. It is also worthwhile to note that nc-AFM could be used to directly probe the interaction between small molecules ( $CO, CO_2, N_2$ ) and catalytically active sites in either molecular catalysts or on catalytic surfaces.

## 6.5 Acknowledgement

We thank L. Gross, G. Meyer and F. Giessibl for discussions.



---

# Bibliography

- Abramovitch, D. Y., S. B. Andersson, L. Y. Pao, and G. Schitter, 2007, Proceedings of the 2007 American Control Conference , 3488.
- Akhmerov, A. R., and C. W. J. Beenakker, 2008, Phys. Rev. B **77**(8), 085423.
- Albrecht, T. R., P. Grutter, D. Horne, and D. Rugar, 1991, J. Appl. Phys. **69**, 668.
- Alivisatos, A. P., W. Gu, and C. Larabell, 2005, Annu. Rev. Biomed. Eng. **7**, 55.
- Alivisatos, A. P., T. D. Harris, P. G. Carrol, M. L. Steigerwald, and L. E. Brus, 1989, J. Chem. Phys. **90**(7), 3463.
- Alivisatos, P., 2004, Nature Biotechnology **22**, 47.
- Allan, G., and C. Delerue, 2004, Phys. Rev. B **70**(24), 245321.
- An, J. M., A. Franceschetti, and A. Zunger, 2007, Phys. Rev. B **76**(4), 045401.
- Appelbaum, J. A., and W. F. Brinkman, 1969, Phys. Rev. **186**(2), 464.
- Ashino, M., A. Schwarz, T. Behnke, and R. Wiesendanger, 2004, Phys. Rev. Lett. **93**(13), 136101.
- Averin, D. V., A. N. Korotkov, and K. K. Likharev, 1991, Phys. Rev. B **44**, 6199.
- B. J. LeRoy, J. K. . C. D., S. G. Lemay, 2004, Nature **432**, 371.
- Bakkers, E. P. A. M., Z. Hens, A. Zunger, A. Franceschetti, L. P. Kouwenhoven, L. Gurevich, and D. Vanmaekelbergh, 2001, Nano Lett. **1**(10), 551.
- Bakkers, E. P. A. M., and D. Vanmaekelbergh, 2000, Phys. Rev. B **62**(12), 7743.
- Balet, L. P., S. A. Ivanov, A. Piryatinski, M. Achermann, and V. I. Klimov, 2004, Nano Letters **4**(8), 1485.
- Banin, U., Y. Cao, D. Katz, and O. Millo, 1999, Nature **400**, 542.
- Banin, U., and O. Millo, 2003, Annu. Rev. Phys. Chem. **54**, 465.

- Bardarson, J. H., M. Titov, and P. W. Brouwer, 2009, *Phys. Rev. Lett.* **102**(22), 226803.
- Bardeen, J., 1961, *Phys. Rev. Lett.* **6**(2), 57.
- Barker, J. A., and D. Henderson, 1976, *Rev. Mod. Phys.* **48**(4), 587.
- Beenakker, C. W. J., 2008, *Rev. Mod. Phys.* **80**(4), 1337.
- Betzig, E., A. Lewis, A. Harootunian, M. Isaacson, and E. Kratschmer, 1986, *BIO-PHYS. J.* **49**, 269.
- Binnig, G., C. F. Quate, and C. Gerber, 1986, *Phys. Rev. Lett.* **56**(9), 930.
- Binnig, G., and H. Rohrer, 1982, *Helv. Phys. Acta* **5**, 726.
- Binnig, G., and H. Rohrer, 1987, *Rev. Mod. Phys.* **59**(3), 615.
- Binnig, G., and D. P. E. Smith, 1986, *Rev. Sci. Instrum.* **57**(8), 1688.
- Boebinger, G. S., A. F. J. Levi, S. Schmitt-Rink, A. Passner, L. N. Pfeiffer, and K. W. West, 1990, *Phys. Rev. Lett.* **65**(2), 235.
- Brey, L., and H. A. Fertig, 2006, *Phys. Rev. B* **73**(23), 235411.
- Caciuc, V., H. Hölscher, and S. Blügel, 2005, *Phys. Rev. B* **72**(3), 035423.
- Caciuc, V., H. Hölscher, D. Weiner, H. Fuchs, and A. Schirmeisen, 2008, *Phys. Rev. B* **77**(4), 045411.
- Cai, J., P. Ruffieux, R. Jaafar, M. Bieri, T. Braun, S. Blankenburg, M. Muoth, A. P. Seitsonen, M. Saleh, X. Feng, K. Müllen, and R. Fasel, 2010, *Nature* **466**, 470.
- Carpenter, B. A., E. A. Zibik, M. L. Sadowski, L. R. Wilson, D. M. Whittaker, J. W. Cockburn, M. S. Skolnick, M. Potemski, M. J. Steer, and M. Hopkinson, 2006, *Phys. Rev. B* **74**(16), 161302.
- Castro Neto, A. H., F. Guinea, N. M. R. Peres, K. S. Novoselov, and A. K. Geim, 2009, *Rev. Mod. Phys.* **81**(1), 109.
- Pletikosić, I., M. Kralj, P. Pervan, R. Brako, J. Coraux, A. T. N'Diaye, C. Busse, and T. Michely, 2009, *Phys. Rev. Lett.* **102**(5), 056808.
- Chen, C. J., 1990, *Phys. Rev. B* **42**(14), 8841.
- Chen, C. J., 1992, *Phys. Rev. Lett.* **69**(11), 1656.
- Chin, P. T. K., C. de Mello Doneg, S. S. van Bavel, S. C. J. Meskers, N. A. J. M. Sommerdijk, and R. A. J. Janssen, 2007, *J. Am. Chem. Soc.* **129**(48), 14880.

- Choi, B.-Y., S.-J. Kahng, S. Kim, H. Kim, H. W. Kim, Y. J. Song, J. Ihm, and Y. Kuk, 2006, Phys. Rev. Lett. **96**, 156106.
- Cleveland, J. P., S. Manne, D. Bocek, and P. K. Hansma, 1993, Rev. Sci. Instrum, **64(2)**, 403.
- Coraux, J., A. T. N. Diaye, M. Engler, C. Busse, D. Wall, N. Buckanie, F.-J. M. zu Heringdorf, R. van Gastel, B. Poelsema, and T. Michely, 2009, New J. Phys. **11**, 023006.
- Corso, D., Andrea, Baroni, Stefano, Resta, Raffaele, and de Gironcoli Stefano, 1993, Phys. Rev. B **47(7)**, 3588.
- Dabbousi, B. O., J. Rodriguez-Viejo, F. V. Mikulec, J. R. Heine, H. Mattoussi, R. Ober, K. F. Jensen, and M. G. Bawendi, 1997, J. Phys. Chem. B **101 (46)**, 94639475.
- Delerue, C., and M. Lannoo, 2004, *Nanostructures: Theory and Modelling* (Springer).
- Deshpande, A., W. Bao, F. Miao, C. N. Lau, and B. J. LeRoy, 2009, Phys. Rev. B **79(20)**, 205411.
- Devreese, J., 2000, Arxiv preprint cond-mat/0004497 .
- DRAKOVA, D., M. NEDJALKOVA, and G. DOYEN, 2006, International Journal of Quantum Chemistry **106**, 1419.
- Dunn, R. C., 1999, Chem. Rev. **99**, 2891.
- Durig, U., 1999, Appl. Phys. Lett. **75**, 433.
- Eigler, D. M., and E. K. Schweizer, 1990, Nature **344**, 524.
- Elias, D. C., R. V. Gorbachev, A. S. Mayorov, S. V. Morozov, A. A. Zhukov, P. Blake, L. A. Ponomarenko, I. V. Grigorieva, K. S. Novoselov, F. Guinea, and A. K. Geim, 2011, Nature Physics **7**, 701.
- Emtsev, K. V., A. Bostwick, K. Horn, J. Jobst, G. L. Kellogg, L. Ley, J. L. McChesney, T. Ohta, S. A. Reshanov, J. Rhrh, E. Rotenberg, A. K. Schmid, *et al.*, 2009, Nature Materials **8**, 203.
- Enevoldsen, G. H., A. S. Foster, M. C. Christensen, J. V. Lauritsen, and F. Besenbacher, 2007, Phys. Rev. B **76(20)**, 205415.
- Enevoldsen, G. H., H. P. Pinto, A. S. Foster, M. C. R. Jensen, A. Kühnle, M. Reichling, W. A. Hofer, J. V. Lauritsen, and F. Besenbacher, 2008, Phys. Rev. B **78(4)**, 045416.
- Eom, D., D. Prezzi, K. T. Rim, H. Zhou, M. Lefenfeld, S. Xiao, C. Nuckolls, M. S. Hybertsen, T. F. Heinz, and G. W. Flynn, 2009, Nano Lett. **9**, 2844.

- Feibelman, P. J., 2008, Phys. Rev. B **77**(16), 165419.
- Feinberg, G., J. Sucher, and C. K. Au, 1989, Physics Reports **180**(2), 83.
- Feldman, B. E., J. Martin, and A. Yacoby, 2009, Nature Physics **5**, 889.
- Fermi, E., 1949, *Nuclear Physics: A Course Given by Enrico Fermi at the University of Chicago* (University of Chicago Press).
- Franceschetti, A., A. Williamson, and A. Zunger, 2000, J. Phys. Chem. B **104**, 3398.
- Fröhlich, H., 1952, Proceedings of the Royal Society of London. Series A, Mathematical and Physical Sciences **215**, 291.
- Fröhlich, H., and R. L. Platzman, 1953, Phys. Rev. **92**(5), 1152.
- Gadzuk, J. W., 1991, Phys. Rev. B **44**(24), 13466.
- Gao, L., J. R. Guest, and N. P. Guisinger, 2010, Nano Lett. **10**(9), 3512.
- Geim, A. K., and K. S. Novoselov, 2007, Nature Materials **6**, 187.
- Giessibl, F. J., 1997, Phys. Rev. B **56**(24), 16010.
- Giessibl, F. J., 2000, Appl. Phys. Lett. **76**(11), 1470.
- Giessibl, F. J., 2003, Rev. Mod. Phys. **75**(3), 949.
- Giessibl, F. J., 2005, Materials Today **8**, 32.
- Gorter, C. J., 1951, Physica **X VII**, no.8, 777.
- Grill, L., M. Dyer, L. Lafferentz, M. Persson, M. V. Peters, and S. Hecht, 2007, Nature Nanotechnology **2**, 687.
- Grodzińska, D., F. Pietra, M. A. van Huis, D. Vanmaekelbergh, and C. de Mello Doneg, 2011, J. Mater. Chem. **21**, 11556.
- Gross, L., F. Mohn, N. Moll, P. Liljeroth, and G. Meyer, 2009, Science **325**(5944), 1110.
- Gross, L., F. Mohn, N. Moll, G. Meyer, R. Ebel, W. M. Abdel-Mageed, and M. Jaspars, 2010, Nature Chemistry **2**, 821.
- Gross, L., N. Moll, F. Mohn, A. Curioni, G. Meyer, F. Hanke, and M. Persson, 2011, Phys. Rev. Lett. **107**(8), 086101.
- Gur, I., N. A. Fromer, M. L. Geier, and A. P. Alivisatos, 2005, Science **310**, 462.
- Hahn, J. R., and W. Ho, 2001, Phys. Rev. Lett. **87**(16), 166102.

- Hameau, S., Y. Guldner, O. Verzelen, R. Ferreira, G. Bastard, J. Zeman, A. Lemaître, and J. M. Gérard, 1999, *Phys. Rev. Lett.* **83**(20), 4152.
- Han, M. Y., B. Özyilmaz, Y. Zhang, and P. Kim, 2007, *Phys. Rev. Lett.* **98**(20), 206805.
- Hancock, Y., A. Uppstu, K. Saloriutta, A. Harju, and M. J. Puska, 2010, *Phys. Rev. B* **81**(24), 245402.
- Hansma, P. K., 1977, *Physics Reports* **30**, 145.
- Hanson, R., L. P. Kouwenhoven, J. R. Petta, S. Tarucha, and L. M. K. Vandersypen, 2007, *Rev. Mod. Phys.* **79**(4), 1217.
- Hartman, U., 1999, *Annu. Rev. Mater. Sci.* **29**, 53.
- Hembacher, S., F. J. Giessibl, and J. Mannhart, 2004, *Science* **305**, 380.
- Hembacher, S., F. J. Giessibl, J. Mannhart, and C. F. Quate, 2003, *PNAS* **100**(22), 12539.
- Hendry, E., M. Koeberg, F. Wang, H. Zhang, C. de Mello Donegá, D. Vanmaekelbergh, and M. Bonn, 2006, *Phys. Rev. Lett.* **96**(5), 057408.
- Hla, S.-W., and K.-H. Rieder, 2003, *Annu. Rev. Phys. Chem.* **53**, 307.
- Hofer, W. A., A. S. Foster, and A. L. Shluger, 2003, *Rev. Mod. Phys.* **75**(4), 1287.
- Hopfield, J. J., 1959, *J. Phys. Chem. Solids* **10**, 110.
- Houtepen, A. J., D. Kockmann, and D. Vanmaekelbergh, 2008, *Nano. Lett.* **8**(10), 35163520.
- Huang, K., and A. Rhys, 1950, *Proc. R. Soc. London, Ser. A* **204**, 406.
- Huang, K., and B. Zhu, 1988, *Phys. Rev. B* **38**(18), 13377.
- Israelachvili, J., 1992, *Intermolecular and Surface Forces* (Academic, London).
- Jaklevic, R. C., and J. Lambe, 1966, *Phys. Rev. Lett.* **17**, 1139, URL <http://link.aps.org/doi/10.1103/PhysRevLett.17.1139>.
- Jdira, L., P. Liljeroth, E. Stoffels, D. Vanmaekelbergh, and S. Speller, 2006, *Phys. Rev. B* **73**, 115305.
- Jdira, L., K. Overgaag, J. Gerritsen, D. Vanmaekelbergh, P. Liljeroth, and S. Speller, 2008a, *Nano. Lett.* **8**(11), 4014.
- Jdira, L., K. Overgaag, R. Stiufiuc, B. Grandidier, C. Delerue, S. Speller, and D. Vanmaekelbergh, 2008b, *Phys. Rev. B* **77**(20), 205308.

- Jiao, L., L. Zhang, X. Wang, G. Diankov, and H. Dai, 2009, *Nature* **458**, 877.
- Kane, C. L., and E. J. Mele, 2005a, *Phys. Rev. Lett.* **95**(22), 226801.
- Kane, C. L., and E. J. Mele, 2005b, *Phys. Rev. Lett.* **95**(14), 146802.
- Kantorovich, L. N., and T. Trevelyan, 2004a, *Phys. Rev. Lett.* **93**(23), 236102.
- Kantorovich, L. N., and T. Trevelyan, 2004b, *Phys. Rev. Lett.* **93**(23), 236102.
- Kastner, M. A., 1993, *Physics Today* **January**, 24.
- Kim, K. S., Y. Zhao, H. Jang, S. Y. Lee, J. M. Kim, K. S. Kim, J.-H. Ahn, P. Kim, J.-Y. Choi, and B. H. Hong, 2009, *Nature* **457**, 706.
- Kim, S., B. Fisher, H.-J. Eisler, and M. Bawendi, 2003, *J. Am. Chem. Soc.* **125**(38), 11466.
- Klein, D. L., R. Roth, A. K. L. Lim, A. P. Alivisatos, and P. L. McEuen, 1997, *Nature* **389**, 699.
- Klein, J., M. B. A. Lger, D. Dfourneau, and M. J. L. Sangster, 1973, *Phys. Rev. B* **7**, 2336.
- Klein, M. C., F. Hache, D. Ricard, and C. Flytzanis, 1990, *Phys. Rev. B* **42**(17), 11123.
- Klimov, V. I., 2007, *Annu. Rev. Phys. Chem.* **58**, 635.
- Klimov, V. I., S. A. Ivanov, J. Nanda, M. Achermann, I. Bezel, J. A. McGuire, and A. Piryatinsk, 2007, *Nature* **447**, 441.
- Konstantatos, G., I. Howard, A. Fischer, S. Hoogland, J. Clifford, E. Klem, L. Levina, and E. H. Sargent, 2006, *Nature* **442**, 180.
- Kosłowski, B., C. Dietrich, A. Tschetschetkin, and P. Ziemann, 2007, *Phys. Rev. B* **75**(3), 035421.
- Kosynkin, D. V., A. L. Higginbotham, A. Sinitskii, J. R. Lomeda, A. Dimiev, B. K. Price, and J. M. Tour, 2009, *Nature* **458**, 872.
- Kudera, S., L. Carbone, M. F. Casula, R. Cingolani, A. Falqui, E. Snoeck, W. J. Parak, and L. Manna, 2005, *Nano Lett.* **5**(3), 445.
- Lambe, J., and R. C. Jaklevic, 1968, *Phys. Rev.* **165**(3), 821.
- Lambert, K., B. D. Geyter, I. Moreels, and Z. Hens, 2009, *Chem. Mater.* **21**, 778.
- Landau, L. D., 1933, *Phys. Zeitschrift Sowjetunion* **3**, 644.
- Landau, L. D., 1965, *Collected Works of Landau, L. D.* (Pergamon, Oxford).

- Lauhon, L. J., and W. Ho, 2001, *Rev. Sci. Instrum.* **72**, 216.
- Lenthe, E. V., and E. J. Baerends, 2003, *Computational Chemistry* **24(9)**, 1142.
- Likharev, K. K., 1999, *Proc. IEEE* **87**, 606.
- Liljeroth, P., P. A. Zeijlmans van Emmichoven, S. G. Hickey, H. Weller, B. Grandidier, G. Allan, and D. Vanmaekelbergh, 2005, *Phys. Rev. Lett.* **95**, 086801.
- Liljeroth, P., L. Jdira, K. Overgaag, B. Grandidier, S. Speller, and D. Vanmaekelbergh, 2006a, *Phys. Chem. Chem. Phys.* **8**, 3845.
- Liljeroth, P., K. Overgaag, A. Urbieto, B. Grandidier, S. G. Hickey, and D. Vanmaekelbergh, 2006b, *Phys. Rev. Lett.* **97**, 096803.
- Loginova, E., S. Nie, K. Thürmer, N. C. Bartelt, and K. F. McCarty, 2009, *Phys. Rev. B* **80(8)**, 085430.
- Loth, S., M. Etzkorn, C. P. Lutz, D. M. Eigler, and A. J. Heinrich, 2010, *Science* **24**, 1628.
- Margenau, H., 1939, *Rev. Mod. Phys.* **11(1)**, 1.
- Martin, Y., C. C. Williams, and H. K. Wickramasinghe, 1987, *J. Appl. Phys.* **61**, 4723.
- Martocchia, D., P. R. Willmott, T. Brugger, M. Björck, S. Günther, C. M. Schlepütz, A. Cervellino, S. A. Pauli, B. D. Patterson, S. Marchini, J. Wintterlin, W. Moritz, *et al.*, 2008, *Phys. Rev. Lett.* **101(12)**, 126102.
- Matulis, A., and F. M. Peeters, 2008, *Phys. Rev. B* **77(11)**, 115423.
- McClure, J. W., 1956, *Phys. Rev.* **104(3)**, 666.
- Medintz, I. L., H. T. Uyeda, E. R. Goldman, and H. Mattoussi, 2005, *Nature Materials* **4**, 435.
- de Mello Donegá, C., P. Liljeroth, and D. Vanmaekelbergh, 2005, *Small* **1**, 1152.
- Melnikov, D. V., and W. B. Fowler, 2001, *Phys. Rev. B* **63(16)**, 165302.
- Meyer, G., and N. M. Amer, 1988, *Appl. Phys. Lett.* **53(12)**, 1045.
- Michalet, X., F. F. Pinaud, L. A. Bentolila, J. M. Tsay, S. Doose, J. J. Li, G. Sundaresan, A. M. Wu, S. S. Gambhir, and S. Weiss, 2005, *Science* **307**, 538.
- Mikaelian, G., N. Ogawa, X. W. Tu, and W. Hoa, 2006, *THE JOURNAL OF CHEMICAL PHYSICS* **124**, 131101.
- Milliron, D. J., S. M. Hughes, Y. Cui, L. Manna, J. Li, L.-W. Wang, and A. P. Alivisatos, 2004, *Nature* **430**, 190.

- Millo, O., D. Katz, Y. Cao, and U. Banin, 2001, *Phys. Rev. Lett.* **86**(25), 5751.
- Moresco, F., 2004, *Physics Reports* **399**, 175.
- Morgenstern, M., 2003, *Surface Review and Letters* **10**, 933.
- Morita, S., and R. Giessibl, F. and Wiesendanger (eds.), 2009, *Noncontact atomic force microscopy*, volume 2 (Springer Verlag).
- Moritz, W., B. Wang, M.-L. Bocquet, T. Brugger, T. Greber, J. Wintterlin, and S. Günther, 2010, *Phys. Rev. Lett.* **104**(13), 136102.
- Murray, C. B., C. R. Kagan, and M. G. Bawendi, 2000, *Annu. Rev. Mater. Sci.* **30**, 545.
- N'Diaye, A. T., S. Bleikamp, P. J. Feibelman, and T. Michely, 2006, *Phys. Rev. Lett.* **97**(21), 215501.
- N'Diaye, A. T., J. Coraux, T. N. Plasa, C. Busse, and T. Michely, 2008, *New J. Phys.* **10**(4), 043033.
- Niquet, Y. M., C. Delerue, and G. Allan, 2002, *Phys. Rev. B* **65**, 165334.
- Novoselov, K. S., A. K. Geim, S. V. Morozov, D. Jiang, Y. Zhang, S. V. Dubonos, I. V. Grigorieva, and A. A. Firsov, 2004, *Science* **306** (5696), 666.
- Ohta, T., A. Bostwick, T. Seyller, K. Horn, and E. Rotenberg, 2006, *Science* **313**, 951.
- Overgaag, K., P. Liljeroth, B. Grandidier, and D. Vanmaekelbergh, 2008, *ACS Nano* **2**, 600.
- Oyabu, N., O. Custance, I. Yi, Y. Sugawara, and S. Morita, 2003, *Phys. Rev. Lett.* **90**(17), 176102.
- Pandey, A., and P. Guyot-Sionnest, 2008, *Science* **322**, 929.
- Vázquez de Parga, A. L., F. Calleja, B. Borca, M. C. G. Passeggi, J. J. Hinarejos, F. Guinea, and R. Miranda, 2008, *Phys. Rev. Lett.* **100**(5), 056807.
- Park, C., H. Yang, A. J. Mayn, G. Dujardin, S. Seo, Y. Kuk, J. Ihm, and G. Kim, 2011, arXiv:1102.1269 .
- Park, S., and R. S. Ruoff, 2009, *Nature Nanotechnology* **4**, 217.
- Passoni, M., F. Donati, A. Li Bassi, C. S. Casari, and C. E. Bottani, 2009, *Phys. Rev. B* **79**(4), 045404.
- Pauling, L., 1931, *J. Am. Chem. Soc.* **53**(4), 1367.
- Pekar, S. I., 1946, *Soviet Physics, JETP* **16**, 335.

- Petta, J. R., A. C. Johnson, J. M. Taylor, E. A. Laird, A. Yacoby, M. D. Lukin, C. M. Marcus, M. P. Hanson, and A. C. Gossard, 2005, *Science* **309**, 2180.
- Pietryga, J. M., D. J. Werder, D. J. Williams, J. L. Casson, R. D. Schaller, and V. I. Klimov, 2008, *J. Am. Chem. Soc.* **130**, 4879.
- Pletikosic, I., M. Kralj, D. okevi, R. Brako, P. Lazi, and P. Pervan, 2010, *J. Phys.: Condens. Matter* **22**, 135006.
- Ponomarenko, L. A., F. Schedin, M. I. Katsnelson, R. Yang, E. W. Hill, K. S. Novoselov, and A. K. Geim, 2008, *Science* **320**, 356.
- Pou, P., S. A. Ghasemi, P. Jelinek, T. Lenosky, S. Goedecker, and R. Perez, 2009, *Nanotechnology* **20(26)**, 264015.
- Preobrajenski, A. B., M. L. Ng, A. S. Vinogradov, and N. Mårtensson, 2008, *Phys. Rev. B* **78(7)**, 073401.
- Rabe, U., K. Janser, and W. Arnol, 1996, *Rev. Sci. Instrum.* **67(9)**, 3281.
- Rast, S., C. Wattinger, U. Gysin, and E. Meyer, 2000, *Rev. Sci. Instrum.* **71**, 2772.
- Reed, A. E., L. A. Curtiss, and F. Weinhold, 1988, *Chem. Rev.* **88(6)**, 899926.
- Reina, A., X. Jia, J. Ho, D. Nezich, H. Son, V. Bulovic, M. S. Dresselhaus, and J. Kong, 2009, *Nano Lett.* **9(1)**, 30.
- Ritter, K. A., and J. W. Lyding, 2009, *Nature Materials* **8**, 235.
- Robel, I., V. Subramanian, M. Kuno, and P. V. Kamat, 2006, *J. Am. Chem. Soc.* **128(7)**, 2385.
- Rugar, D., H. J. Mamin, P. Guethner, S. E. Lambert, J. E. Stern, McFadyen, and T. Yogi, 1990, *Jo Appl. Phys.* **68(3)**, 1169.
- Rusponi, S., M. Papagno, P. Moras, S. Vlaic, M. Etzkorn, P. M. Sheverdyeva, D. Pacilé, H. Brune, and C. Carbone, 2010, *Phys. Rev. Lett.* **105(24)**, 246803.
- Rutter, G. M., J. N. Crain, N. P. Guisinger, T. Li, P. N. First, and J. A. Stroscio, 2007, *Science* **317**, 219.
- Rycerz, A., J. Tworzydło, and C. W. J. Beenakker, 2007, *Nature Physics* **3**, 172 .
- Sader, J. E., and S. P. Jarvis, 2004, *Applied Physics Letters* **84(10)**, 1801.
- Sarma, S. D., S. Adam, E. H. Hwang, and E. Rossi, 2011, *Rev. Mod. Phys.* **83(2)**, 407.
- Schaller, R. D., M. Sykora, J. M. Pietryga, and V. I. Klimov, 2006, *Nano. Lett.* **6(3)**, 424429.

- Schönenberger, C., H. van Houten, and C. Beenakker, 1993a, *Physica B* **189**, 218.
- Schönenberger, C., H. van Houten, H. C. Donkersloot, A. M. T. van der Putten, and L. G. J. Fokkink, 1992, *Physica Scripta* **45**, 289.
- Schönenberger, C., H. V. Houten, J. Kerkhof, and H. Donkersloota, 1993b, *Applied Surface Science* **67**, 222.
- Schwarz, A., and R. Wiesendanger, 2008, *Nanotoday* **3**, 28.
- Silvestrov, P. G., and K. B. Efetov, 2007, *Phys. Rev. Lett.* **98**.
- Sohn, L. L., L. P. Kouwenhoven, and G. Schn (eds.), 1997, *Mesoscopic Electron Transport* (Springer).
- Sols, F., F. Guinea, and A. H. C. Neto, 2007, *Phys. Rev. Lett.* **99**(16), 166803.
- Son, Y.-W., M. L. Cohen, and S. G. Louie, 2006, *Phys. Rev. Lett.* **97**(21), 216803.
- Sprinkle, M., M. Ruan, Y. Hu, J. Hankinson, M. Rubio-Roy, B. Zhang, X. Wu, C. Berger, and W. A. de Heer, 2010, *Nature Nanotechnology* **5**, 727.
- Starodub, E., A. Bostwick, L. Moreschini, S. Nie, F. E. Gabaly, K. F. McCarty, and E. Rotenberg, 2011, *Phys. Rev. B* **83**(12), 125428.
- Steiner, D., D. Dorfs, U. Banin, F. Della Sala, L. Manna, and O. Millo, 2008, *Nano Lett.* **9**, 2954.
- Stroschio, J. A., and R. J. Celotta, 2004, *Science* **306**, 242.
- Stroschio, J. A., F. Tavazza, J. N. Crain, R. J. Celotta, and A. M. Chaka, 2006, *Science* **313**, 948.
- Sugimoto, Y., M. Abe, S. Hirayama, N. Oyabu, O. Custance, and S. Morita, 2005, *Nature* **4**, 156.
- Sugimoto, Y., P. Pou, M. Abe, P. Jelinek, R. Perez, S. Morita, and O. Custance, 2007, *Nature* **446**, 64.
- Sutter, P., M. S. Hybertsen, J. T. Sadowski, and E. Sutter, 2009a, *Nano Letters* **9** (7), 26542660.
- Sutter, P., J. T. Sadowski, and E. Sutter, 2009b, *Phys. Rev. B* **80**(24), 245411.
- Sutter, P. W., J.-I. Flege, and E. A. Sutter, 2008, *Nature Materials* **7**, 406.
- Talapin, D. V., J. S. Lee, M. V. Kovalenko, and E. V. Shevchenko, 2010, *Chem. Rev.* **110**, 389.
- Talapin, D. V., and C. B. Murray, 2005, *Science* **310**, 86.

- Tanaka, A., S. Onari, and T. Arai, 1992, Phys. Rev. B **45**(12), 6587.
- Ternes, M., C. P. Lutz, C. F. Hirjibehedin, F. J. Giessibl, and A. J. Heinrich, 2008, Science **319**, 1066.
- Tersoff, J., and D. R. Hamann, 1985, Phys. Rev. B **31**(2), 805.
- Tersoff, J., C. Teichert, and M. G. Lagally, 1996, Phys. Rev. Lett. **76**(10), 1675.
- Urban, J. J., D. V. Talapin, E. V. Shevchenko, C. R. Kagan, and C. B. Murra, 2007, Nature Materials **6**, 115.
- Vanin, M., J. J. Mortensen, A. K. Kelkkanen, J. M. Garcia-Lastra, K. S. Thygesen, and K. W. Jacobsen, 2010, Phys. Rev. B **81**(8), 081408.
- te Velde, G., F. M. Bickelhaupt, E. J. Baerends, C. F. Guerra, S. J. A. van Gisbergen, J. G. Snijders, and T. Ziegler, 2001, Computational Chemistry **22**(9), 931.
- Visser, J., 1972, Adv. Colloid Interface Sci. **3**, 331.
- Wallace, P. R., 1947, Phys. Rev. **71**.
- Wang, B., M. Caffio, C. Bromley, H. Frchtl, and R. Schaub, 2010, ACS Nano **5**, 5773.
- Wang, B., X. Ma, M. Caffio, R. Schaub, and W.-X. Li, 2011, Nano Letters **11**(2)(0), 424.
- Wegner, D., R. Yamachika, Y. Wang, V. W. Brar, B. M. Bartlett, J. R. Long, and M. F. Crommie, 2008, Nano Lett. **8**, 131.
- Wiesendanger, R., 1998, *Scanning probe microscopy and spectroscopy: methods and applications* (Cambridge University Press).
- Wingreen, N. S., K. W. Jacobsen, and J. W. Wilkins, 1989, Phys. Rev. B **40**(17), 11834.
- Wu, S. W., N. Ogawa, and W. Ho, 2006, Science **312**, 1362.
- Yang, J., Y. Ren, and A. min Tian, 2004, J. Phys. Chem. B **104**(20), 49514957.
- Yu, D., C. Wang, and P. Guyot-Sionnest, 2003, Science **300**, 1277.
- Yu, D., C. Wang, B. L. Wehrenberg, and P. Guyot-Sionnest, 2004, Phys. Rev. Lett. **92**(21), 216802.
- Zhang, Y., V. W. Brar, F. Wang, C. Girit, Y. Yayon, M. Panlasigui, A. Zettl, and M. F. Crommie, 2008, Nature Physics **4**, 627.
- Zhang, Y., T.-T. Tang, C. Girit, Z. Hao, M. C. Martin, A. Zettl, M. F. Crommie, Y. R. Shen, and F. Wang, 2009, Nature **459**, 820.



---

# Appendix: The band structure of graphene calculated with tight-binding method

The nearest neighbor tight-binding calculation for the  $\pi$  band structure of graphene is shown below. The variables have been labeled in Fig. .6.

We assume the  $\pi$  electron wavefunction of an isolated carbon atom is  $\phi(\vec{r})$  and the real electron wavefunction in graphene can be written as  $\psi(r) = \sum_{i=1}^4 c_i \phi_i(\vec{r}) e^{i\vec{k} \cdot \vec{R}_i}$ , where  $c_i$  is a constant. If we have a Hamiltonian operator  $\hat{H}$  for the electron in this band, then,

$$\hat{H} \sum_{i=1}^4 c_i \phi_i(\vec{r}) e^{i\vec{k} \cdot \vec{R}_i} = E(\vec{k}) \sum_{i=1}^4 c_i \phi_i(\vec{r}) e^{i\vec{k} \cdot \vec{R}_i} \quad (.3)$$

where  $E(\vec{k})$  is the energy dispersion function.

Multiplying Eq. (.3) by  $\phi_1^*(\vec{r})$  and integrate over the whole space on both sides of the equation result

$$\sum_{i=1}^4 c_i S_{1i} e^{i\vec{k} \cdot (\vec{R}_i - \vec{R}_1)} = E(\vec{k}) c_1 \quad (.4)$$

where  $S_{1i} = \langle \phi_1 | \hat{H} | \phi_i \rangle$ . By replacing  $\phi_1^*(\vec{r})$  with  $\phi_m^*(\vec{r})$  for  $m = 2, 3, 4$  results

$$\sum_{i=1}^4 c_i S_{mi} e^{i\vec{k} \cdot (\vec{R}_i - \vec{R}_m)} = E(\vec{k}) c_m. \quad (.5)$$

Equation (.4) can be explicitly written as

$$c_1 S_{11} + c_2 S_{12} e^{i\vec{k} \cdot \vec{R}_{21}} + c_3 S_{13} e^{i\vec{k} \cdot \vec{R}_{31}} + c_4 S_{14} e^{i\vec{k} \cdot \vec{R}_{41}} = E(\vec{k}) c_1. \quad (.6)$$

In Eq. (.5),  $m = 2, 3, 4$  is

$$c_1 S_{21} e^{i\vec{k} \cdot \vec{R}_{12}} + c_2 S_{22} = E(\vec{k}) c_2; \quad (.7)$$

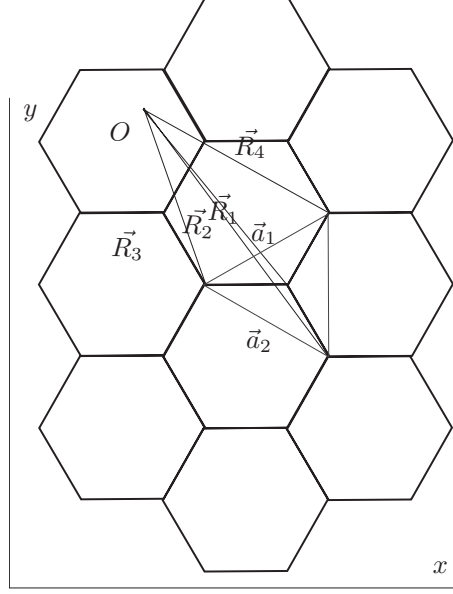


Figure .6: The graphene lattice and variables used in the nearest neighbor tight-binding calculation.

$$c_1 S_{31} e^{i\vec{k}\vec{R}_{13}} + c_3 S_{33} = E(\vec{k}) c_3; \quad (.8)$$

$$c_1 S_{41} e^{i\vec{k}\vec{R}_{14}} + c_4 S_{44} = E(\vec{k}) c_4, \quad (.9)$$

respectively. From the lattice symmetry it is easy to see that  $c_2 = c_3 = c_4$  and  $S_{12} = S_{13} = S_{14}$ ,  $S_{11} = S_{22}$ .

Adding Eqs. (.7), (.8), (.9) together, we have

$$c_1 S_{12} (e^{i\vec{k}\vec{R}_{12}} + e^{i\vec{k}\vec{R}_{13}} + e^{i\vec{k}\vec{R}_{14}}) = 3(E(\vec{k}) - S_{11}). \quad (.10)$$

Combining Eq. (.6) and Eq. (.10) results the expression of  $E(\vec{k})$ .

$$E(\vec{k}) = S_{11} \pm S_{12} \frac{\sqrt{3 + 2 \cos(\vec{k}\vec{a}_1) + 2 \cos(\vec{k}\vec{a}_2) + 2 \cos(\vec{k}(\vec{a}_1 - \vec{a}_2))}}{\sqrt{3}}, \quad (.11)$$

where the value of  $S_{11}$  can be set to zero. With proper coordinates, Eq. .11 can be written as

$$E(\vec{k}) = \pm S_{12} \frac{\sqrt{3 + 2 \cos(k_x \sqrt{3}a/2 + k_y a/2) + 2 \cos(k_x \sqrt{3}a/2 - k_y a/2) + 2 \cos k_y a}}{\sqrt{3}}, \quad (.12)$$

where  $S_{12} = \gamma_0$  is the nearest neighbor hopping energy. One band diagram drawn from this equation is shown in Fig. 5.2.

---

# Summary

This thesis deals with low temperature scanning tunneling microscopy/spectroscopy and atomic force microscopy (LT-STM/STS and AFM) studies on colloidal semiconductor and graphene quantum dots (g-QDs). These nanostructures are interesting because they show tunable electrical and optical properties due to the quantum confinement effect. The high spatial resolution of scanning probe microscopy makes it possible to measure the topography and the electronic properties of individual QDs. In addition to the experiments on the different types of QDs, this thesis also includes our experiments on the moiré pattern of an epitaxial graphene monolayer on Ir(111) and the measurement of the intermolecular interaction between two carbon monoxide molecules probed with the frequency modulation AFM (FM-AFM). These latter experiments shed light on the conceptual understanding of AFM measurements of atomically thin films and the use of molecule-modified AFM tip.

In the first chapter, we give a general introduction to the working principles of STM/STS and FM-AFM. In addition, we introduce the basic concepts of double-barrier tunneling junction, electron-phonon coupling in semiconductor nanocrystals and the use of a tuning fork force sensor in AFM, which provide some background knowledge for the understanding of the experiments presented in the following chapters.

In chapter 2, we discuss electron-phonon coupling in CdSe quantum dots (spheres and rods) probed by LT-STM. We resolve the polaronic states of the QDs, which are induced by the coupling between the tunneling electrons and longitudinal optical phonons. Our data show how the electron-phonon coupling strength depends on the orbital envelope function in these QDs and how the conductance spectrum evolves from shell-tunneling into the shell-filling regime once the tip is placed closer to the sample. Numerical calculations based on a dielectric continuum model can reproduce the experimentally measured electron-phonon coupling strength. We find that a relative broad distribution of coupling strengths in our sample, which reflects the differences in the dielectric environments of the QDs.

In chapter 3, we discuss the quantum transport properties of PbSe-CdSe core-shell QDs measured by LT-STM. We observed a series of equally spaced double resonances in the conductance spectra of these QDs. The phenomenon is explained by hole-induced electron transport, the hole occupation in the PbSe core enabled by the strong and relatively symmetric potential barrier of the CdSe shell. The presence

of a hole inside a QD shifts the energy of the electron tunneling channels by the electron-hole interaction energy,  $E_{e-h}$ . This induces the double peak feature in the conductance spectra when the average hole occupation is close to 0.5. From the conductance spectra, the electron-hole interaction energy can be directly measured and we find this is close to 80 *meV* for the QDs we investigated.

In chapter 4, the moiré pattern of an epitaxial graphene monolayer on the Ir(111) surface investigated with tuning fork based FM-AFM is presented and discussed. We applied FM-AFM to measure the geometric corrugation of the moiré pattern more directly. Aided by a simple theoretical estimate of the vdW interaction between the tip and the Ir substrate, we found a peak to peak corrugation of  $35 \pm 10$  *pm* for the epitaxial graphene monolayer on Ir(111). We also found that different regions of the graphene moiré unit cell have slightly different LDOS.

In chapter 5, we present our investigation on the confined electronic states in g-QDs with atomically well defined structure on Ir(111). These g-QDs have a diameter from a few to ca. twenty nanometers and a roughly hexagonal shape. We map the spatially resolved tunneling conductance that allows us to visualize how the confined states evolve with the energy in real space. The low energy carriers still have a linear dispersion down to the smallest g-QDs we have measured (about 2nm in diameter). Tight binding and effective Hamiltonian approaches show good agreement with the experimental results. More generally, these measurements demonstrate that the intrinsic electronic structure of atomically well-defined g-QDs can be studied when they are deposited directly on a metallic surface, provided that the coupling with the substrate is sufficiently weak.

Chapter 6 is devoted to the FM-AFM experiments on probing the intermolecular interaction between two carbon monoxide molecules. With one CO molecule attached to the AFM tip apex, we measure how the intermolecular interaction depends on the distance between the molecule on the tip and another molecule adsorbed on the Cu(111) surface. We found that at a close distance (few Å), there is a repulsive interaction induced by the Pauli repulsion between the electrons in the outer orbitals in these molecules. Also we found that geometric relaxation of the molecules has to be considered in order to explain the short range force response. Our experiments demonstrate the limitations of AFM force measurement using CO functionalized tips.

---

# Samenvatting

In dit proefschrift wordt beschreven hoe zowel rastertunnel microscopie ('Scanning Tunneling Microscopy', STM) en bijbehorende spectroscopie (STS) als atoomkracht microscopie ('Atomic Force Microscopy', AFM) gebruikt kunnen worden om colloïdale halfgeleider en grafeen quantum deeltjes (g-QDs) te bestuderen. Deze nanostructuren zijn interessant vanwege hun vele mogelijke toepassingen: vanwege het 'quantum confinement effect' zijn elektrische en optische eigenschappen variabel. De hoge ruimtelijke resolutie van een 'scanning probe microscoop' maakt het mogelijk om de topografie en elektronische eigenschappen van individuele QDs te meten. Naast de experimenten op verschillende soorten QDs, beschrijft dit proefschrift ook nog twee andere experimenten: bij de eerste wordt het moiré patroon van epitaxiaal gegroeide grafeen monolagen op Ir(111) bestudeerd, bij de ander wordt beschreven hoe een niet-contact AFM (FM-AFM) gebruikt kan worden om de intermoleculaire kracht tussen twee koolstofmonoxide moleculen te meten. Deze experimenten geven een idee hoe AFM-metingen van atomair-dunne lagen en molecuul-gemodificeerde AFM-naalden geïnterpreteerd moeten worden.

In het eerste hoofdstuk geven we een algemene introductie op de werking van zowel STM, STS als FM-AFM. Daarnaast introduceren we de beginselen van een 'double-barrier tunneling junction', de koppeling van elektronen en fononen in halfgeleider QDs en het gebruik van een stemvork-sensor voor AFM. Dit zal de benodigde achtergrond informatie geven om de experimenten in de rest van dit proefschrift te kunnen begrijpen.

In hoofdstuk 2 bespreken we de koppeling van elektronen en fononen in CdSe QDs (bolletjes en staafjes), gemeten met een LT-STM. Wij laten zien hoe de polaron toestanden van de QDs geanalyseerd kunnen worden. Deze toestanden ontstaan door de koppeling van tunnelende elektronen en optische fononen. Onze resultaten laten zien hoe de kracht van de elektron-fonon koppeling afhankelijk is van de orbitaal vorm in deze QDs, en hoe het geleidingsspectrum geleidelijk verandert van een schil-tunnelend tot een schil-vullend regime, wanneer de naald dichterbij het monster gebracht wordt. Berekeningen kunnen deze gemeten elektron-fonon koppelingskracht reproduceren aan de hand van een diëlektrisch continuüm model. Wij hebben een relatief brede verdeling van koppelingsterktes in ons monster gevonden; dit wijst op verschillen in de diëlektrische omgevingen van de verschillende QDs.

In hoofdstuk 3 bespreken we de quantum-transport eigenschappen van PbSe-CdSe

gelaagde QDs, zoals gemeten met LT-STM. We hebben series van dubbele resonanties gemeten in de geleidingsspectra van deze QDs, waarbij het energie verschil steeds gelijk was. De uitleg van dit fenomeen is gebaseerd op elektronengat-geïnduceerde elektron transport. De bezetting van het elektronengat in de PbSe kern wordt toegestaan door de sterke en relatief symmetrische potentiaal barrière van de CdSe schil. De aanwezigheid van het positief gat in de QD verschuift de energie van de elektronentunnelkanalen met de elektron-elektronengat interactieënergie:  $E_{e-h}$ . Dit effect induceert de kenmerkende dubbele pieken in de geleidingsspectra, gezien de gemiddelde elektronengatbezetting dicht bij 0.5 ligt. Uit de geleidingsspectra kan de interactieënergie van het elektron-elektronengat direct gemeten worden. Voor de QDs die wij bestudeerd hebben, ligt deze energie op 80 meV.

Het onderzoek naar het moiré-patroon van een epitaxiaal gegroeide grafeen monolaag op een Ir(111) oppervlak met stemvork-FM-AFM, wordt in hoofdstuk 4 gepresenteerd en bediscussieerd. Wij hebben FM-AFM toegepast om de geometrische rimpeling van het moiré patroon direct te kunnen bestuderen. Aan de hand van een eenvoudige theoretische schatting van de van-der-Waals interactie tussen de naald en het Ir substraat, hebben we een golf gemeten die van top tot top  $35 \pm 10$  *picometer* lang was. Ook hebben we ontdekt dat verschillende gebieden in de moiré-eenheidscel van grafeen kleine verschillen hebben in de LDOS.

In hoofdstuk 5 beschrijven we ons onderzoek naar begrensde elektronische toestanden in g-QDs met een goed beschreven atomaire structuur, op een oppervlak van Ir(111). Deze g-QDs hebben een diameter van enkele to ongeveer 20 nanometer en hebben een ruwweg zeshoekige vorm. Wij hebben de plaats-afhankelijke tunnelgeleiding in kaart gebracht, die ons in staat stelt om weer te geven hoe de begrensde toestanden veranderen met de energie. De laag-energetische dragers hebben een lineaire dispersie tot en met de kleinste g-QDs die wij gemeten hebben (met een diameter van  $\pm 2$  nm). Zowel benaderingen via een ‘tight binding’ model als via de effectieve Hamiltoniaan beschreven de experimentele resultaten goed. In algemene zin laten deze metingen zien dat de intrinsieke elektronische structuur van die g-QDs bestudeerd kunnen worden zelfs wanneer deze direct op een metalen oppervlak geadsorbeerd zijn, mits de quantum-koppeling voldoende zwak is.

Hoofdstuk 6 is gewijd aan de FM-AFM experimenten waarbij de intermoleculaire interactie tussen twee koolstofmonoxide molekulen wordt gemeten. Met één CO molecuul geadsorbeerd op de punt van de AFM naald, meten we hoe de intermoleculaire interactie afhankelijk is van de afstand tussen het molecuul op de punt en een ander molecuul dat geadsorbeerd is op het Cu(111) oppervlak. We hebben ontdekt dat er op korte afstanden een tegenwerkende interactie wordt geïnduceerd door de Pauli repulsie tussen elektronen in de buitenste orbitalen van de moleculen. Ook hebben we ontdekt dat verandering van de bindingsboek van de moleculen in acht genomen moet worden bij het uitleggen van dit korte-afstandseffect. Onze experimenten laten zien wat de beperkingen zijn van kracht-microscopie wanneer gebruik gemaakt wordt van een CO-gefunctionaliseerde naald.

---

# Dankwoord

I would like to thank Prof. Daniël Vanmaekelbergh and Prof. Peter Liljeroth for providing me the opportunity to work in the CMI group. Especially, I want to thank Peter, a distinguished teacher, for guiding me into the world of SPM. I cannot ask for more from him.

Thank all the group members I have been working with during my PhD period, prof. A. Meijerink, prof. J. Kelly, Dr. C. de. Mello-Donaga, prof. dr. H.W. de Wijn, Philip, Rolf, Karen, Linda, Alex, Mark, Ingmar, Dominika(多米尼卡), Zachar, Wiel, Esther, Yiming(一鸣), Joren, Marianna, Francesca, Dariusz, Rosa, Bert, Relinde, Rogier, Joost, Lucas, Karen, Matti, Freddy, Sander, Nico, Ward, Tim etc. It was a pleasure to work with you and I learned a lot from you during these days. I also would like to give special thanks to Karen, Mark, Ingmar, Rogier, Lucas, Joost, Sampsa and Christophe for their cooperation on the STM experiments. The experience continually reminds me that experimental physics is not a science of individual person. A special thanks goes to Hans and Stephan for solving the problems I had with our STM and PC. Furthermore, I would like to thank Stefan and Dominika for helping me cooling down the LT-STM during the many weekdays and weekends.

Thank Pieter for sharing his house with me during the last year.

Thank all these old and new friends I haven't mentioned yet: Hengyu(恒宇), Dapeng(大鹏), Fang(芳), Liang(良), Haitao(海涛), De(德), Ran(冉) and Juan(娟), Bo(博), Yanchao(彦超), Xin(鑫), Yinghuan(迎焕), Qiulan(秋蓝), Yuan(媛), Meikun(媚坤), Lu(璐), Xinghan(星汉), Qingyun(庆云), Wenhao(文豪), Jinbao(金宝), Ou(欧), Qing(清), Jingkun(敬坤), Dawei(大伟), Junting(俊婷), Haifan(海帆), Ao(傲), Jerry etc. Cannot image my life without meeting you guys!

Thank the encouragement and support I got during writing this thesis, from Daniël, Peter, Mana(曼娜), Jingkun, Qiulan etc. Thank Evelien(伊芙琳) for helping me to translate the summary of this thesis into Dutch. Bedankt!

Finally, I want to give my grateful thanks to my parents, for their endless support.



---

# List of publications

This thesis is based on following publications:

- Sampsa K. Hämäläinen, Zhixiang Sun, Mark P. Boneschanscher, Andreas Uppstu, Mari Ijäs, Ari Harju, Daniël Vanmaekelbergh, and Peter Liljeroth, Quantum confined electronic states in atomically well-defined graphene nanostructures, *Phys. Rev. Lett.* 107, 236803 (2011)
- Zhixiang Sun, Mark P. Boneschanscher, Ingmar Swart, Daniël Vanmaekelbergh, and Peter Liljeroth, Quantitative Atomic Force Microscopy with Carbon Monoxide Terminated Tips, *Phys. Rev. Lett.* 106, 046104 (2011)
- Zhixiang Sun, Sampsa K. Hämäläinen, Jani Sainio, Jouko Lahtinen, Daniël Vanmaekelbergh, and Peter Liljeroth, Topographic and electronic contrast of the graphene moiré on Ir(111) probed by scanning tunnelling microscopy and noncontact atomic force microscopy, *Phys. Rev. B* 83, 081415(R) (2011)
- Ingmar Swart, Zhixiang Sun, Daniël Vanmaekelbergh and Peter Liljeroth, Hole-Induced Electron Transport through Core-Shell Quantum Dots: A Direct Measurement of the Electron-Hole Interaction, *Nano Lett.*, 10, 1931 (2010)
- Zhixiang Sun, Ingmar Swart, Christophe Delerue, Daniël Vanmaekelbergh, and Peter Liljeroth, Orbital and Charge-Resolved Polaron States in CdSe Dots and Rods Probed by Scanning Tunneling Spectroscopy, *Phys. Rev. Lett.* 102, 196401 (2009)